Contribution of somatostatin interneurons to correlated neuronal activity in the developing hippocampus

Dissertation

zur Erlangung des akademischen Grades

doctor rerum naturalium (Dr. rer. nat.)

vorgelegt dem Rat der Medizinischen Fakultät

der Friedrich-Schiller-Universität Jena

von

M.Sc. Tom Floßmann

geboren am 30. Mai 1990 in Jena, Deutschland

Gutachter

1. Prof. Knut Holthoff, Universitätsklinikum Jena

2. Prof. Stefan H. Heinemann, Friedrich-Schiller-Universität Jena

3. Prof. Thomas G. Oertner, Universitätsklinikum Eppendorf Hamburg

Tag der öffentlichen Verteidigung: 03. Dezember 2019

Table of contents

1. List of abbreviations

alv.	*alveus*
AMPA	α-amino-3-hydroxy-5-methyl-4-isoxazolepropionic acid
AMPA-R	α-amino-3-hydroxy-5-methyl-4-isoxazolepropionic acid receptor
BiC	bistratified cells
BPN	backpropagating neuron
CA1	*cornu ammonis* 1
CA3	*cornu ammonis* 3
Ca_V	voltage-gated Ca^{2+} channel
ChR2	channelrhodopsin 2-EYFP fusion protein
EEG	electro-encephalogram
E_{Cl}-	chloride reversal potential
Emx1	empty spiracles homeobox 1 promoter
EYFP	enhanced yellow fluorescent protein
GABA	γ-amino-butyric-acid
$GABA_A$-R	ionotropic GABA receptor
GDP	giant depolarizing potential
GPCR	G-protein coupled receptor
GPSC	GABAergic postsynaptic current
HR3	eNpHR3.0-EYFP fusion protein
HSN	hippocampo-septal neuron
KCC2	K^+ $2Cl^-$ cotransporter
NKCC1	Na^+ K^+ $2Cl^-$ cotransporter
NMDA	N-Methyl-D-aspartate
NMDA-R	N-Methyl-D-aspartate receptor
O-BiC	*oriens* bistratified cells
OGB1 AM	Oregon Green BAPTA-1 acetoxymethyl ester
OLM	*oriens-lacunosum moleculare*
PC	pyramidal cell
PSC	postsynaptic current
s.l.m.	*stratum lacunosum moleculare*
s.o.	*stratum oriens*
SOM	somatostatin

SOM^{ChR2}	ChR2 expression under control of SOM promoter
SOM^{HR3}	HR3 expression under control of SOM promoter
SPW	sharp wave

2. Zusammenfassung

Frühe korrelierte neuronale Aktivität tritt in Form synchroner *Bursts* von Aktionspotentialen in großen Zellpopulationen und in allen Teilen des sich entwickelnden Gehirns auf. Eine wachsende Zahl an Studien legt nahe, dass synchrone Aktivität einen wichtigen Beitrag zur Reifung des neuronalen Netzwerks leistet und dabei auftretende Störungen zur Fehlentwicklung des Nervensystems führen. Aus diesem Grund ist ein mechanistisches Verständnis der Generierung korrelierter neuronaler Aktivität von großer Bedeutung für die klinische Forschung. Im unreifen Hippokampus tritt synchrone Aktivität kurz nach der Geburt auf und ist hochgradig von der depolarisierenden Wirkung bei synaptischer $GABA_A$-Rezeptor-Aktivierung abhängig. Interneurone, die GABA freisetzen, sind mit hoher Wahrscheinlichkeit an der Burst-Generierung beteiligt. Welche der anatomisch hochgradig heterogenen Subtypen GABAerger Interneurone an der Generierung korrelierter Aktivität im unreifen Hirn beteiligt sind, ist bislang nur unvollständig aufgeklärt. In der vorliegenden Dissertation wird der Beitrag der Somatostatin-exprimierenden (SOM)-Interneurone an korrelierter neuronaler Aktivität im sich entwickelnden Hippokampus untersucht.

Um die zugrundeliegenden synaptischen Mechanismen zu analysieren, kamen elektrophysiologische und optische Techniken an akuten hippokampalen Hirnschnitten von neonatalen Mäusen zum Einsatz. In einem transgenen Tiermodell wurde die Beteiligung von entweder glutamatergen Pyramidenzellen oder GABAergen SOM-Interneuronen an synchroner Aktivität mithilfe zellspezifischer Expression des Kalziumfarbstoffs GCaMP6s und schneller konfokaler Kalziumbildgebung sowie paralleler Ableitung des lokalen Feldpotentials untersucht. Es wurde gezeigt, dass beide Populationen während neuronaler *Bursts* spontan und hochgradig korreliert aktiv sind. Mittels der Expression des optisch-aktivierbaren Natriumkanals Channelrhodopsin 2 (ChR2) in SOM-Interneuronen (SOM^{ChR2}) wurden Aktionsströme optogenetisch induziert. Elektrophysiologische Messungen zeigten, dass die Photoaktivierung von SOM-Interneuronen eine $GABA_A$-Rezeptor-abhängige synaptische Erregung von Pyramidenzellen zur Folge hat, die vom Chlorid-Importer NKCC1 abhängig ist. In Ableitungen von Pyramidenzellen mithilfe von Kalziumbildgebung wurde zudem gezeigt, dass die Photoaktivierung von SOM^{ChR2} korrelierte Netzwerkaktivität ähnlich der Spontanaktivität induziert. Komplementär

wurde unter Verwendung einer optogenetischen Strategie zur Hemmung von SOM-Interneuronen der Beitrag der spontanen Feuerrate dieser Nervenzellpopulation zur Burst-Generierung untersucht. Zu diesem Zweck wurden transgene Mäuse eingesetzt, welche die lichtgetriebene Chlorid-Pumpe eNpHR3.0 (HR3), ein molekulargenetisch optimiertes Halorhodopsin-Konstrukt, in SOM-Interneuronen (SOM^{HR3}) exprimieren. Die Photoinhibition von SOM^{HR3} wurde für langanhaltende Hyperpolarisation der Zellen optimiert und reduzierte effektiv die spontane Feuerrate der SOM-Interneurone. Elektrophysiologische Messungen von Pyramidenzellen ergaben, dass die Photoinhibition von SOM^{HR3} eine Reduktion der *Burst*-Aktivität im Pyramidenzellband der CA1 Region des neonatalen Hippokampus zur Folge hat.

Zusammenfassend zeigt die vorliegende Arbeit, dass SOM-Interneurone durch präsynaptisches spontanes Feuern von Aktionspotentialen und eine erregende postsynaptische $GABA_A$-Rezeptor Aktivierung in glutamatergen Pyramidenzellen die korrelierte Netzwerkaktivität im sich entwickelnden Hippokampus antreiben. Die hier gefundenen Ergebnisse leisten einen wichtigen Beitrag zum mechanistischen Verständnis spontaner korrelierter Aktivität und der aktivitätsabhängigen Hirnreifung.

3. Abstract

Spontaneous correlated neuronal activity fine-tunes the developing brain and disturbances thereof may cause severe neurodevelopmental disorders. Hence, understanding the underlying mechanisms of early neuronal activity instructing the neuronal circuitry is a key for research of diseases and clinical prevention. In the immature hippocampus correlated bursts of neuronal activity occur at early perinatal stages and are highly dependent on a depolarizing postsynaptic current upon γ-amino-butyric-acid (GABA) gated ionotropic receptor ($GABA_AR$) activation. The contribution of GABA-releasing interneuronal subpopulations to the mechanism of burst generation remains elusive. In the present work, the GABAergic subpopulation of somatostatin-expressing (SOM) interneurons and its role in spontaneous correlated neuronal activity is investigated in the developing hippocampus.

To dissect the underlying synaptic mechanisms, electrophysiological and optical techniques were applied in acute hippocampal brain slices from neonatal mice. In a transgenic approach the participation of either glutamatergic pyramidal cells or GABAergic SOM interneurons during bursts were elucidated by the expression of the genetic Ca^{2+} indicator GCaMP6s and fast confocal Ca^{2+} imaging with parallel local field potential recordings. It was shown that both populations are during burst activity in a highly correlated manner. A light-gated Na^+ channel, channelrhodopsin 2 (ChR2), was utilized in a SOM interneuron specific transgenic mouse model (SOM^{ChR2}) to evoke photo-activated action potential firing in this population. Electrophysiological measurements revealed a $GABA_AR$-dependent synaptic connectivity with glutamatergic pyramidal cells in the CA1 pyramidal cell layer and an excitatory depolarizing mode of action at the postsynapses dependent on Cl^- importer NKCC1. Furthermore, Ca^{2+} imaging from the pyramidal cell layer revealed that photo-activation of SOM^{ChR2} evokes correlated neuronal activity reminiscent of spontaneous bursts. To elucidate the contribution of spontaneous action potential firing in SOM interneurons to burst generation, the light-activated chloride pump halorhodopsin (eNpHR3) was expressed under control of the SOM promoter (SOM^{HR3}) in transgenic mice. Photo-stimulation of SOM^{HR3} was optimized for stable hyperpolarizing currents and effectively inhibited spontaneous action potential firing in SOM interneurons. Electrophysiological recordings from pyramidal cells revealed that photo-inhibition of SOM interneurons reduced burst activity in CA1 pyramidal

cells. The mechanism of burst population dynamics was interpreted by a recurrent neural network model. Modeling the experimental findings revealed that tonic or temporally patterned GABA release from SOM interneurons elevates the activity level of the network due to the excitatory action of GABA towards a threshold and thereby either increases the probability of burst generation or simply triggers burst activity.

In conclusion, the present work shows that SOM interneurons drive correlated activity in the developing hippocampus depending on spontaneous action potential firing of presynaptic SOM interneurons and depolarizing postsynaptic $GABA_AR$ activation in glutamatergic pyramidal cells. The results provided here causal understanding of correlated neuronal activity with important implications for activity-dependent brain maturation.

4. Introduction

4.1 Neuronal activity in the context of brain development

During development, sequences of gene programs in neuron progenitors and post-mitotic neurons sculpt the brain architecture by guiding proliferation, subtype differentiation, migration, dendrite and axon growth, as well as synaptic specificity (O'Leary and Sahara 2008, Philippidou and Dasen 2013, Bandler *et al.* 2017, Lim *et al.* 2018, Favuzzi *et al.* 2019). Those genetic programs constitute a blueprint of the neuronal network, but lack the capability to fine-tune neuronal circuits for mature functionality. A growing number of publications provide evidence that electrical activity fills in this gap and interacts with the genetic program to drive brain maturation (reviewed in Spitzer 2006). Electrical neuronal activity in the developing brain can be divided in two categories: 1) intrinsic spontaneously generated activity and 2) sensory-evoked activity. The necessity of sensory experience during a critical postnatal period for proper establishment of synaptic connectivity was first convincingly demonstrated in the visual cortex by the Nobel laureates Hubel and Wiesel in cats and monkeys (Hubel 1982, Wiesel 1982), and subsequently in rodents (reviewed in Hensch 2005). However, in the last two decades a new field of research developed, which considers neuronal activity patterns preceding the onset of sensory perception as potentially critical for brain development. Those patterns of spontaneous activity are intrinsically generated by immature neurons synchronizing neuronal assemblies. Electrical activity stimulates intracellular signaling cascades and drives maturation processes like neuronal migration and differentiation (Katz and Shatz 1996, Spitzer 2006).

The emergence of spontaneous neuronal activity is a general characteristic of the immature mammalian brain and appears with the expression of voltage-gated channels (Luhmann *et al.* 2016, Griguoli and Cherubini 2017). Distinct mechanisms and patterns of spontaneous activity were reported at different stages *in vitro* and *in vivo* in all brain areas examined until now, including neocortex (Schwartz *et al.* 1998, Khazipov *et al.* 2004) and hippocampus (Ben-Ari *et al.* 1989, Leinekugel *et al.* 2002). For review of developmental spontaneuos activity see Blankenship and Feller 2010. Intrinsic burst-firing activates neighboring cells prenatally due to different mechanisms: extra-synaptic ionotropic receptor activation (Marchionni *et al.* 2007, Blankenship *et al.* 2009), electrical synapses or chemical synapses (Feller *et al.*

1996, Dupont *et al.* 2006). With the onset of chemical synaptic transmission, spontaneous activity recruits large neuron populations and generates correlated neuronal activity. In rodents, synapse-driven correlated activity occurs during the first two postnatal weeks between postnatal day (P) 0 and 10 (Khazipov and Milh 2018). Spontaneous correlated activity is observed abundantly in the regions of the telencephalon *in vitro* (Ben-Ari *et al.* 1989, Garaschuk *et al.* 1998, Dupont *et al.* 2006, Crepel *et al.* 2007) as well as *in vivo* (Leinekugel *et al.* 2002, Khazipov *et al.* 2004, Ackman *et al.* 2012, Kummer *et al.* 2016). The spontaneous synchronous activity fades out within the second postnatal week, when sensory inputs from retina and cochlea arise (McLaughlin *et al.* 2003, Babola *et al.* 2018). At this stage, network activity patterns become sparse and more complex (Buhl and Buzsaki 2005, Egorov and Draguhn 2013, Luhmann *et al.* 2016).

In the visual system, spontaneous correlated network activity during brain development has been studied intensively. *In vivo* studies demonstrated synchronous bursts of spontaneous discharges in retinal ganglion cells of fetal mice at prenatal stages (Galli and Maffei 1988, Meister *et al.* 1991). In absence of visual perception correlated retinal activity is induced by spontaneous co-release of acetylcholine and γ-amino-butyric-acid (GABA) from reciprocal connected starburst amacrine cells (Feller *et al.* 1996, Zheng *et al.* 2004). The recurrent excitatory network of starburst amacrine cells generates bursts of action potentials in postsynaptic retinal ganglion cells. This activity spreads stochastically across the inner retina as so called retinal waves and synchronizes neighboring retinal ganglion cells (Meister *et al.* 1991). The correlative activity increases intracellular Ca^{2+} concentrations in the retinal ganglion cells due to the activation of voltage-gated Ca^{2+} channels (Ca_V) in the neuronal membrane (Ackman *et al.* 2012). The retinal waves sculpt retinotopic map formation most likely due to a Ca^{2+}-dependent mechanism (McLaughlin *et al.* 2003, Liu *et al.* 2014). Disrupting retinal waves genetically causes developmental deficits in retinocollicular projections: distant retinal ganglion cells innervate the same superior colliculus cell and thereby form larger receptive fields in the colliculus (Liu *et al.* 2014). Furthermore, it has been shown that pharmacological blocking of retinal activity chronically disrupts ocular dominance columns of receptive fields in the primary visual cortex. Retinal waves interact with spontaneous correlated activity in the lateral geniculate nucleus and the primary visual cortex (Ackman *et al.* 2012, Ackman and Crair 2014). The interaction of the immature activity patterns

mimics adult sensory-driven activity and instructs the maturation of the visual system with persistent implications for adult functions.

Recent studies showed that correlated neuronal activity also occurs in preterm born human infants by the end of the second trimester (Iyer *et al.* 2015, Arichi *et al.* 2017). Intriguingly, specific properties of bursts recorded by electro-encephalography (EEG) correlate with neurodevelopmental outcome at an age of two years. This predictive character of early neuronal activity supports the idea that spontaneous correlated neuronal activity also drives brain maturation in humans.

An increasing number of studies illuminates the different levels on which circuitry refinement is mediated by spontaneous activity patterns: 1) neurogenesis (Bonetti and Surace 2010), 2) differentiation of neurotransmitter identity (Spitzer 2017), 3) neuronal migration (Komuro and Rakic 1996, Heck *et al.* 2007), 4) axonal myelination (Demerens *et al.* 1996), 5) synapse formation (Kwon and Sabatini 2011, Soto *et al.* 2012, Oh *et al.* 2016), 6) synaptic maturation (Kasyanov *et al.* 2004), and 7) neuronal apoptosis (Blanquie *et al.* 2017, Wong *et al.* 2018, Denaxa *et al.* 2018). Together these processes are contributing to the correct formation of brain subfields, cortical layer differentiation, excitation-inhibition balance, and adult neuronal functionality and connectivity (Hannan *et al.* 2001, Kilb *et al.* 2011, Burbridge *et al.* 2014, Luhmann *et al.* 2016, Che *et al.* 2018).

If activity-dependent mechanisms underlie physiological brain development, disturbances are likely to cause neurodevelopmental diseases (Meredith 2015, Schmidt and Mirnics 2015, Washbourne 2015). Genetic population studies and experimental evidences suggest a complex background of genetic alterations for neurodevelopmental diseases, which cause, in combination with pre- and perinatal external factors, abnormal brain development (Connors *et al.* 2008). Some studies indicate that pre- and postnatal environmental risk factors might lead to the development of autism and autism spectrum disorders due to the disturbance of immature neuronal activity patterns (Ben-Ari 2015, Modabbernia *et al.* 2017). Recent experimental studies on different models of epilepsy demonstrate that the interaction of deficient genotypes with electrical neuronal activity and external factors tremendously influences the outcome of genetic predispositions (Marguet *et al.* 2015, Salgueiro-Pereira *et al.* 2019). For instance, Marguet *et al.* utilized a genetic mouse model carrying a current-deficient mutation of the voltage-gated K^+ channel K_V7 with

clinical significance in human epilepsy. Neonatal K_V7-deficient mice show pronounced alterations in cortical network activity and hippocampal neuronal firing. They develop an adult hyperactive phenotype with pronounced behavioral consequences. Suppressing neuronal activity during a vulnerable period in the first two postnatal weeks rescued the wild type phenotype. Hence, a better understanding of the dynamics of early correlated neuronal activity is of great interest to resolve mechanisms underlying the physiology and pathophysiology of neurodevelopment.

4.2 Early correlated network activity in the developing hippocampus

The hippocampal formation is one of the best investigated regions in terms of neuronal activity and functions in the mature (Bannerman *et al.* 2014, Knierim 2015) and immature brain (Griguoli and Cherubini 2017). Here, neuronal network activity undergoes developmental changes from single-cellular spiking to small synchronous assemblies and large population activity (Figure 1). Spontaneous L-type channel-mediated Ca^{2+} spikes occur already at embryonic day 16-19 in the CA1 pyramidal cell layer (Crepel *et al.* 2007). Studies in the spinal cord of embryonic *Xenopus* demonstrated that early Ca^{2+} signaling affects neuronal proliferation, migration and differentiation (Spitzer 1994, Gu *et al.* 1994). In the murine hippocampus *in vitro,* some adjacent neurons are electrically coupled and form small units, which are called synchronous plateau assemblies (SPA), with intrinsic firing properties generating several seconds-lasting plateaus of increased intracellular Ca^{2+} concentration (Crepel *et al.* 2007) (Figure 1).

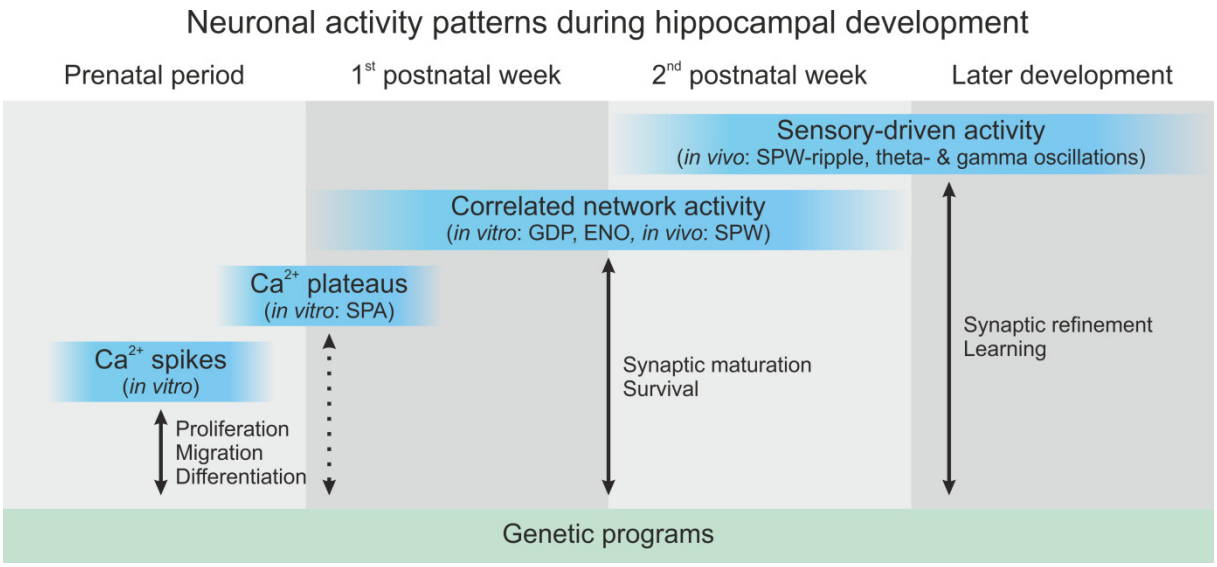

Figure 1. Developmental transition of neuronal activity patterns in the murine hippocampus.
The panel shows periods of several neuronal activity patterns during development (blue) and potential interactions with the genetic programs (arrows). SPA – synchronous plateau assembly, GDP – giant depolarizing potential, ENO – early network oscillation, SPW – sharp wave

After birth, so called sharp waves (SPWs) are the most prominent spontaneous activity patterns in the developing hippocampus *in vivo* (Figure 1). SPWs are recorded in local field potential measurements as solitary fast deflections indicating activity in a large number of neurons accompanied by unit activity and occurring in a frequency range of several events per minute (Sipilä *et al.* 2006, Leinekugel *et al.* 2002). They show similarities to SPW-ripples observed in the adult hippocampus, which are associated with spatial memory consolidation (Roux *et al.* 2017). However, until the end of the second postnatal week, immature SPWs miss the typical 140 Hz to 200 Hz ripple oscillation of mature SPWs (Buhl and Buzsaki 2005). *In vitro* preparations of the hippocampus also show the ability to reliably generate spontaneous rhythmic activity and thereby synchronize large neuronal populations. The activity pattern is characterized as long quiescent periods which are interrupted by prominent bursts of action potential firing simultaneously in large numbers of neurons (Ben-Ari *et al.* 1989). The several hundred milliseconds lasting depolarizations of the neuronal membrane potential accompanying the bursts are called giant depolarizing potentials (GDPs, Figure 1). They depend on glutamate and GABA-mediated synaptic transmission. It is still under debate whether SPWs are the *in vivo* counterpart to GDPs (Sipilä *et al.* 2006, Buzsaki 2015). The transition from SPW to SPW-ripple activity coincides with the generation of other rhythms like theta

and gamma oscillations *in vivo* and with the loss of the hippocampal capacity to generate GDPs in *in vitro* preparations (Egorov and Draguhn 2013).

With the ubiquitous expression of Ca_V the depolarizations trigger L-type Ca_V to open and cause transient increases of free intracellular [Ca^{2+}], so called Ca^{2+} transients. Due to the burst-firing of action potentials and corresponding depolarization, GDPs are strong drivers of Ca^{2+} transients and directly cause influx of Ca^{2+} in the participating cells (Garaschuk *et al.* 1998). Large scale recordings show that GDPs are propagating as Ca^{2+} waves or early network oscillations from CA3 into CA1 and adjacent areas of the entorhinal cortex and surprisingly *vice versa* in a retrograde direction (Shi *et al.* 2014, Barger *et al.* 2015). Ca^{2+} signaling is believed to be the principal link between neuronal activity and neuron maturation (West and Greenberg 2011). As a second messenger, intracellular Ca^{2+} controls proliferation, migration, differentiation and synaptic maturation of neurons (Yap and Greenberg 2018). This predestines GDPs as drivers of Ca^{2+} signaling-mediated changes in genetic expression patterns and intracellular protein rearrangement. This idea is discussed in an *in vitro* study, indicating that GDPs might act as coincidence detectors and thereby provide a mechanism to potentiate synaptic strength at mossy fiber projection synapses on CA3 pyramidal cells (PCs, Kasyanov *et al.* 2004). Recent studies in the developing cortex demonstrated that spontaneous neuronal activity is also positively regulating interneuron survival in a Ca^{2+} dependent manner (Denaxa *et al.* 2018, Priya *et al.* 2018, Wong *et al.* 2018). Further evidence indicates that similar mechanisms might exist for PC survival with region-specific differences (Ikonomidou *et al.* 1999, Blanquie *et al.* 2017). Thereby spontaneous correlated activity potentially provides a mechanism to balance the composition of GABAergic and glutamatergic neurons in the developing brain.

4.3 Developmental shift of $GABA_A$ receptor-mediated membrane polarization

GDP generation depends on recurrent synaptic excitation due to activation of postsynaptic N-methyl-D-aspartate receptors (NMDA-Rs) and α-amino-3-hydroxy-5-methyl-4-isoxazolepropionic acid receptors (AMPA-Rs), and, hence, on glutamate release from PCs (Ben-Ari *et al.* 1989, Bolea *et al.* 1999). Interestingly, it also relies on ionotropic GABA receptor ($GABA_AR$) activity. The contribution of $GABA_ARs$ to

GDP generation is mediated by a depolarizing current (Sipilä *et al.* 2005). The depolarizing action of GABA at resting membrane potential is a general feature of neonatal neurons which is observed not only in slice preparations, but also *in vivo* (Kirmse *et al.* 2015). There is a lively debate going on in the field, how depolarization upon $GABA_AR$ activation modulates neuronal activity (Bregestovski and Bernard 2012). A large number of studies on brain slice preparations from newborn mice demonstrated an excitatory action of GABA upon $GABA_AR$-mediated synaptic transmission. However, in the intact brain, $GABA_AR$ activation evokes smaller depolarizing potentials and causes shunting of excitatory postsynaptic currents (Kirmse *et al.* 2015). Taking into account that $GABA_ARs$ are permeable for Cl^- and HCO_3^-, the electrochemical driving force of both ions contribute to the $GABA_AR$ current (Kaila *et al.* 1989). Several *in vitro* studies illuminated that, beside the positive reversal potential of HCO_3^-, which is maintained stable over development and adulthood, the positively shifted reversal potential of Cl^- (E_{Cl}-) underlies depolarization upon $GABA_AR$ gating in immature neurons (Ben-Ari *et al.* 1990, Cherubini *et al.* 1991, Leinekugel *et al.* 1997, Ben-Ari *et al.* 2007). The elevated intracellular Cl^- concentration $[Cl^-]_{in}$ at immature stages is established by the Cl^- loading activity of the Na^+-dependent K^+ $2Cl^-$ cotransporter NKCC1 (Figure 2) (Yamada *et al.* 2004). Beyond the first postnatal week, $[Cl^-]_{in}$ decreases due to up-regulation of expression of the K^+-dependent $2Cl^-$ cotransporter KCC2 which is maintained high throughout adulthood (Rivera *et al.* 1999, Ben-Ari *et al.* 2012, Sato *et al.* 2017).

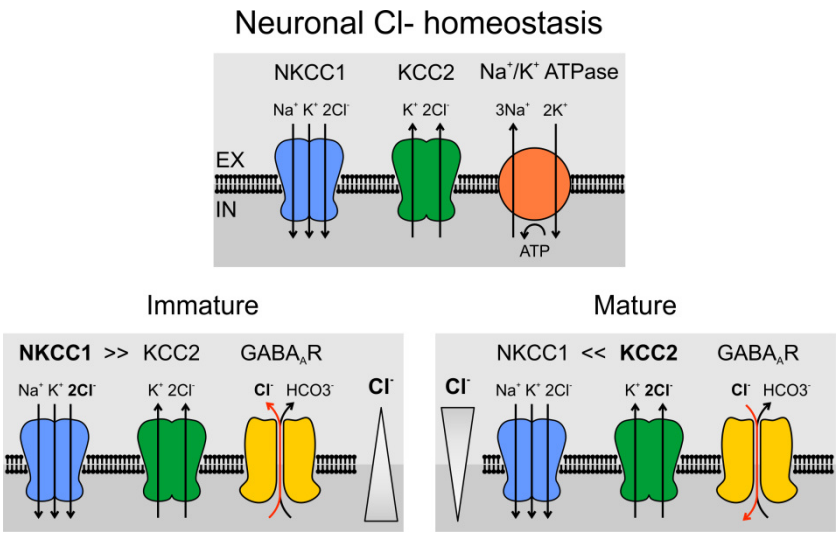

Figure 2. Developmental shift of membrane polarization upon GABAAR activation.
Top: NKCC1 and KCC2 maintain neuronal $[Cl^-]_{in}$ homeostasis driven by the electrochemical gradients of Na^+ and K^+ in a Na^+/K^+ ATPase-dependent manner. *Bottom*: During development, due to a decrease in the ratio of Cl^- transport between NKCC1 and KCC2, $GABA_AR$-mediated current shifts from depolarizing to hyperpolarizing at resting membrane potential. The triangles qualitatively indicate the electro-chemical gradient of Cl^- across the neuronal membrane. EX – extracellular space, IC – intracellular space

The developmental shift in E_{Cl}- renders $GABA_AR$ activation hyperpolarizing in mature neurons. Besides shunting, hyperpolarization is an important mechanism of the inhibitory function of GABAergic interneurons. Blocking NKCC1 in the immature hippocampus reduces the depolarizing action of GABA and attenuates the frequency of spontaneous correlated neuronal activity *in vitro* (Valeeva *et al.* 2013) and *in vivo* (Sipilä *et al.* 2006). Moreover, pharmacological inhibition of KCC2 activity increases the frequency and synchrony of GDPs in slices from neonatal rodents (Spoljaric *et al.* 2019). The establishment of GABAergic synapses precedes that of glutamatergic transmission during PC development in the hippocampal CA1 (Tyzio *et al.* 1999). During development, emerging glutamatergic synapses lack AMPA-Rs and are silent upon glutamate release at resting membrane potential due to the voltage-dependent Mg^{2+} block of NMDARs. Hence, sole glutamate release at silent synapses does not evoke NMDAR-mediated Ca^{2+} influx and excitatory postsynaptic potentials (EPSPs). Recurrent correlated neuronal activity triggers action potential firing in many cells simultaneously and thereby activates $GABA_ARs$ at GABAergic synapses close to silent glutamatergic synapses, which by chance receive glutamate at the same time. GABAergic sub-threshold depolarization facilitates NMDA-R currents due to a reduction of Mg^{2+} block (Leinekugel *et al.* 1997). The corresponding Ca^{2+} transients

are important for the recruitment of AMPA-Rs to the glutamatergic synapses in a process which is referred to as synapse unsilencing (Zhu *et al.* 2000). This process is also involved in the unsilencing of immature neurons in the optical tectum of Xenopus *in vivo* and depends on depolarizing GABAergic inputs (van Rheede *et al.* 2015). The control of GDP generation by depolarizing $GABA_AR$-mediated synaptic transmission suggests that interneurons have an important role in GDP generation and synaptic maturation.

4.4 Diversity of hippocampal SOM interneurons

Interneurons are divided into subclasses by their morphology, electrophysiological properties, embryonic origin or expression of molecular markers (Somogyi and Klausberger 2005, Tricoire *et al.* 2011). The latter is of outstanding interest, since it allows addressing distinct interneuron types via immuno-histochemistry or transgenic approaches, like the cre-lox P technique. Among the major molecularly defined GABAergic subpopulations are neurons expressing somatostatin (SOM), which are present in the perinatal hippocampus (Hennou *et al.* 2002). SOM is a genetically encoded peptide which is well described for its role as a hormone in the digestive system. As neurotransmitter, SOM modulates neuronal excitability and responses via pre- and postsynaptic action on G-protein coupled receptors (Liguz-Lecznar *et al.* 2016).

Most of the SOM interneurons show regular spiking. Some have slow firing and a small proportion has fast spiking properties (Mikulovic *et al.* 2015). This difference is likely related to the different functional demands of SOM expressing neuron subtypes. In the adult brain, CA1 SOM interneurons are involved in the control of high-frequency ripple oscillations (140-180 Hz), which are associated with hippocampus-dependent memory consolidation (Stark *et al.* 2014). Among other molecular subtypes, SOM interneurons are one of the first interneuron populations present in the postnatal hippocampus and originate from the medial (MGE) and in smaller number from the caudal (CGE) ganglionic eminence (Figure 3) (Pleasure *et al.* 2000). MGE interneurons contribute to GDP generation in the developing CA3 and CA1 (Wester and McBain 2016). Further it was shown, that hub interneurons, a functional und morphologically defined population of super-connected pioneering

MGE-derived interneurons, are partially SOM positive and contribute to the synchronization of the neonatal hippocampus (Picardo *et al.* 2011, Cossart 2014, Modol *et al.* 2017).

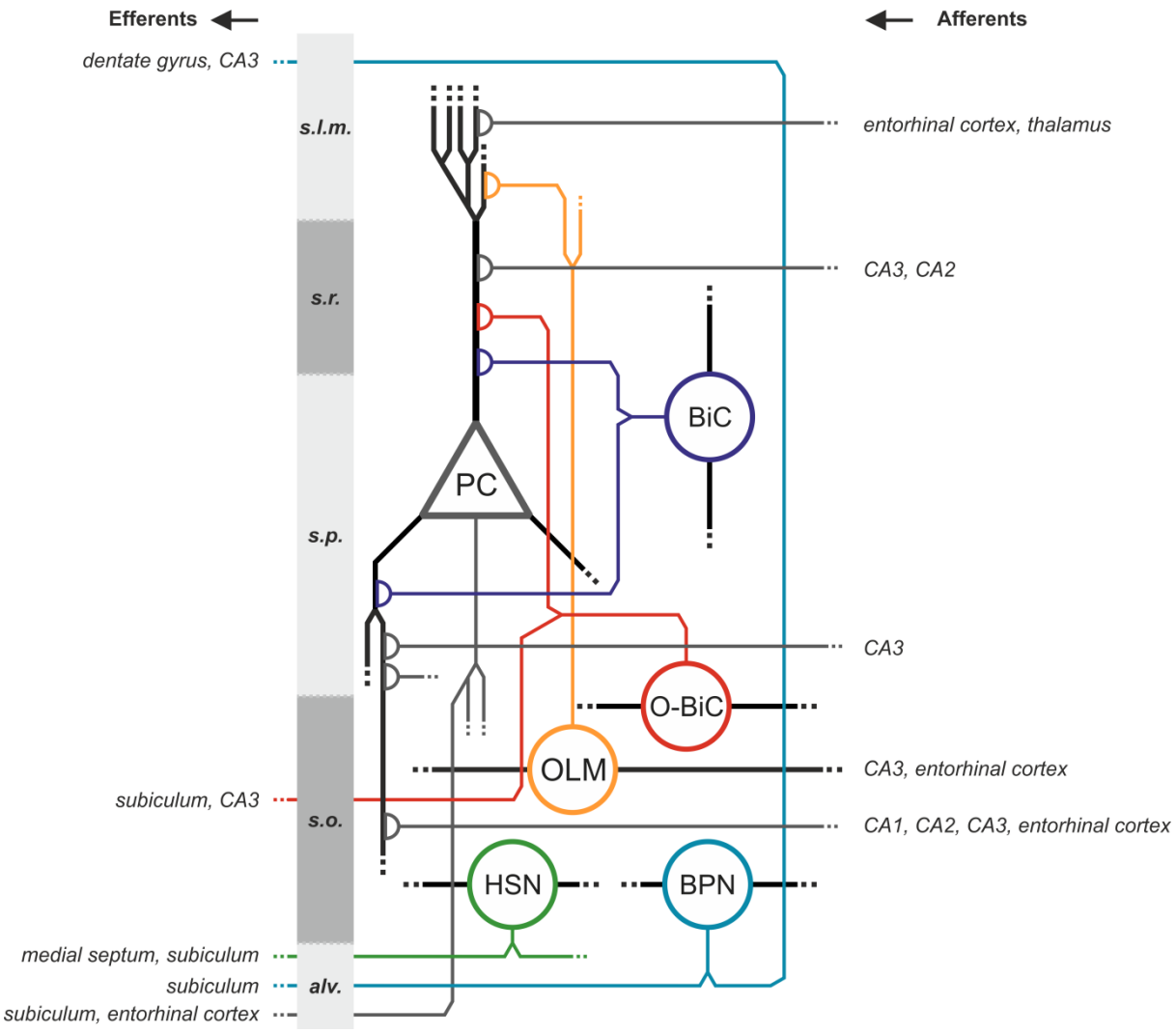

Figure 3. Overview of SOM interneuron circuitry in CA1 pyramidal cell layer of the adult hippocampus.

Axons and cell bodies are indicated in the color of the corresponding neuron, dendrites are indicated as black lines. Long-range projecting hippocampo-septal neurons (HSN) and back-propagating neurons (BPN) reside in *stratum oriens* (s.o.) and send axon projections along the *alveus* (alv.) fibers or *stratum lacunosum moleculare* (s.l.m.) into adjacent and distal brain regions. Local projecting *oriens-lacunosum moleculare* (OLM) neurons, bistratified cells (BiC) and *oriens*-bistratified cells (O-BiC) innervate different dendritic domains of CA1 PCs. For simplicity, no local projections from PCs to interneurons and synapses between interneurons are shown. s.p. *stratum pyramidale*, s.r. *stratum radiatum*

Among anatomical defined and well characterized SOM interneurons in the adult hippocampus are two different dendrite-targeting subtypes: I) bistratified cells (40% of CA1 SOM interneurons) (Baude *et al.* 2007) and II) *oriens lacunosum-moleculare* (OLM, 35% of CA1 SOM interneurons) neurons (Figure 3) (Leao *et al.* 2012). The somata of bistratified cells in the CA1 reside mainly within the *stratum pyramidale*, except *oriens*-bistratified cells (Figure 3), which are located in *stratum oriens* with horizontally running dendrites and heterogeneous innervation of local and distal PCs in subiculum and CA3 (Klausberger 2009). The dendrites of bistratified cells extend to *strata oriens* and *radiatum*. They co-express parvalbumin which correlates with fast-spiking properties. Almost all axonal projections of BiCs terminate on the basal and apical shafts of PCs and target dendrites aligned with PC projections from CA3. This circuitry is thought to support gamma-oscillations (30-80 Hz) in the adult brain via an inhibitory action of GABA (Tukker *et al.* 2007).

Soma and dendrites of OLM neurons are restricted to *stratum oriens* and the *alveus* (Pelkey *et al.* 2017). The axon of OLM neurons terminates in the *stratum lacunosum moleculare*. OLM interneurons receive excitatory inputs from entorhinal cortex, as well as from CA3 and CA1 PC collaterals, which provides a feedback inhibition in combination with their projections to apical dendritic tufts of the same cells (Leao *et al.* 2012). They fire at high frequencies and have low parvalbumin expression levels. Ventral hippocampal OLM-interneurons are driving type 2 theta-oscillations (4-9 Hz) which are associated with emotion-related behavior (Mikulovic *et al.* 2018). CA1 OLM-interneurons are further regulating object memory encoding and fear-related memory (Siwani *et al.* 2018). Recently, a single-cell transcriptomic study revealed at least 13 clusters of expression patterns in SOM interneurons with implications for different neuron subtypes (Harris *et al.* 2018). Among those clusters, the authors identified OLM neurons, BiCs, long-range projecting hippocampo-septal neurons (HSN) with projections to medial septum and subiculum, and nitric oxide synthase 1 positive back-projecting neurons (BPN) targeting subiculum, dentate gyrus and CA3 (Figure 3). However, the authors stated that the transitions between those subclasses are gradual and expression patterns as well as anatomical features within the groups are heterogeneous.

Due to the overlap of SOM interneurons with neuronal populations that are involved in the control of correlated activity in the adult and immature hippocampus, they are

promising candidates for a subtype-specific characterization of the mechanisms underlying spontaneous correlated neuronal activity.

5. Objectives of the study

The interactions of spontaneous neuronal activity and brain development are of great interest to understand neurodevelopmental diseases. The GABAergic system plays a special role in the control of early correlated network activity. However, it remains elusive how molecular defined subpopulations of interneurons causally contribute to synchronous activity.

Whether and how somatostatin expressing interneurons as a molecular defined subgroup of GABAergic interneurons contribute to early correlated neuronal activity in the developing hippocampus is still unknown. The present study dissects the mechanistic contribution of SOM interneurons to network activity in the neonatal hippocampus via optogenetic and pharmacological manipulations. The experimental observations were further tested in a computational recurrent neuronal network model (in collaboration with V. Rahmati and S. J. Kiebel) to investigate the mechanisms underlying population dynamics.

The present work addresses the issues:

(1) Do SOM interneurons participate in spontaneous correlated neuronal activity in the CA1 pyramidal cell layer of the developing hippocampus?

(2) Do SOM interneurons have output synapses on CA1 PCs and, if so, what is their mode of action?

(3) Does temporally patterned GABA release from SOM interneurons trigger correlated neuronal activity in the developing hippocampus?

(4) Are SOM interneurons causally involved in the generation of spontaneous correlated neuronal activity in the immature CA1?

(5) Which mechanism underlies the generation of spontaneous correlated neuronal activity in the neonatal network?

6. Published manuscript

6.1 Somatostatin interneurons promote neuronal synchrony in the neonatal hippocampus. Tom Flossmann, Thomas Kaas, Vahid Rahmati, Stefan J. Kiebel, Otto W. Witte, Knut Holthoff, Knut Kirmse, Cell Reports, Volume 26, Issue 12, 3173-3182.e5, 2019

Cell Reports

Report

Somatostatin Interneurons Promote Neuronal Synchrony in the Neonatal Hippocampus

Graphical Abstract

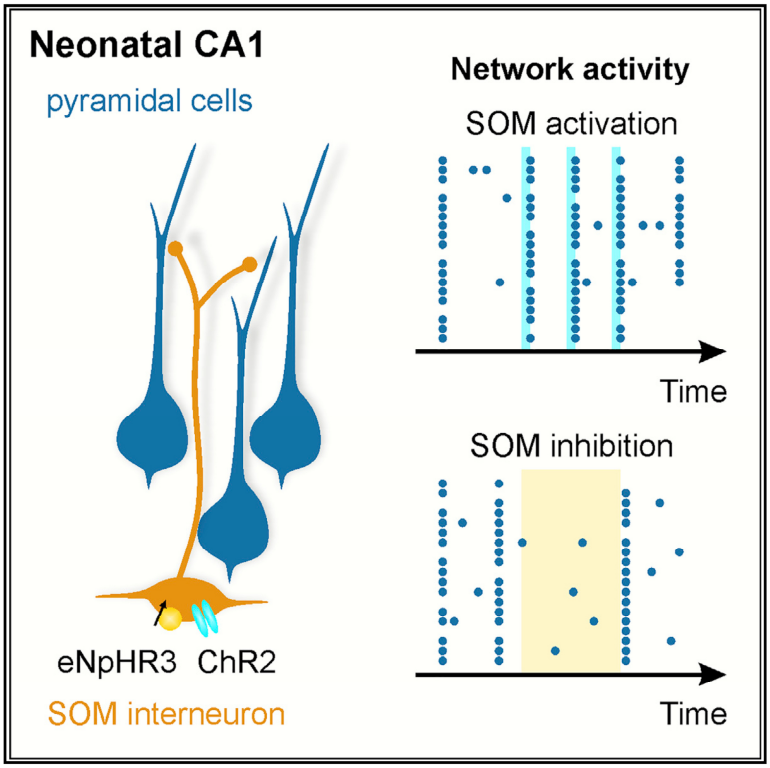

Authors

Tom Flossmann, Thomas Kaas, Vahid Rahmati, Stefan J. Kiebel, Otto W. Witte, Knut Holthoff, Knut Kirmse

Correspondence

knut.kirmse@med.uni-jena.de

In Brief

Developing neural circuits generate burst-like spontaneous activity. Flossmann et al. report a mechanism whereby somatostatin interneurons promote neuronal synchrony in the neonatal hippocampus. This action depends on depolarizing GABAergic output synapses and requires chloride uptake via NKCC1. Their findings have implications for the activity-dependent refinement of developing brain circuits.

Highlights

- Neonatal SOM interneurons establish excitatory GABAergic output synapses in CA1
- Spontaneous activity of SOM interneurons drives CA1 network synchrony
- The synchronizing capacity of SOM interneurons depends on NKCC1
- GABA-mediated excitation modulates network instability and amplification threshold

Flossmann et al., 2019, Cell Reports *26*, 3173–3182
March 19, 2019
https://doi.org/10.1016/j.celrep.2019.02.061

CellPress

Cell Reports
Report

Somatostatin Interneurons Promote Neuronal Synchrony in the Neonatal Hippocampus

Tom Flossmann,[1] Thomas Kaas,[1] Vahid Rahmati,[2] Stefan J. Kiebel,[2] Otto W. Witte,[1] Knut Holthoff,[1,3] and Knut Kirmse[1,3,4,*]
[1]Hans-Berger Department of Neurology, Jena University Hospital, 07747 Jena, Germany
[2]Department of Psychology, Technische Universität Dresden, 01187 Dresden, Germany
[3]These authors contributed equally
[4]Lead Contact
*Correspondence: knut.kirmse@med.uni-jena.de
https://doi.org/10.1016/j.celrep.2019.02.061

SUMMARY

Synchronized activity is a universal characteristic of immature neural circuits that is essential for their developmental refinement and strongly depends on GABAergic neurotransmission. A major subpopulation of GABA-releasing interneurons (INs) expresses somatostatin (SOM) and proved critical for rhythm generation in adulthood. Here, we report a mechanism whereby SOM INs promote neuronal synchrony in the neonatal CA1 region. Combining imaging and electrophysiological approaches, we demonstrate that SOM INs and pyramidal cells (PCs) coactivate during spontaneous activity. Bidirectional optogenetic manipulations reveal excitatory GABAergic outputs to PCs that evoke correlated network events in an NKCC1-dependent manner and contribute to spontaneous synchrony. Using a dynamic systems modeling approach, we show that SOM INs affect network dynamics through a modulation of network instability and amplification threshold. Our study identifies a network function of SOM INs with implications for the activity-dependent construction of developing brain circuits.

INTRODUCTION

Immature neuronal circuits generate correlated spontaneous activity, in which discrete events synchronize large cell populations. Synchronized activity has been found in multiple brain regions *in vitro* (Ben-Ari et al., 1989; Easton et al., 2014) and *in vivo* (Ackman et al., 2012; Khazipov et al., 2004; Kirmse et al., 2015; Kummer et al., 2016; Leinekugel et al., 2002; Yang et al., 2009), including in pre-term human infants (Iyer et al., 2015; Vanhatalo et al., 2005). Evidence suggests that specific spatiotemporal activity patterns are essential for proper circuit development (Zhang et al., 2011). The responsible mechanisms are diverse, comprising the regulation of cell survival (Blanquie et al., 2017), synaptogenesis (Oh et al., 2016), and synaptic plasticity of nascent connections (Winnubst et al., 2015). Disturbances of early activity can lead to persistent network alterations (Tolner et al., 2012) and promote the emergence of neurodevelopmental disorders (Kirmse et al., 2018).

A prototypical example of correlated activity are giant depolarizing potentials (GDPs) in the hippocampus *in vitro* (Ben-Ari et al., 1989). In rodents, GDPs are generated during the first postnatal week, when γ-aminobutyric acid (GABA), acting via $GABA_A$ receptors ($GABA_ARs$), mainly depolarizes postsynaptic cells (Kirmse et al., 2010; Tyzio et al., 2011). Antagonism or deletion of the chloride cotransporter NKCC1 (Sulis Sato et al., 2017; Yamada et al., 2004) interferes with GDP generation (Pfeffer et al., 2009; Sipilä et al., 2005), pointing to a pivotal role of GABAergic neurons in sculpting early activity. GABAergic interneurons (INs) exhibit an extraordinary diversity in anatomical, molecular, and physiological terms (Pelkey et al., 2017), but their roles in brain development are only beginning to be understood. Evidence suggests that soma-targeting INs originating from the medial ganglionic eminence (MGE) are critical to GDP generation (Picardo et al., 2011; Wester and McBain, 2016). In addition to prospective parvalbumin INs, the MGE gives rise to a second GABAergic population expressing the neuropeptide somatostatin (SOM). SOM INs represent a heterogeneous class, partially overlapping with early generated GABAergic hub cells (Villette et al., 2016), which were previously shown to orchestrate network synchrony (Picardo et al., 2011). SOM INs preferentially target dendrites (Pelkey et al., 2017) and are crucial for rhythm generation in the adult (Stark et al., 2014). In the neocortex, they become synaptically integrated by the neonatal period, forming a transient circuit with thalamocortical afferents and layer 4 (Anastasiades et al., 2016; Tuncdemir et al., 2016). SOM INs can be genetically targeted by $SOM^{IREScre}$ mice at early developmental stages (Taniguchi et al., 2011), but their role in network dynamics has not yet been directly examined.

Here, we address this question in the neonatal CA1 by combining Ca^{2+} imaging, electrophysiology, optogenetics, and computational modeling. We demonstrate an excitatory GABAergic connectivity between SOM INs and pyramidal cells (PCs) that drives the emergence of network synchrony during a critical period of brain maturation.

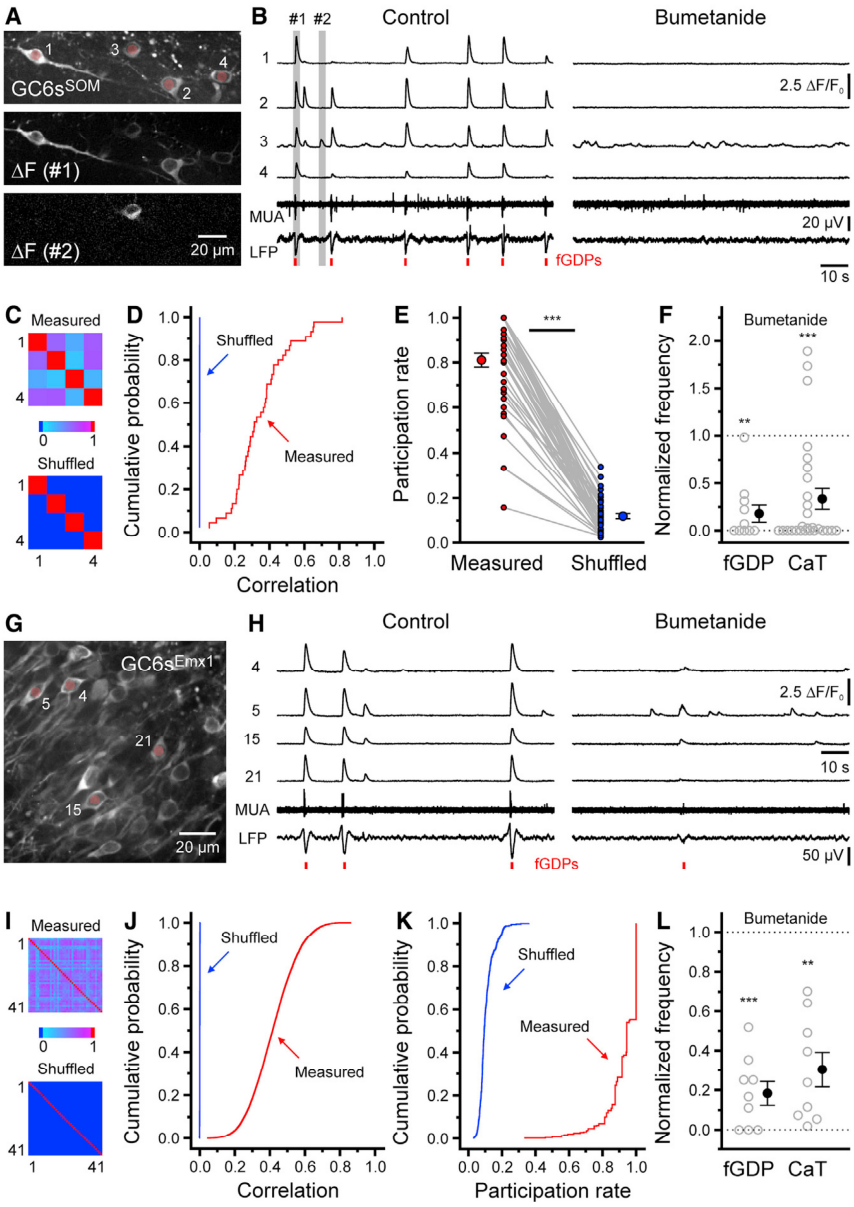

Figure 1. GABAergic SOM INs and Glutamatergic PCs Form a Network of Coactive Cells in the Neonatal CA1

(A) GCaMP6s-expressing SOM INs ($GC6s^{SOM}$) in *str. oriens* and ΔF images for time periods indicated in (B).

(B) Sample $\Delta F/F_0$ traces, time-aligned local field potential (LFP; 0.2–25 Hz), and multi-unit activity (MUA; > 200 Hz) in the absence and presence of bumetanide.

(C) Pearson correlation matrix for measured and randomly shuffled CaTs from the same slice.

(D) Pearson correlation coefficients (n = 45 cell pairs from 15 slices).

(E) Participation rates (n = 44 cells from 18 slices) for measured and randomly shuffled fGDPs.

(F) Effects of bumetanide.

(G) GCaMP6s-expressing PCs in *str. pyramidale*.

(H) Sample $\Delta F/F_0$ traces, time-aligned LFP, and MUA.

(I) Pearson correlation matrices from the same slice.

(J) Pearson correlation coefficients.

(K) Participation rates (n = 480 cells from 11 slices) for measured and randomly shuffled fGDPs.

(L) Effects of bumetanide. Each symbol represents a single slice.

In (B) and (H), for illustration, $F_0(t)$ was estimated by oversmoothing F(t). Data represent mean ± SEM. $^{**}p < 0.01$; $^{***}p < 0.001$. See also Table S1.

RESULTS

GABAergic SOM INs and Glutamatergic PCs Form a Network of Coactive Cells in the Neonatal CA1

As SOM INs are heterogeneous, we verified that cre expression in $SOM^{IREScre}$ mice is virtually excluded from bona fide glutamatergic Satb2-immunopositive neurons in area CA1 at postnatal day (P)5 (Figures S1A and S1B). To elucidate a potential involvement of SOM INs in spontaneous CA1 network activity, we conducted confocal Ca^{2+} imaging utilizing a cell-type-specific expression of GCaMP6s ($SOM^{IREScre}$:$GCaMP6s^{LSL}$ mice; Figure 1A). Somatic Ca^{2+} transients (CaTs) in SOM INs were invariably associated with action currents (ACs), even though GCaMP6s underestimated absolute spike numbers (Figure S1C). In Ca^{2+} imaging experiments, 48 out of 49 SOM INs recorded in *stratum* (*str.*) *oriens* were spontaneously active (CaT frequency: 2.6 ± 0.3 min^{-1}, n = 49 cells from 21 slices; Figure 1B), often in a synchronous manner (Figure 1B). Indeed, pairwise Pearson correlations for measured data were higher than those for randomly shuffled CaT event times (measured: 0.35 ± 0.02; shuffled: 0.00 ± 0.00, $p = 5.7 \times 10^{-14}$; n = 45 neuron pairs from 15 slices, exact Wilcoxon signed-rank test; Figures 1C and 1D; Table S1). CaTs were frequently paralleled by local field potential signals, referred to as field GDPs (fGDPs; frequency: 0.9 ± 0.2 min^{-1}; n = 21 slices), and multi-unit discharges (Figure 1B). In individual SOM INs, CaTs were detected in 81.1% ± 3.1% of fGDPs, which is significantly higher than expected by chance (12.0% ± 1.1%; $p = 1.1 \times 10^{-13}$; n = 44 cells from 18 slices, exact Wilcoxon signed-rank test; Figure 1E).

In slices obtained from $Emx1^{IREScre}$:$GCaMP6s^{LSL}$ mice, we confirmed that fGDPs reflect a massive coactivation of PCs. Pairwise correlations among Emx1 cells were similarly as high as for SOM INs (measured: 0.42 ± 0.00; shuffled: 0.00 ± 0.00; $p < 1.0 \times 10^{-16}$, n = 11,178 neuron pairs from 11 slices, Wilcoxon signed-rank test; Figures 1G–1J; Table S1). Also, for individual Emx1 cells, the probability of CaT occurrence during fGDPs amounted to 92.8% ± 0.4%, which significantly exceeded

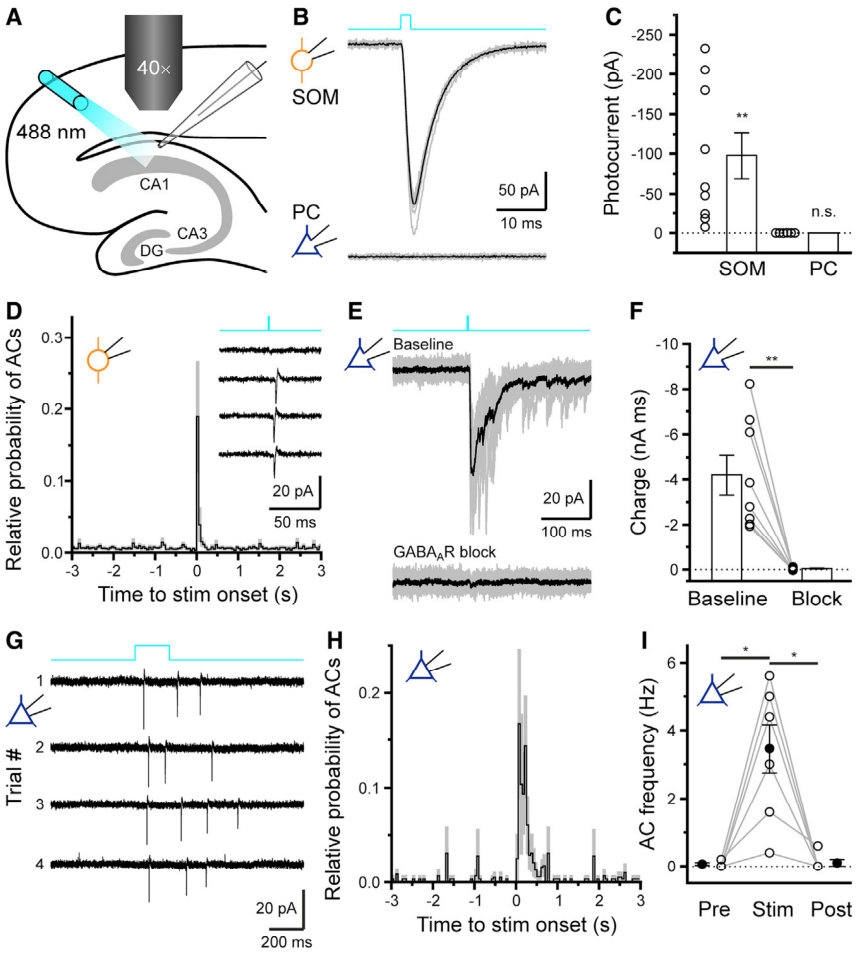

Figure 2. SOM INs Mediate an Excitatory GABAergic Input to Neonatal CA1 PCs

(A) Experimental arrangement. ChR2(H134R)-EYFP was conditionally expressed in SOM INs.

(B) In TTX, photo-stimulation (2 ms) induced inward currents in SOM INs but not PCs. Gray, individual traces; black, mean current.

(C) Quantification of photo-currents.

(D) Relative probability of action currents (ACs) around stimulation onset (n = 9 cells). Inset: sample traces from an individual cell.

(E) In DNQX and APV, photo-stimulation elicited PSCs in PCs that were sensitive to GABA$_A$R block.

(F) Charge transfer within 100 ms after stimulation onset in the absence or presence of a GABA$_A$R antagonist (bicuculline [20 μM, n = 3 cells] or gabazine [10 μM, n = 5 cells]).

(G) Photo-activation of SOM INs (200 ms, 100 Hz) evoked ACs in a PC (in DNQX and APV).

(H) Relative AC probability around stimulation onset (n = 6 PCs).

(I) AC frequency (500-ms time bins) at −0.5 s (Pre), 0 s (Stim), and 1 s (Post).

In (C), (F), and (I), each open symbol represents a single cell. Data represent mean ± SEM. *$p < 0.05$; **$p < 0.01$; n.s., not significant. See also Figure S2 and Table S2.

chance level (10.6% ± 0.2%; $p < 1.0 \times 10^{-16}$, n = 480 cells from 11 slices, Wilcoxon signed-rank test; Figures 1H and 1K). GDP generation depends on GABA$_A$R-mediated depolarization (Dzhala et al., 2005; Pfeffer et al., 2009; Sipilä et al., 2005), which results from chloride accumulation via electroneutral cotransporters, including NKCC1 (Kirmse et al., 2018). Therefore, we hypothesized that NKCC1 inhibition would impair CaT generation in both SOM INs and PCs. Indeed, the specific NKCC1 antagonist bumetanide (10 μM) inhibited fGDPs (Figures 1F and 1L) and reduced CaT frequencies to 33% ± 11% and 29.7% ± 8.6% of baseline in SOM INs and Emx1 PCs, respectively (SOM: $p = 4.8 \times 10^{-4}$, n = 27 cells from 11 slices; Emx1: $p = 3.9 \times 10^{-3}$, n = 9 slices; exact Wilcoxon signed-rank tests; Figures 1B, 1F, 1H, and 1L). Collectively, our data reveal that GABAergic SOM INs and glutamatergic PCs may constitute a common network of coactive cells in the developing CA1.

SOM INs Mediate an Excitatory GABAergic Input to Neonatal CA1 PCs

To address the role of SOM INs in GDP generation, we examined whether SOM INs are equipped with functional synaptic outputs. To this end, we transgenically expressed a channelrhodopsin-2(H134R)-EYFP fusion protein in SOM INs (ChR2^{SOM}). Whole-cell recordings in the presence of the voltage-gated Na^+ channel antagonist tetrodotoxin citrate (TTX) (0.5 μM) revealed that, at P1–P4, focally delivered pulses of blue light (2 ms; Figure 2A) induced inward currents in EYFP$^+$ SOM INs but not EYFP$^-$ PCs (SOM: −98 ± 29 pA, $p = 9.7 \times 10^{-3}$, n = 9 cells; PC: −0.1 ± 0.1 pA, p = 0.44, n = 6 cells, one-sample t tests; Figures 2B and 2C). Cell-attached and loose-patch recordings from SOM INs confirmed that photo-stimulation of ChR2^{SOM} evoked ACs in a pulse-number-dependent manner (Figures 2D and S2A–S2D; Table S2). To address whether neonatal SOM INs form GABAergic synapses, we performed whole-cell recordings from EYFP$^-$ PCs in the presence of ionotropic glutamate receptor antagonists (10 μM DNQX and 50 μM DL-2-amino-5-phosphonopentanoic acid [APV]). In all PCs examined, photo-activation of SOM INs induced postsynaptic currents (PSCs) with short latencies (7.1 ± 0.5 ms; charge transfer within 100 ms: −4.5 ± 1.3 nA ms; n = 12 cells). Based on their sensitivity to bicuculline (20 μM, n = 3) or gabazine (10 μM, n = 5), which reduced charge transfer to 1.1% ± 0.4% of baseline ($p = 1.7 \times 10^{-3}$ for pooled data, n = 8 cells, paired t test; Figures 2E and 2F), PSCs were mediated by GABA$_A$Rs. Conversely, repetitive (5 pulses, 100 Hz) photo-activation of SOM INs in the presence of bicuculline failed to evoke PSCs (charge transfer within 100 ms: 0.06 ± 0.07 nA ms, n = 4 cells), confirming that cre-dependent recombination is absent from glutamatergic PCs. These GABAergic inputs may excite PCs, as photo-stimulation (200 ms, 100 Hz) in the presence of DNQX plus APV reversibly increased AC frequency from 0.07 ± 0.04 Hz to 3.3 ± 0.8 Hz (Figures 2G–2I;

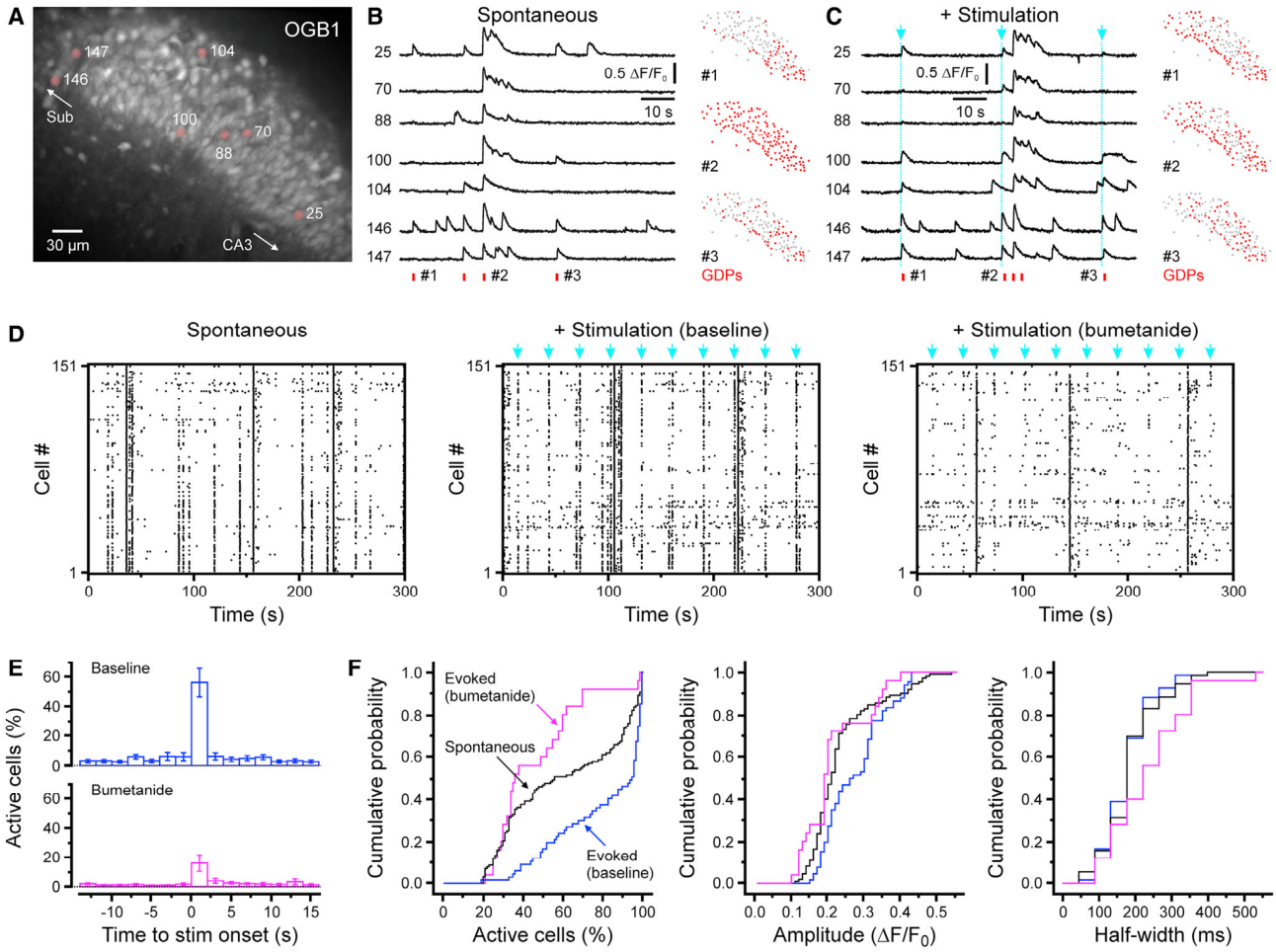

Figure 3. SOM INs Synchronize CA1 Network Activity in an NKCC1-Dependent Manner

(A) OGB1-stained CA1 cells. Arrows indicate slice orientation (Sub, subiculum).

(B) Sample $\Delta F/F_0$ traces. Right: activity maps of spontaneous GDPs (red, active cells; gray, inactive cells).

(C) Left: sample traces from the same set of cells. Blue, optogenetic stimulation (50 ms, 100 Hz). Right: activity maps of light-evoked GDPs.

(D) Raster plots indicating CaTs from all individual cells in *str. pyramidale* (i.e., primarily PCs) under baseline conditions (left) and in response to photo-stimulation (blue; 50 ms, 100 Hz) in the absence (middle) or presence (right) of bumetanide (same slice as in A–C).

(E) Fraction of active cells aligned to photo-stimulation onset (time = 0 s) in the absence or presence of bumetanide. Data represent mean ± SEM (n = 10 slices).

(F) Fraction of active cells (left), average amplitude of CaTs (middle), and half-width (right) of spontaneous (n = 128 GDPs) and evoked GDPs in the absence (n = 66 GDPs) or presence (n = 25 GDPs) of bumetanide (data from a total of 10 slices).

See also Figures S2 and S3 and Table S3.

Table S2). We conclude that SOM INs establish potentially excitatory GABAergic connections onto neonatal PCs.

SOM INs Can Synchronize CA1 Network Activity in an NKCC1-Dependent Manner

To clarify whether SOM INs can trigger synchronized activity, we performed Ca^{2+} imaging in slices from *SOM^{IREScre}; ChR2(H134R)^{LSL}* mice (Figure 3A). In the absence of ChR2^{SOM} stimulation, the activity of cells in *str. pyramidale* (i.e., primarily PCs) consisted of discrete network events (i.e., GDPs) interspersed between epochs of low synchronicity (a total of 10 slices and 1,284 cells were analyzed; Figure 3B). Neither the mean frequencies of CaTs and GDPs nor the active fraction of putative PCs during GDPs significantly differed from those in control slices lacking ChR2 (Figures S2E–S2G; Table S2). Strikingly, photo-activation of SOM INs was sufficient to induce GDP-like activity, as evidenced by the near-simultaneous generation of CaTs in large numbers of PCs (Figures 3C and 3D).

We quantified the effect of photo-stimulation by determining the active fraction of putative PCs for consecutive 2-s-long time bins. In standard artificial cerebrospinal fluid (ACSF), ChR2^{SOM} stimulation (50 ms, 100 Hz) increased the active cell fraction from 5.7% ± 2.7% before light stimulation to 56.2% ± 9.7% ($p = 1.0 \times 10^{-3}$, n = 10 slices, paired t test; Figure 3E; Table S3). This effect did not require intact projections from CA3, since photo-activation was similarly effective in slices, in

which CA3 had been mechanically disconnected from CA1 (from 1.5% ± 0.6% to 62.4% ± 9.0%; Figures S3A–S3C; Table S4). SOM INs may synchronize PCs by inhibition or excitation. If the latter mechanism is operative, attenuating GABAergic depolarization should inhibit their synchronizing capacity. Hence, we repeated the aforementioned experiment in naive slices following wash-in of bumetanide (10 μM). We found that photo-stimulation of $ChR2^{SOM}$ significantly increased the active fraction of putative PCs from 1.6% ± 0.8% to 16.0% ± 5.6% ($p = 0.037$, $n = 10$, paired t test; Figure 3E). A mixed-model ANOVA revealed a significant interaction for the independent variables (before or after stimulation × absence or presence of bumetanide: $p = 1.7 \times 10^{-3}$; Table S3), suggesting that SOM INs synchronize CA1 circuits in an NKCC1-dependent manner. The proposed role of GABAergic signaling in network excitation is compatible with the observation that, even in the presence of DNQX and APV, $ChR2^{SOM}$ stimulation increased, albeit to a lesser extent, the active fraction of putative PCs in a bumetanide-sensitive manner (Figures S3F–S3J; Table S4). Note that, in addition to inhibiting the evoked response, DNQX and APV also reduced baseline activity ($t(9.6) = 2.9$, $p = 0.016$; control: 0.17 ± 0.04 min^{-1}; DNQX + APV: 0.04 ± 0.01 min^{-1}; $n = 10$ and 6 slices, respectively, Welch's t test).

Using an operational definition of GDPs, we found that photo-stimulation of $ChR2^{SOM}$ evoked GDPs in 67% ± 11% of trials. Compared to spontaneous GDPs, evoked GDPs had similar kinetics, a higher fraction of active PCs, and higher single-cell CaT amplitudes (spontaneous: $n = 128$ GDPs; evoked: $n = 67$ GDPs; Figure 3F). Bumetanide reduced the fraction of stimulation trials resulting in GDP generation to 25% ± 10% ($t(9) = 3.6$, $p = 5.4 \times 10^{-3}$, $n = 10$ slices, paired t test). These data indicate that NKCC1- and $GABA_A$R-mediated excitation underlies the synchronizing effect of SOM INs. Optogenetically evoked GDPs in the presence of bumetanide did not significantly differ from spontaneous events (Figure 3F). In sum, optogenetic activation of SOM INs can induce synchronized, NKCC1-dependent network activity resembling spontaneous GDPs.

Spontaneous GABA Release from SOM INs Promotes GDP Activity in the Neonatal CA1

As optogenetic activation might enforce non-physiological spiking activity in SOM INs, we sought to corroborate our conclusions by optogenetic silencing. To this end, we expressed an eNpHR3.0-EYFP fusion protein in SOM INs ($HR3^{SOM}$). Whole-cell recordings verified that 30-s-long photo-stimulation of $HR3^{SOM}$ induced outward currents in all $EYFP^+$ SOM INs examined (16.3 ± 3.1 pA; $n = 6$ cells; Figure 4A). Photo-stimulation was performed in an alternating manner at 594/488 nm, which minimized current decay (Figure 4B). In voltage-clamp recordings, the membrane resistance of SOM INs (1.7 ± 0.2 GΩ; $n = 15$ cells) was almost twice as high as that of $EYFP^-$ PCs (0.9 ± 0.1 GΩ; $n = 40$ cells; $U = 109$, $p = 1.7 \times 10^{-4}$, exact Mann-Whitney U test), while their membrane capacitance was similar (SOM: 27.6 ± 3.5 pF; $EYFP^-$: 30.9 ± 2.1 pF; $t(53) = 0.79$, $p = 0.43$, two-sample t test). In addition, SOM INs had a significantly higher spontaneous firing rate than PCs (SOM: 2.0 ± 0.6 Hz, $n = 10$ cells; $EYFP^-$: 0.4 ± 0.4 Hz, $n = 6$ cells; $U = 7$, $p = 0.015$, exact Mann-Whitney U test). In keeping with their electrical compactness, cell-attached recordings from spontaneously active SOM INs in the absence of antagonists confirmed that $HR3^{SOM}$-mediated photo-currents reduced AC frequency to 25.4% ± 7.9% of baseline ($p = 6.0 \times 10^{-6}$, $n = 10$ cells, one-sample t test on normalized data; Figures 4C and 4D; Table S5). We then asked whether SOM INs contribute to spontaneous GABA release onto $EYFP^-$ PCs. In the presence of DNQX and APV, photo-stimulation of $HR3^{SOM}$ significantly reduced the frequency of $GABA_A$R-mediated PSCs (GPSCs) to 67.1% ± 5.6% (baseline: 1.9 ± 0.4 Hz; stim: 1.3 ± 0.2 Hz; $p = 4.2 \times 10^{-3}$, $n = 5$ cells, one-sample t test on normalized data; Figures 4E and 4F). Hence, SOM INs constitute a major GABAergic synaptic input to PCs.

In the absence of blockers, bursts of mixed GABAergic and glutamatergic PSCs were apparent in voltage-clamp recordings from PCs (Figure 4G). Since photo-stimulation of $HR3^{SOM}$ prohibited the use of Ca^{2+} imaging as a readout of activity, we investigated whether PSC bursts could serve as a surrogate of GDPs. In simultaneous Ca^{2+} imaging and electrophysiological measurements, PSC bursts were typically accompanied by CaTs in many CA1 cells (Figure 4G). The active cell fraction per PSC burst amounted to 48.9% ± 9.7%, which was higher than that for randomly shuffled events (9.2% ± 1.6%, $p = 5.2 \times 10^{-3}$, $n = 7$ cells, paired t test; Figure 4H; Table S5). Hence, we used whole-cell recordings from PCs for further quantification. Photo-stimulation of $HR3^{SOM}$ (30 s) decreased PSC frequency to 72.1% ± 5.5% (baseline: 2.5 ± 0.6 Hz, $p = 3.9 \times 10^{-3}$, $n = 10$ cells, exact one-sample Wilcoxon signed-rank test on normalized data; Figures 4I–4K). After terminating photo-inhibition of SOM INs, PSC frequency transiently increased to 465% ± 98% of the pre-stimulus level ($p = 2.0 \times 10^{-3}$, $W = 55$, exact one-sample Wilcoxon signed-rank test on normalized data; Figures 4I and 4J). This was paralleled by a rebound increase in SOM IN firing in independent experiments (Figure 4D). Under baseline conditions, PSC bursts were detected in eight out of 10 cells at a rate of 2.0 ± 0.4 min^{-1}. Photo-stimulation of $HR3^{SOM}$ reduced the frequency of PSC bursts to 71% ± 12% of baseline ($p = 0.047$, $n = 8$ cells, exact one-sample Wilcoxon signed-rank test on normalized data; Figures 4I and 4K). In slices in which CA3 had been disconnected from CA1, this effect tended to be more variable (PSC bursts were reduced to 80% ± 21%; $n = 10$ cells; Figures S3D and S3E) but was not significantly different from that in naive slices (interaction term [stimulation × intact/cut CA3 to CA1]: $p = 0.39$; stim: $p = 0.035$, mixed-model ANOVA; Table S4). Hence, a considerable fraction of PSC bursts that persisted under photo-stimulation of $HR3^{SOM}$ in naive slices was not driven by CA3. Relieving SOM INs from inhibition temporarily potentiated the rate of PSC bursts to 890% ± 190% of the pre-stimulus level in naive slices (within 2.5 s after stimulation offset, $p = 4.1 \times 10^{-3}$, $t(7) = 4.2$, one-sample t test on normalized data; Figure 4I). Thus, we conclude that spontaneous GABA release from SOM INs promotes GDP generation in CA1.

A Neural Network Model with Excitatory GABA Accounts for Major Experimental Observations

Using a recently established developing recurrent neural network model (RNN) (Rahmati et al., 2017), we investigated whether we can qualitatively reproduce and reveal mechanistic

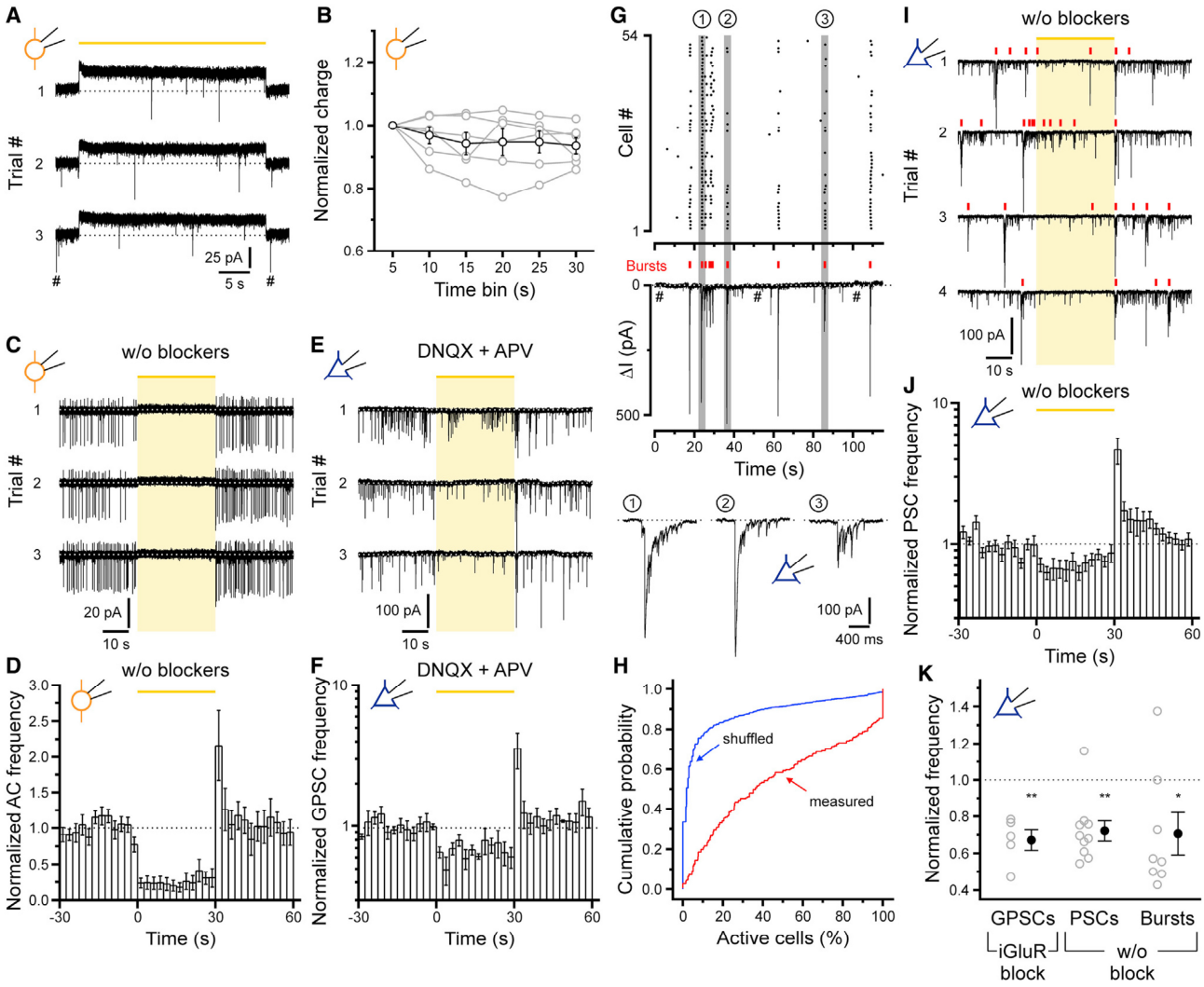

Figure 4. Spontaneous GABA Release from SOM INs Promotes GDP Activity

(A) eNpHR3.0-EYFP was conditionally expressed in SOM INs. Photo-stimulation at 594/488 nm (yellow) induced outward currents in SOM INs. Clipped PSCs are indicated (#).

(B) Normalized mean eNpHR3.0-mediated currents (bin length, 5 s).

(C) Sample cell-attached recording from a spontaneously active SOM IN.

(D) AC frequency in SOM INs normalized to the pre-stimulation period (n = 10 cells).

(E) Sample whole-cell recording from a PC in DNQX and APV.

(F) GPSC frequency normalized to the pre-stimulation period (n = 5 cells).

(G) Sample raster plot indicating somatic CaTs (top) and time-aligned voltage-clamp recording from a PC revealing coincident PSC bursts. Current responses to voltage steps used to monitor passive properties were clipped (#). Bottom: sample PSC bursts at higher temporal resolution.

(H) Distributions of active cell fractions per PSC burst for measured and shuffled bursts (n = 221 bursts from seven slices).

(I) Sample traces in the absence of receptor antagonists.

(J) PSC frequency normalized to the pre-stimulation period (n − 10 cells).

(K) Photo-stimulation of $HR3^{SOM}$ reduced the frequency of GABAergic (iGluR block, GPSCs) and mixed GABAergic and glutamatergic (without block) PSCs and PSC bursts. Each gray symbol represents a single cell and slice.

Data represent mean ± SEM. *p < 0.05; **p < 0.01. See also Figure S3 and Table S5.

insights into our experimental observations. The network is a mean-field model of activity rates of two populations of glutamatergic (PC) and GABAergic (SOM) cells with short-term synaptic plasticity (STP-RNN; Figure 5A), here parameterized with excitatory GABA and depressing synapses. We found that a perturbation of the SOM population, when applied at the network's rest state, was amplified profoundly, leading to population spikes (Figures 5B) that are analogous to experimentally observed GDPs (Figures 3B and 3D). The duration of simulated GDPs (simGDPs) was comparable (~400 ms) to that of

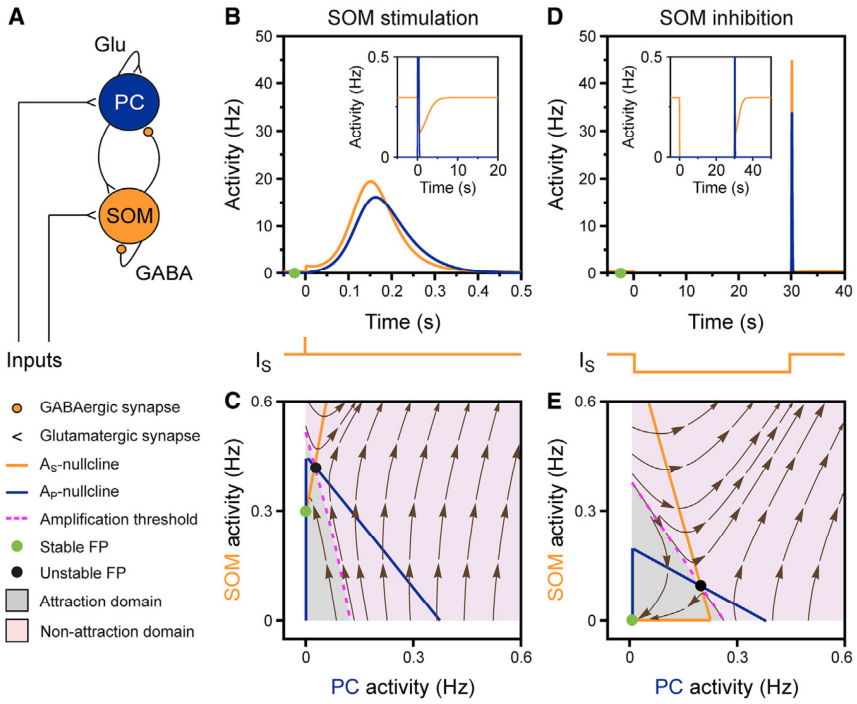

Figure 5. An STP-RNN Model with Excitatory GABA Emulates Major Experimental Observations

(A) Graph representing the STP-RNN.

(B) A simGDP is triggered by a perturbation of the SOM population at time t = 0 ($I_s(t=0) = 30$ Hz), when the STP-RNN was operating at its rest state (green dot).

(C) An unstable fixed point (FP) hidden in the network firing activity enables simGDP emergence. The $A_s - A_p$-plane of the STP-RNN with frozen synaptic efficacies at the rest state. The gray and purple regions belong to the attraction and amplification domains of the stable rest state in the Frozen STP-RNN. Both are attraction domains of the stable rest state in the STP-RNN. Activities initiated in the amplification domain initiate a simGDP in the non-frozen STP-RNN.

(D) A rebound simGDP emerged following the release from inhibition applied to the SOM population for 30 s ($I_s = -0.5$ Hz).

(E) SOM IN activity regulates amplification threshold; same as in (C), but synapses were frozen at the new stable FP at the origin (during inhibition of SOM INs).

Insets in (B) and (D) show network activity at longer timescales. Brown streamlines show the local direction of example trajectories in the corresponding Frozen STP-RNN. See also Figures S4 and S5.

experimentally measured GDPs. In the absence of external input, the network is a mono-stable system operating at its rest state (green dots in Figures 5B and 5C), where the spontaneous average activity rate of SOM INs (A_s) exceeds that of PCs (A_p), as observed in cell-attached measurements. In the model, this difference is mainly due to a higher membrane resistance of SOM INs, in line with our experimental data. To investigate the mechanism of simGDP emergence, we plotted the $A_s - A_p$-plane of the network with slow STP dynamics frozen at the rest state (Frozen STP-RNN; Figure 5C; STAR Methods). We found that an unstable fixed point (FP; black dots in A_s; Figures 5C and 5E) is hidden in the network's fast dynamics, which does not exist in the non-frozen STP-RNN (Rahmati et al., 2017). This unstable FP, which disappears after the peak of the simGDPs, enables the emergence of simGDPs by building an amplification threshold (magenta line, Figure 5C) in the initial activity phase of the STP-RNN operating at its rest state. The simGDPs can be effectively triggered only if the perturbation is sufficiently strong enough to push activity of the STP-RNN beyond the amplification threshold (Figure 5C) (Rahmati et al., 2017). This underlies a relatively all-or-none characteristic of simGDPs, which is a well-known property of experimentally measured GDPs.

We next simulated a decrease in the excitatory effect of GABA due to NKCC1 inhibition. A gradual decrease in the average absolute synaptic efficacy of GABAergic synapses ($|J_s|$) led to a potent reduction in the size of simGDPs evoked by a perturbation of either the SOM or the PC population (Figures S4A and S4B). This manipulation decreased the spontaneous A_s (Figure S4A), as in our experimental data (Figure 1F), and shifted the amplification threshold upward and to the right (Figure S4C). This shift implies that triggering simGDPs in the model requires a stronger input and can explain the decrease in fGDP frequency induced by bumetanide (Figures 1F and 1L). These findings disclose a contribution of GABAergic excitation by SOM INs to network instability that is essential for (sim)GDP emergence. We then selectively eliminated either SOM-SOM or PC-PC connections by zeroing their absolute synaptic efficacies (J_{ss} and J_{pp}, respectively; Figure S5A). Setting $J_{pp} = 0$ reduced the size of simGDPs evoked by perturbing either SOM INs or PCs and shifted the amplification threshold upward and to the right (Figure S5). In contrast, setting $J_{ss} = 0$ had only minor effects (Figure S5). The fact that simGDPs can emerge even when $J_{ss} = 0$ or $J_{pp} = 0$ points to an important role of reciprocal PC-SOM synaptic connections. Indeed, eliminating PC-SOM connectivity ($J_{sp} = 0$) strongly attenuated simGDPs and shifted the amplification threshold upward and to the right (Figure S5).

In the model, inhibition of the SOM population for 30 s diminished the spontaneous A_s, and the release from inhibition was followed by a rebound simGDP involving both SOM INs and PCs (Figure 5D), thus resembling our experimental data (Figure 4). This behavior results from a downward shift in the amplification threshold during inhibition, rendering the SOM population's activity more prone to the amplification domain at the time of inhibition release (purple region in Figure 5E). Besides, inhibition of SOM INs shifted the amplification threshold to the right (Figures 5C and 5E), indicating that initiating simGDPs by the PC population may require a stronger input as compared to baseline. This explains the experimentally observed decrease in spontaneous GDP frequency during inhibition (Figures 4I and 4K) and may also suggest that the

GDP-initiating inputs preferentially target PCs rather than SOM INs. In sum, modeling results demonstrate an effective contribution of SOM INs to GDP emergence, mainly through a modulation of network instability and amplification threshold.

DISCUSSION

SOM INs Are Crucial Components of the Neonatal Hippocampal Circuitry

Here, we focused on SOM INs that are genetically accessible by the expression of SOM and cre recombinase in *SOM*^{IREScre} mice (Taniguchi et al., 2011). SOM INs are a heterogeneous GABAergic cell class. They include distal dendrite-targeting *oriens-lacunosum moleculare* (OLM) cells (Chittajallu et al., 2013); bistratified INs mainly synapsing on proximal dendrites (Klausberger et al., 2004); long-distance projecting cells (Gulyás et al., 2003); and, partially overlapping, a subpopulation of super-connected hub cells (Mòdol et al., 2017; Picardo et al., 2011). Moreover, in the adult, a small fraction of *SOM*^{IREScre}-expressing cells are fast-spiking INs containing parvalbumin (Hu et al., 2013). In all PCs examined here, ChR2^{SOM} stimulation evoked PSCs that were abolished by blocking $GABA_A$Rs (Figure 2), confirming that SOM INs establish GABAergic outputs by P1–P4. Though not explicitly addressed, this finding indirectly implies that PSCs induced by SOM INs are not mediated by $GABA_B$Rs, which may contribute to GDP termination via hyperpolarization in neonates (Khalilov et al., 2017). SOM INs account for a sizeable fraction of GPSCs in PCs, since their optogenetic inhibition reduced GPSC frequency by ~30% (Figure 4K). This value is a lower limit estimate, as (1) the HR3^{SOM}-mediated silencing was incomplete (Figure 4D) and (2) GPSCs also comprise action-potential-independent (miniature) GABA release, presumably less affected by HR3^{SOM}. Thus, our data extend previous results, which had revealed that MGE-derived GABAergic INs establish synapses with PCs (Wester and McBain, 2016) and Cajal-Retzius cells (Quattrocolo and Maccaferri, 2013) by P14. An important open question relates to the activation of neonatal SOM INs. Mature SOM INs receive dense input from CA1 PCs (Ali and Thomson, 1998) and additionally express metabotropic glutamate receptors (mGluR1s) (Ferraguti et al., 2004), which can generate inward currents and potentially underlie tonic excitation (McBain et al., 1994). However, it is unknown whether these mechanisms are operative shortly after birth.

SOM IN-Dependent GABAergic Control of Correlated Network Activity

Several forms of oscillations in the adult brain are promoted by synaptic inhibition. For example, GABA released from cortical Martinotti cells may synchronize PCs via hyperpolarization and rebound spiking (Hilscher et al., 2017). Here, we demonstrate that neonatal CA1 SOM INs rely on a diametrically opposed mechanism that uses postsynaptic excitation. In addition to correlative evidence (Figure 1), this conclusion is causally supported by the following findings: (1) GABA release from SOM INs can excite CA1 PCs (Figure 2) and elicit GDPs (Figure 3); (2) NKCC1 inhibition attenuates the synchronizing capacity of SOM INs (Figure 3); and (3) an excitatory, but not an inhibitory, action of GABA at SOM-PC synapses lowers the network amplification threshold, thus facilitating simGDP generation (Figures 5 and S4). As to which extent subclasses of SOM INs have differential effects, this remains incompletely understood. Interestingly, GABAergic hub cells (many of which express SOM) were reported to affect network dynamics in multiple ways, including an increase or decrease of GDP frequency or GDP phase shifts (Picardo et al., 2011), thus indicating converging and diverging mechanisms of how GABAergic INs may modulate synchrony. Modeling further revealed that the effects of SOM INs are strongly dependent on SOM-PC connections, whereas SOM-SOM connectivity has a minor role (Figure S5). Interestingly, ablation of GABAergic INs in neonatal mice attenuated hippocampal network activity *in vivo* (Bitzenhofer and Hanganu-Opatz, 2014), pointing to a synchronizing effect of GABA in the intact brain. In our study, photo-inhibition of SOM INs was considerably less effective in inhibiting GDPs than was the blocking of NKCC1 (Figures 1 and 4). While this discrepancy may result from incomplete silencing, it suggests that other sources of GABA contribute to the drive of network synchrony. Clearly, further work is required to unravel the functions of distinct subtypes of GABAergic INs *in vivo*.

It was proposed that GABA promotes neuronal synchrony via temporally precise (Khazipov et al., 1997) or non-patterned (Sipilä et al., 2005) $GABA_A$R activation. Our data converge to suggest that both mechanisms could contribute to the synchronizing capacity of SOM INs. First, SOM IN activation induced time-locked GPSCs in PCs (Figure 2) and triggered GDPs (Figure 3). This effect was qualitatively reproduced in a reductionist STP-RNN model with excitatory GABA (Figures 5 and S4). Second, the model predicts that a tonic, temporally unstructured decrease in the mean firing rate of SOM INs elevates the network amplification threshold (Figure 5), rendering GDP initiation more difficult. Accordingly, silencing SOM INs reduced the frequency of PSC bursts (Figure 4). In sum, while a coordinated activation of SOM INs may trigger GDPs, a change in their average spontaneous activity might suffice to modulate the probability of GDP generation. In the model, releasing SOM INs from inhibition resulted in a rebound simGDP involving both SOM INs and PCs, only if GABAergic synapses were excitatory (Figure 5D). A similar behavior was observed in experiments (Figure 4), in line with a recent study (Wester and McBain, 2016). Together, these data explain rebound GDPs as primary network effects, although additional factors (e.g., an HR3^{SOM}-dependent shift in chloride reversal potential, activation of voltage-dependent conductances) may contribute as well.

In conclusion, our study reveals a crucial contribution of SOM INs to correlated network activity in the neonatal hippocampus. Thus, our findings have important implications for the understanding of how neuronal activity sculpts brain circuits during development.

STAR★METHODS

Detailed methods are provided in the online version of this paper and include the following:

- KEY RESOURCES TABLE
- CONTACT FOR REAGENT AND RESOURCE SHARING

SUPPLEMENTAL INFORMATION

Supplemental Information can be found with this article online at https://doi.org/10.1016/j.celrep.2019.02.061.

ACKNOWLEDGMENTS

We thank Chuanqiang Zhang and Jürgen Graf for comments, Ina Ingrisch for technical assistance, and Dr. John Dempster (Glasgow) for adapting WinFluor. This work was supported by the Priority Program 1665 (HO 2156/3–1/2 to K.H., KI 1816/1–1/2 to K.K., and KI 1638/3–2 to S.J.K.); the Collaborative Research Center/Transregio 166 (B3 to K.H. and K.K.) and the Research Unit 1738 (WI 830/10–2 to O.W.W. and K.H.) of the German Research Foundation; the Bernstein Focus (01GQ0923 to K.H. and O.W.W.) of the Federal Ministry of Education and Research; and the Interdisciplinary Centre for Clinical Research Jena (to K.K., K.H., and T.K.).

AUTHOR CONTRIBUTIONS

K.K. and K.H. designed research, with contributions from all authors. T.F. and T.K. performed experiments. T.F., T.K., V.R., and K.K. analyzed data. V.R. designed the model and ran the simulations. All authors participated in the interpretation of data. K.K., T.F., K.H., V.R., and S.J.K. wrote the paper, with contributions from all authors.

DECLARATION OF INTERESTS

The authors declare no competing interests.

Received: June 13, 2018
Revised: December 18, 2018
Accepted: February 13, 2019
Published: March 19, 2019

REFERENCES

Ackman, J.B., Burbridge, T.J., and Crair, M.C. (2012). Retinal waves coordinate patterned activity throughout the developing visual system. Nature *490*, 219–225.

Ali, A.B., and Thomson, A.M. (1998). Facilitating pyramid to horizontal oriens-alveus interneurone inputs: dual intracellular recordings in slices of rat hippocampus. J. Physiol. *507*, 185–199.

Anastasiades, P.G., Marques-Smith, A., Lyngholm, D., Lickiss, T., Raffiq, S., Kätzel, D., Miesenböck, G., and Butt, S.J. (2016). GABAergic interneurons form transient layer-specific circuits in early postnatal neocortex. Nat. Commun. *7*, 10584.

Ben-Ari, Y., Cherubini, E., Corradetti, R., and Gaiarsa, J.L. (1989). Giant synaptic potentials in immature rat CA3 hippocampal neurones. J. Physiol. *416*, 303–325.

Bitzenhofer, S.H., and Hanganu-Opatz, I.L. (2014). Oscillatory coupling within neonatal prefrontal-hippocampal networks is independent of selective removal of GABAergic neurons in the hippocampus. Neuropharmacology *77*, 57–67.

Blanquie, O., Yang, J.W., Kilb, W., Sharopov, S., Sinning, A., and Luhmann, H.J. (2017). Electrical activity controls area-specific expression of neuronal apoptosis in the mouse developing cerebral cortex. eLife *6*, e27696.

Chittajallu, R., Craig, M.T., McFarland, A., Yuan, X., Gerfen, S., Tricoire, L., Erkkila, B., Barron, S.C., Lopez, C.M., Liang, B.J., et al. (2013). Dual origins of functionally distinct O-LM interneurons revealed by differential 5-HT(3A)R expression. Nat. Neurosci. *16*, 1598–1607.

Dzhala, V.I., Talos, D.M., Sdrulla, D.A., Brumback, A.C., Mathews, G.C., Benke, T.A., Delpire, E., Jensen, F.E., and Staley, K.J. (2005). NKCC1 transporter facilitates seizures in the developing brain. Nat. Med. *11*, 1205–1213.

Easton, C.R., Weir, K., Scott, A., Moen, S.P., Barger, Z., Folch, A., Hevner, R.F., and Moody, W.J. (2014). Genetic elimination of GABAergic neurotransmission reveals two distinct pacemakers for spontaneous waves of activity in the developing mouse cortex. J. Neurosci. *34*, 3854–3863.

Ferraguti, F., Cobden, P., Pollard, M., Cope, D., Shigemoto, R., Watanabe, M., and Somogyi, P. (2004). Immunolocalization of metabotropic glutamate receptor 1alpha (mGluR1alpha) in distinct classes of interneuron in the CA1 region of the rat hippocampus. Hippocampus *14*, 193–215.

Grantyn, R., Henneberger, C., Jüttner, R., Meier, J.C., and Kirischuk, S. (2011). Functional hallmarks of GABAergic synapse maturation and the diverse roles of neurotrophins. Front. Cell. Neurosci. *5*, 13.

Gulyás, A.I., Hájos, N., Katona, I., and Freund, T.F. (2003). Interneurons are the local targets of hippocampal inhibitory cells which project to the medial septum. Eur. J. Neurosci. *17*, 1861–1872.

Hilscher, M.M., Leão, R.N., Edwards, S.J., Leão, K.E., and Kullander, K. (2017). Chrna2-Martinotti cells synchronize layer 5 type A pyramidal cells via rebound excitation. PLoS Biol. *15*, e2001392.

Hu, H., Cavendish, J.Z., and Agmon, A. (2013). Not all that glitters is gold: off-target recombination in the somatostatin-IRES-Cre mouse line labels a subset of fast-spiking interneurons. Front. Neural Circuits *7*, 195.

Iyer, K.K., Roberts, J.A., Hellström-Westas, L., Wikström, S., Hansen Pupp, I., Ley, D., Vanhatalo, S., and Breakspear, M. (2015). Cortical burst dynamics predict clinical outcome early in extremely preterm infants. Brain *138*, 2206–2218.

Khalilov, I., Minlebaev, M., Mukhtarov, M., Juzekaeva, E., and Khazipov, R. (2017). Postsynaptic GABA(B) receptors contribute to the termination of giant depolarizing potentials in CA3 neonatal rat hippocampus. Front. Cell. Neurosci. *11*, 179.

Khazipov, R., Leinekugel, X., Khalilov, I., Gaiarsa, J.L., and Ben-Ari, Y. (1997). Synchronization of GABAergic interneuronal network in CA3 subfield of neonatal rat hippocampal slices. J. Physiol. *498*, 763–772.

Khazipov, R., Sirota, A., Leinekugel, X., Holmes, G.L., Ben-Ari, Y., and Buzsáki, G. (2004). Early motor activity drives spindle bursts in the developing somatosensory cortex. Nature *432*, 758–761.

Kirmse, K., Witte, O.W., and Holthoff, K. (2010). GABA depolarizes immature neocortical neurons in the presence of the ketone body ß-hydroxybutyrate. J. Neurosci. *30*, 16002–16007.

Kirmse, K., Kummer, M., Kovalchuk, Y., Witte, O.W., Garaschuk, O., and Holthoff, K. (2015). GABA depolarizes immature neurons and inhibits network activity in the neonatal neocortex in vivo. Nat. Commun. *6*, 7750.

Kirmse, K., Hübner, C.A., Isbrandt, D., Witte, O.W., and Holthoff, K. (2018). GABAergic transmission during brain development: multiple effects at multiple stages. Neuroscientist *24*, 36–53.

Klausberger, T., Márton, L.F., Baude, A., Roberts, J.D., Magill, P.J., and Somogyi, P. (2004). Spike timing of dendrite-targeting bistratified cells during hippocampal network oscillations in vivo. Nat. Neurosci. *7*, 41–47.

Kummer, M., Kirmse, K., Zhang, C., Haueisen, J., Witte, O.W., and Holthoff, K. (2016). Column-like Ca(2+) clusters in the mouse neonatal neocortex revealed by three-dimensional two-photon Ca(2+) imaging in vivo. Neuroimage *138*, 64–75.

Leinekugel, X., Khazipov, R., Cannon, R., Hirase, H., Ben-Ari, Y., and Buzsáki, G. (2002). Correlated bursts of activity in the neonatal hippocampus in vivo. Science *296*, 2049–2052.

McBain, C.J., DiChiara, T.J., and Kauer, J.A. (1994). Activation of metabotropic glutamate receptors differentially affects two classes of hippocampal interneurons and potentiates excitatory synaptic transmission. J. Neurosci. *14*, 4433–4445.

Mòdol, L., Sousa, V.H., Malvache, A., Tressard, T., Baude, A., and Cossart, R. (2017). Spatial embryonic origin delineates GABAergic hub neurons driving network dynamics in the developing entorhinal cortex. Cereb. Cortex *27*, 4649–4661.

Oh, W.C., Lutzu, S., Castillo, P.E., and Kwon, H.B. (2016). De novo synaptogenesis induced by GABA in the developing mouse cortex. Science *353*, 1037–1040.

Pelkey, K.A., Chittajallu, R., Craig, M.T., Tricoire, L., Wester, J.C., and McBain, C.J. (2017). Hippocampal GABAergic inhibitory interneurons. Physiol. Rev. *97*, 1619–1747.

Pfeffer, C.K., Stein, V., Keating, D.J., Maier, H., Rinke, I., Rudhard, Y., Hentschke, M., Rune, G.M., Jentsch, T.J., and Hübner, C.A. (2009). NKCC1-dependent GABAergic excitation drives synaptic network maturation during early hippocampal development. J. Neurosci. *29*, 3419–3430.

Picardo, M.A., Guigue, P., Bonifazi, P., Batista-Brito, R., Allene, C., Ribas, A., Fishell, G., Baude, A., and Cossart, R. (2011). Pioneer GABA cells comprise a subpopulation of hub neurons in the developing hippocampus. Neuron *71*, 695–709.

Quattrocolo, G., and Maccaferri, G. (2013). Novel GABAergic circuits mediating excitation/inhibition of Cajal-Retzius cells in the developing hippocampus. J. Neurosci. *33*, 5486–5498.

Rahmati, V., Kirmse, K., Holthoff, K., Schwabe, L., and Kiebel, S.J. (2017). Developmental emergence of sparse coding: a dynamic systems approach. Sci. Rep. *7*, 13015.

Sipilä, S.T., Huttu, K., Soltesz, I., Voipio, J., and Kaila, K. (2005). Depolarizing GABA acts on intrinsically bursting pyramidal neurons to drive giant depolarizing potentials in the immature hippocampus. J. Neurosci. *25*, 5280–5289.

Stark, E., Roux, L., Eichler, R., Senzai, Y., Royer, S., and Buzsáki, G. (2014). Pyramidal cell-interneuron interactions underlie hippocampal ripple oscillations. Neuron *83*, 467–480.

Sulis Sato, S., Artoni, P., Landi, S., Cozzolino, O., Parra, R., Pracucci, E., Trovato, F., Szczurkowska, J., Luin, S., Arosio, D., et al. (2017). Simultaneous two-photon imaging of intracellular chloride concentration and pH in mouse pyramidal neurons in vivo. Proc. Natl. Acad. Sci. USA *114*, E8770–E8779.

Taniguchi, H., He, M., Wu, P., Kim, S., Paik, R., Sugino, K., Kvitsiani, D., Fu, Y., Lu, J., Lin, Y., et al. (2011). A resource of Cre driver lines for genetic targeting of GABAergic neurons in cerebral cortex. Neuron *71*, 995–1013.

Tolner, E.A., Sheikh, A., Yukin, A.Y., Kaila, K., and Kanold, P.O. (2012). Subplate neurons promote spindle bursts and thalamocortical patterning in the neonatal rat somatosensory cortex. J. Neurosci. *32*, 692–702.

Tsodyks, M., Pawelzik, K., and Markram, H. (1998). Neural networks with dynamic synapses. Neural Comput. *10*, 821–835.

Tuncdemir, S.N., Wamsley, B., Stam, F.J., Osakada, F., Goulding, M., Callaway, E.M., Rudy, B., and Fishell, G. (2016). Early somatostatin interneuron connectivity mediates the maturation of deep layer cortical circuits. Neuron *89*, 521–535.

Tyzio, R., Allene, C., Nardou, R., Picardo, M.A., Yamamoto, S., Sivakumaran, S., Caiati, M.D., Rheims, S., Minlebaev, M., Milh, M., et al. (2011). Depolarizing actions of GABA in immature neurons depend neither on ketone bodies nor on pyruvate. J. Neurosci. *31*, 34–45.

Vanhatalo, S., Palva, J.M., Andersson, S., Rivera, C., Voipio, J., and Kaila, K. (2005). Slow endogenous activity transients and developmental expression of K+-Cl- cotransporter 2 in the immature human cortex. Eur. J. Neurosci. *22*, 2799–2804.

Villette, V., Guigue, P., Picardo, M.A., Sousa, V.H., Leprince, E., Lachamp, P., Malvache, A., Tressard, T., Cossart, R., and Baude, A. (2016). Development of early-born γ-aminobutyric acid hub neurons in mouse hippocampus from embryogenesis to adulthood. J. Comp. Neurol. *524*, 2440–2461.

Wester, J.C., and McBain, C.J. (2016). Interneurons differentially contribute to spontaneous network activity in the developing hippocampus dependent on their embryonic lineage. J. Neurosci. *36*, 2646–2662.

Winnubst, J., Cheyne, J.E., Niculescu, D., and Lohmann, C. (2015). Spontaneous activity drives local synaptic plasticity in vivo. Neuron *87*, 399–410.

Yamada, J., Okabe, A., Toyoda, H., Kilb, W., Luhmann, H.J., and Fukuda, A. (2004). Cl- uptake promoting depolarizing GABA actions in immature rat neocortical neurones is mediated by NKCC1. J. Physiol. *557*, 829–841.

Yang, J.W., Hanganu-Opatz, I.L., Sun, J.J., and Luhmann, H.J. (2009). Three patterns of oscillatory activity differentially synchronize developing neocortical networks in vivo. J. Neurosci. *29*, 9011–9025.

Zhang, J., Ackman, J.B., Xu, H.P., and Crair, M.C. (2011). Visual map development depends on the temporal pattern of binocular activity in mice. Nat. Neurosci. *15*, 298–307.

STAR★METHODS

KEY RESOURCES TABLE

REAGENT or RESOURCE	SOURCE	IDENTIFIER
Antibodies		
Rabbit polyclonal anti-Satb2	Abcam	Cat #: ab34735; RRID: AB_2301417
Donkey anti-rabbit Alexa Fluor 488	Thermo Fisher Scientific	Cat #: A-21206; RRID: AB_141708
Chemicals, Peptides, and Recombinant Proteins		
1(S),9(R)-(−)-Bicuculline methiodide	Sigma-Aldrich	CAS #: 40709-69-1; Cat #: 14343
Gabazine (SR-95531)	Sigma-Aldrich	CAS #: 104104-50-9; Cat #: S106
Bumetanide	Sigma-Aldrich	CAS #: 28395-03-1; Cat #: B3023
DL-2-amino-5-phosphonopentanoic acid (APV)	Tocris	CAS #: 76326-31-3; Cat #: 0105
6,7-dinitroquinoxaline-2,3(1H,4H)-dione (DNQX)	Tocris	CAS #: 2379-57-9; Cat #: 0189
Tetrodotoxin citrate (TTX)	Biotrend	CAS #: 18660-81-6; Cat #: BN0518
Experimental Models: Organisms/Strains		
SOM^{IREScre} (*Sst*$^{tm2.1(cre)Zjh}$/J)	The Jackson Laboratory	Stock #: 013044
Emx1^{IREScre} (B6.129S2-*Emx1*$^{tm1(cre)Krj}$/J)	The Jackson Laboratory	Stock #: 005628
Ai96 (B6;129S6-*Gt(ROSA)26Sor*$^{tm96(CAG-GCaMP6s)Hze}$/J)	The Jackson Laboratory	Stock #: 024106
Ai32 (B6.Cg-*Gt(ROSA)26Sor*$^{tm32(CAG-COP4*H134R/EYFP)Hze}$/J)	The Jackson Laboratory	Stock #: 024109
Ai39 (B6;129S-*Gt(ROSA)26Sor*$^{tm39(CAG-hop/EYFP)Hze}$/J)	The Jackson Laboratory	Stock #: 014539
Ai14 (B6;129S6-*Gt(ROSA)26Sor*$^{tm14(CAG-tdTomato)Hze}$/J)	The Jackson Laboratory	Stock #: 007908
C57BL/6J	The Jackson Laboratory	Stock #: 000664
Software and Algorithms		
OriginPro	OriginLab	N/A
SPSS Statistics	IBM	N/A
MATLAB	MathWorks	N/A
Mathematica	Wolfram Research	N/A
ImageJ	https://imagej.net/	N/A
pClamp	Molecular Devices	N/A
Winfluor 3.7.5	J. Dempster, University of Strathclyde Glasgow	N/A
Excel	Microsoft	N/A

CONTACT FOR REAGENT AND RESOURCE SHARING

Further information and requests for resources and reagents should be directed to and will be fulfilled by the Lead Contact, Knut Kirmse (knut.kirmse@med.uni-jena.de).

EXPERIMENTAL MODEL AND SUBJECT DETAILS

A detailed list of mouse strains used in this study is provided in the key resources table. All experimental procedures were carried out with approval from the local government and complied with European Union norms (Directive 2010/63/EU). Experiments were performed on acute brain slices prepared from mice of both sexes at postnatal day (P) 1–5. Animals were housed in standard cages with 12 h light/12 h dark cycles. SOM IN-specific expression of the genetically encoded Ca^{2+} indicator GCaMP6s, either of the optogenetic actuators eNpHR3.0 or ChR2(H134R) or the fluorescent reporter tdTomato was achieved by crossing homozygous *SOM*^{IREScre} mice (The Jackson Laboratory, stock no. 013044) to homozygous mice of one of the following cre-reporting strains: *GCaMP6s*^{LSL} (Ai96, The Jackson Laboratory, stock no. 024106), *ChR2(H134R)-EYFP*^{LSL} (Ai32, The Jackson Laboratory, stock no. 024109), *eNpHR3.0-EYFP*^{LSL} (Ai39, The Jackson Laboratory, stock no. 014539) or *tdTomato*^{LSL} (Ai14, The Jackson Laboratory, stock no. 007908). PC-specific expression of GCaMP6s was obtained by crossing homozygous *Emx1*^{IREScre} females (The Jackson Laboratory, stock no. 005628) to homozygous *GCaMP6s*^{LSL} male mice. Additional experiments were performed on slices of C57BL/6J mice.

METHOD DETAILS

Preparation of brain slices

Animals were decapitated under deep isoflurane anesthesia. The brain was removed quickly and transferred into ice-cold saline containing (in mM): 125 NaCl, 4 KCl, 10 glucose, 1.25 NaH_2PO_4, 25 $NaHCO_3$, 0.5 $CaCl_2$, and 2.5 $MgCl_2$, bubbled with 5% CO_2/95% O_2 (pH, 7.4). Horizontal brain slices containing the hippocampus (350 μm) were cut on a vibratome and stored for at least 1 h before their use at room temperature in artificial cerebrospinal fluid (ACSF) containing (in mM): 125 NaCl, 4 KCl, 10 glucose, 1.25 NaH_2PO_4, 25 $NaHCO_3$, 2 $CaCl_2$, and 1 $MgCl_2$, bubbled with 5% CO_2/95% O_2 (pH, 7.4). For recordings, slices were placed into a submerged-type recording chamber on the microscope stage (Nikon Eclipse FN1, Nikon Instruments Inc.) equipped with near-infrared differential interference contrast optics (ACSF flow rate ~4 mL min^{-1}). In order to assess the contribution of CA3, in subsets of experiments (indicated in Results) a cut was made between CA3 and CA1 using a scalpel blade. All experiments were performed at 32–34°C.

Confocal Ca^{2+} imaging and analysis

Ca^{2+} imaging recordings were performed in hippocampal area CA1 from cells expressing the genetically encoded indicator GCaMP6s. Alternatively, cells were loaded with the membrane-permeable Ca^{2+}-indicator Oregon Green 488 BAPTA-1 AM (OGB1) using multi-cell bolus-loading in *str. pyramidale*. Fluorescence signals were acquired at ~22.5 Hz using a CSU10 Nipkow-disc scanning unit (Yokogawa Electric Corp.) in combination with a Rolera XR FAST 1394 CCD camera (QImaging Corp.) and the software Winfluor 3.7.5 (Dr. John Dempster, University of Strathclyde, Glasgow). For GCaMP6s measurements, hardware-binning (2 × 2) was applied. Excitation light at 488 nm was provided by a single wavelength solid-state laser (Sapphire CDRH-LP, Coherent) via a 16 × /0.8 NA (Nikon) or 40 × /0.8 NA (Nikon) water immersion objective, respectively. An acousto-optic tunable filter (GH18A, Gooch & Housego) was used to adjust the final laser power of excitation.

To correct for minor x-y drifts during recordings, stack registration based on template-matching was applied (ImageJ plugin by Q. Tseng). Somatic fluorescence signals were obtained from manually selected regions of interest and expressed as relative changes from resting fluorescence levels ($\Delta F/F_0$). For illustration purposes (Figure 1), F_0 was determined by over-smoothing the fluorescence traces with a median filter (width, 500 data points). Ca^{2+} transients (CaTs) were detected using a template-matching algorithm implemented in pClamp 10 (Molecular Devices), and their times of peak were defined as the times of CaT occurrence.

Network events were operationally defined as GDPs as follows: (1) CaTs were classified as GDP-related if they fell into a 500-ms-long time interval during which the fraction of active cells (i.e., cells with ≥ 1 detected CaT) was ≥ 20%. (2) Neighboring GDP-related CaTs were assigned to the same GDP if both shared a 500-ms-long time interval during which the fraction of active cells was ≥ 20%, otherwise to separate GDPs. For each GDP, active cells were ranked according to their CaT times, and GDP half-width was calculated as the difference in CaT times corresponding to the 25^{th} and 75^{th} percentiles of active cells. Pairwise Pearson correlation coefficients were determined for all possible cell pairs analyzed in a given image sequence using custom-written routines in MATLAB (MathWorks). To this end, binary CaT time-courses were first convolved with a Gaussian kernel having a standard deviation of two sampling intervals. Correlation coefficients derived from measured data were compared to those from simulated data obtained by randomly shuffling (uniform distribution; 5,000 times) CaT times of all cells. When performing this randomization, the mean CaT frequency of each cell was kept the same as the empirical one. For combined Ca^{2+} imaging and local field potential measurements, participation rate was defined, for each cell separately, as the fraction of field GDPs (fGDPs) during which the cell was active. A cell was classified as active during a given fGDP if at least one CaT was detected within the interval [fGDP peak time – 1.5 s, fGDP peak time + 1.5 s], otherwise the cell was considered inactive during the given fGDP. Chance level was determined on the basis of simulated data generated by randomly shuffling (1,000 times) fGDP times (routines written in Visual Basic and MATLAB). Only recordings with ≥ 4 fGDPs were included in the analysis of participation rates.

Electrophysiological recordings and analysis

Electrophysiological signals were acquired using a Multiclamp 700B (Molecular Devices, patch-clamp recordings) or an EXT-02F (npi electronic GmbH, extracellular measurements) amplifier, a 16-bit AD/DA board (Digidata 1550A) and the software pClamp 10.7. Signals were either low-pass filtered at 1–3 kHz and sampled at 10–50 kHz in patch-clamp studies or band-pass filtered at 0.2–1300 Hz and sampled at 20 kHz in extracellular recordings. For whole-cell recordings, glass pipettes (4–7 MΩ) were filled with the following solution (in mM): 40 KCl, 100 K^+-Gluconate, 1 $CaCl_2$, 11 EGTA, 10 HEPES, 2 Mg^{2+}-ATP, 0.3 Na^+-GTP (pH adjusted to 7.25 with KOH). In a few cases, neurobiotin (0.2%) was added for subsequent morphological characterization. Whole-cell voltage-clamp recordings were performed at a holding potential of –70 mV (not corrected for liquid junction potential). For cell-attached (seal resistance > 1 GΩ) and loose-patch measurements, recording pipettes (4–14 MΩ) contained (in mM): 150 NaCl, 4 KCl, 10 HEPES (pH adjusted to 7.4 with NaOH). In these experiments, holding current was manually zeroed, unless states otherwise. For extracellular recordings, quartz glass-insulated platinum/tungsten microelectrodes were used (EF8025, Thomas Recording GmbH). Postsynaptic currents (PSCs), action currents (ACs) and fGDPs were detected using template matching (pClamp 10). Synchronization of electrophysiological and optical signals was done using brief LED or laser light pulses. EYFP fluorescence signals were used to identify SOM INs in electrophysiological measurements.

Trains of spontaneous PSCs were operationally defined as PSC bursts as follows: (1) PSCs were classified as burst-related if they fell into a 500-ms-long time interval during which the mean PSC frequency was ≥ 20 Hz. (2) Neighboring burst-related PSCs were

assigned to the same burst if both shared a 500-ms-long time interval during which the mean PSC frequency was ≥ 20 Hz, otherwise to separate GDPs. For combined Ca^{2+} imaging (OGB1) and whole-cell voltage-clamp recordings, a CaT was considered as related to a given PSC burst if its time of peak was found in the interval [PSC burst onset – 1.5 s, PSC burst offset + 1.5 s]. The fraction of active cells during a given PSC burst was determined as the ratio of the number of active cells (i.e., cells with ≥ 1 burst-related CaT) and the total number of analyzed cells. Fractions of active cells determined for measured data were compared to those for simulated data by randomly shuffling (1,000 times) PSC bursts times (routines written in Visual Basic and MATLAB).

Optogenetic stimulation

Excitation was provided by a 488 nm diode laser (Cobolt MLD 488) and a 594 nm solid-state laser (Cobolt Mambo), intensity-modulated by an acousto-optic tunable filter (GH18A, Gooch & Housego) and coupled into a multimode 0.22 NA optical fiber (core diameter, 200 μm; FG200LCC, Thorlabs GmbH). The tip of the fiber was positioned at an axial distance of ~500 μm to the CA1 surface and approximately centered to CA1 (see Figure 2A). Note, however, that we could not entirely exclude stray light from reaching adjacent areas. For each wavelength, light power at the tip of the fiber was ~5 mW. Photo-stimulation of ChR2(H134R) was performed using single or trains of 488 nm light pulses (2 ms, 100 Hz). To minimize photo-current decay, eNpHR3.0 was stimulated in an alternating manner at 488/594 nm (1 kHz repetition rate, 50/50% duty cycle).

Immunohistochemistry

Animals were decapitated under deep isoflurane anesthesia. Brains were removed quickly and immersion-fixed in 4% paraformaldehyde (PFA) in phosphate-buffered saline (PBS) for 22 h, then cryoprotected in PBS containing 10% and 30% sucrose, respectively, frozen and stored at –80°C. Horizontal sections (40 μm) comprising the hippocampus were prepared on a cyromicrotome (HM400, Microm). Slices were washed in PBS, permeabilized with 0.2% Triton X-100 and blocked with 3% normal donkey serum (NDS) in PBS. Free-floating sections were incubated overnight with a rabbit polyclonal anti-Satb2 antibody (1:2500, Abcam, ab34735) in PBS containing 3% NDS/0.2% Triton X-100 at 4°C. Following rinsing, an Alexa Fluor 488-coupled donkey anti-rabbit antibody (1:500, ThermoFisher Scientific, A21206) was applied for 3 h at room temperature in PBS supplemented with 3% NDS/0.2% Triton X-100. Nuclei were counterstained using DAPI. After rinsing, slices were mounted on slides using Fluoromount (SouthernBiotech). Fluorescence images (z stacks) were acquired with a LSM 710 laser-scanning confocal microscope and a 20 × dry or, for quantification, 40 × oil immersion objective (Carl Zeiss) and analyzed using ImageJ.

For analysis, DAPI-stained nuclei in CA1 were semi-automatically detected using a three-dimensional template matching routine implemented in MATLAB. For each detected cell, a Satb2 fluorescence index (FI) was calculated according to the equation: $FI = (F_{soma} - F_{ref})/(F_{soma} + F_{ref})$, where F_{soma} is the fluorescence measured at the soma and F_{ref} the mean fluorescence measured in *str. pyramidale* of the respective optical section. The resulting bimodal distribution of FI values was fitted with a two-term Gaussian function. A threshold value was derived from the Gaussian term with the lower mean (corresponding to Satb2-negative cells) by computing its 99th percentile. A cell was classified as Satb2-positive, if its FI value was larger than threshold, otherwise it was considered Satb2-negative. According to this, the expected probability of false Satb2-positive cells is 1%.

Computational modeling

Overview. To model neural activity in our experimental data we adopted a recently established recurrent neural network model (RNN) (Rahmati et al., 2017). The model was shown to not only being able to emulate the experimentally observed developmental trajectory of network activity and properties but also address the underlying mechanisms, during the first postnatal month. It is an extended Wilson-Cowan-type model (Tsodyks et al., 1998) and has the advantage of being biophysically interpretable and mathematically accessible. Here, we consider the RNN proposed for the period of physiological blindness, i.e., the first postnatal week. In the following, we first provide the corresponding mathematical description of the model and then describe its phase plane components. For more details about the model and the approach see Rahmati et al. (2017).

Model description. The model is a mean-field network model of activity rates of two spatially localized, homogeneous glutamatergic and GABAergic cells (here, PC and SOM populations) that are recurrently connected (Figure 5A). The synaptic efficacies are dynamic over time due to short-term synaptic plasticity (STP) mechanisms, namely short-term synaptic depression (STD) and facilitation (STF). Hence, we call the network hereafter STP-RNN. By adapting the original equations (Rahmati et al., 2017; Tsodyks et al., 1998), we formulated the mean-field dynamics of the STP-RNN (10D) used in this paper as (dots denote the time derivatives):

$$\begin{aligned}
&\tau_p \dot{A}_p(t) = -A_p(t) + f_p(J_{pp}\, u_{pp}(t) x_{pp}(t) A_p(t) - J_{ps}\, u_{ps}(t)\, x_{ps}(t)\, A_s(t) + I_p(t)) = -A_p(t) + f_p(h_p)\\
&\tau_s \dot{A}_s(t) = -A_s(t) + f_s(J_{sp}\, u_{sp}(t) x_{sp}(t) A_p(t) - J_{ss}\, u_{ss}(t)\, x_{ss}(t) A_s(t) + I_s(t)) = -A_s(t) + f_s(h_s)\\
&\dot{x}_{ij} = \tau_{r_{ij}}^{-1}(1 - x_{ij}(t)) - u_{ij}(t)\, x_{ij}(t)\, A_j(t)\\
&\dot{u}_{ij} = \tau_{f_{ij}}^{-1}(U_{ij} - u_{ij}(t)) + U_{ij}(1 - u_{ij}(t))\, A_j(t)
\end{aligned} \tag{1}$$

where i and j$\in \{p, s\}$, and j is the index of the presynaptic population, A_p and A_s are the average activity rates (in Hz) of PC and SOM populations which can be properly scaled to represent locally the average recorded activities in these populations, x_{ij} and u_{ij} are the average dynamic variables of STD and STF mechanisms, τ_p and τ_s are approximations to the decay time constants of the glutamatergic and GABAergic postsynaptic potentials, $\tau_{r_{ij}}$ is the synaptic recovery time constant of depression, $\tau_{f_{ij}}$ is the synaptic facilitation

time constant, U_{ij} is analogous to the synaptic release probability, J_{ij} is the average maximum absolute synaptic efficacy of recurrent $(i=j)$ or feedback $(i\neq j)$ connections, and I_p and I_s are the external inputs received by the PC and SOM populations from other brain regions or stimulation. The transformation from the summed input to each population, h_i, to an activity output (in Hz) is governed by the response function, f_i, defined as (Rahmati et al., 2017):

$$f_i(h_i)=\begin{cases}0 & \text{for } h_i\leq\theta_i\\ G_i(h_i-\theta_i) & \text{for } \theta_i<h_i\end{cases} \quad (2)$$

where θ_i is the population activity threshold, and G_i is the linear input-output gain above θ_i.

To parameterize the STP-RNN as a network model belonging to the first postnatal week, we mainly followed Rahmati et al. (2017) by setting $\tau_p = 0.045$s, $\tau_s = 0.0225$s, $J_{pp} = J_{sp} = J_p = 2$, $J_{ss} = J_{ps} = J_s = -1.7$, $\tau_{r_{pp}} = \tau_{r_{sp}} = \tau_{rp} = 5.5$s, $\tau_{r_{ss}} = \tau_{r_{ps}} = \tau_{r_s} = 5$s, $\tau_{f_{pp}} = \tau_{f_{sp}} = \tau_{f_p} = 0.8$s, $\tau_{f_{ss}} = \tau_{f_{ps}} = \tau_{f_s} = 0.8$s, $U_{pp} = U_{sp} = U_p = 0.9$, $U_{ss} = U_{ps} = U_s = 0.9$, $\theta_p = 0.3$, $\theta_s = -0.1$, $G_p = G_s = 1$, and $I_p = I_s = 0$ Hz (for ongoing spontaneous activity). Note that direct experimental proof for monosynaptic SOM-to-SOM connectivity at the age investigated is currently lacking. According to these parameter values, both glutamatergic and GABAergic connections will act depressing, and GABAergic transmission will be excitatory (see Figure 2) rather than inhibitory (note the negative value of J_s). However, it will have an effectively lesser excitatory effect than glutamatergic transmission (note that $J_p > |J_s|$). We emphasize that STP mechanisms of SOM IN output synapses at P1–5 are currently unknown and depressing synapses in our model are an informed assumption by extrapolating from previous work (Grantyn et al., 2011). This assumption also provided for a useful model component in a previous study (Rahmati et al., 2017). In the model, the population activity threshold of each population effectively depends on its background input and the membrane resistance of its cells. Accordingly, our assigned values to θ_p and θ_s reflect our assumption that SOM INs, as compared to PC cells, have a higher membrane resistance and/or receive a higher mean-level of spontaneous background input, consistent with our experimental data. All parameter values are consistent throughout the paper, unless otherwise stated.

Frozen STP-RNN

A STP-RNN with frozen synaptic efficacies is called Frozen STP-RNN. For example, the corresponding Frozen STP-RNN of the stable rest state can be obtained by freezing (i.e., fixing) the STP variables x_{ij} and u_{ij} at their steady state values at the rest state. The freezing converts the STP-RNN (10D; see Equation 1) effectively to a 2D network with constant synaptic efficacies. As shown in Rahmati et al. (2017), the corresponding Frozen STP-RNN can provide a reliable approximation to the stability behavior of a STP-RNN at the fixed point (FP, see below). The equations governing the dynamics of a Frozen STP-RNN are:

$$\begin{aligned}\tau_p\dot{A}_p(t) &= -A_p(t)+f_p\left(J^{frz}_{pp}A_p(t)-J^{FP}_{PS}A_s(t)+I_P(t)\right)\\ \tau_s\dot{A}_s(t) &= -A_s(t)+f_s\left(J^{frz}_{sp}A_p(t)-J^{frz}_{ss}A_s(t)+I_s(t)\right)\end{aligned} \quad (3)$$

where $J^{frz}_{ij} = J_{ij}\,u^{frz}_{ij}\,x^{frz}_{ij}$, and u^{frz}_{ij} and x^{frz}_{ij} are the values of u_{ij} and x_{ij} (see Equation 1) at the state of interest, e.g., at the rest state of the STP-RNN.

Phase plane

Following Rahmati et al. (2017), to visualize the initial phase of the STP-RNN's activity behavior at the FP of interest we used the phase plane analysis of the Frozen STP-RNN, based on the activity rates: $A_s - A_p$-plane (2D). The $A_s - A_p$ -plane sketch includes the curves of the A_p -nullcline and A_s-nullcline representing sets of points for which $\dot{A}_p(t)=0$ and $\dot{A}_s(t)=0$ in the corresponding Frozen STP-RNN (Equation 3), respectively.

Fixed point

A fixed point (FP) is a network's steady state, with the stability behavior needed to be determined (see below). In this paper, we compute the FPs for both STP-RNNs and Frozen STP-RNNs. The FPs of the STP-RNN represents the steady states of the full network; i.e., STP-RNN (10D), see Equation 1. The FPs of a Frozen STP-RNN with synaptic efficacies frozen at a stable FP of interest in STP-RNN include essentially that FP, and possibly some other FPs which may not exist in the STP-RNN itself; see Results and Rahmati et al. (2017). The intersections of A_p-nullcline and A_s-nullcline in the $A_s - A_p$-plane also represent the FPs of the Frozen STP-RNN.

Stability of FPs

To determine the stability of any FP in the STP-RNN (resp. in the Frozen STP-RNN) we applied the linear stability analysis to its 10D (resp. 2D) system of equations in Equation 1 (resp. Equation 3): We investigated whether all eigenvalues of the corresponding Jacobian matrix have strictly negative real parts (if so, the FP is stable), or whether at least one eigenvalue with positive real part exists (if so, the FP is unstable).

simGDP size and duration

To qualitatively measure the total number of neurons synchronized during a simGDP we followed Rahmati et al. (2017) and approximated the GDP size as a dimensionless parameter: $GDP_{size} = \omega \times (A^{max}_{sum} - A^{0}_{sum})$, where the sum activity $A_{sum} = A_p + A_s$ is the sum of activity rates of the PC and SOM populations (in Hz), and A^{max}_{sum} and A^{0}_{sum} are the maximal sum activity during simGDP and the preceding activity, and $\omega = 1\ \text{Hz}^{-1}$ is a scaling factor. We measure the simGDP duration as its termination time minus its initiation time.

Simulations

All simulation results in this paper have been implemented as Mathematica and MATLAB (MathWorks) codes. For simulations, we set the integration time-step size to 0.001 s.

QUANTIFICATION AND STATISTICAL ANALYSIS

Statistical analyses were performed using OriginPro 2015/2016/2018, Microsoft Excel 2010 and SPSS Statistics 22/24. All data are reported as mean ± standard error of the mean (SEM). Unless otherwise stated, the statistical parameter n refers to the number of slices in Ca^{2+} imaging experiments and to the number of cells in electrophysiological recordings. The Shapiro-Wilk test was used to test for the normality of data. Parametric testing procedures were applied for normally distributed data; otherwise non-parametric tests were used. P values (two-tailed tests) < 0.05 were considered statistically significant. Details of the applied statistical tests are provided in Tables S1–S5.

Cell Reports, Volume *26*

Supplemental Information

Somatostatin Interneurons Promote Neuronal Synchrony in the Neonatal Hippocampus

Tom Flossmann, Thomas Kaas, Vahid Rahmati, Stefan J. Kiebel, Otto W. Witte, Knut Holthoff, and Knut Kirmse

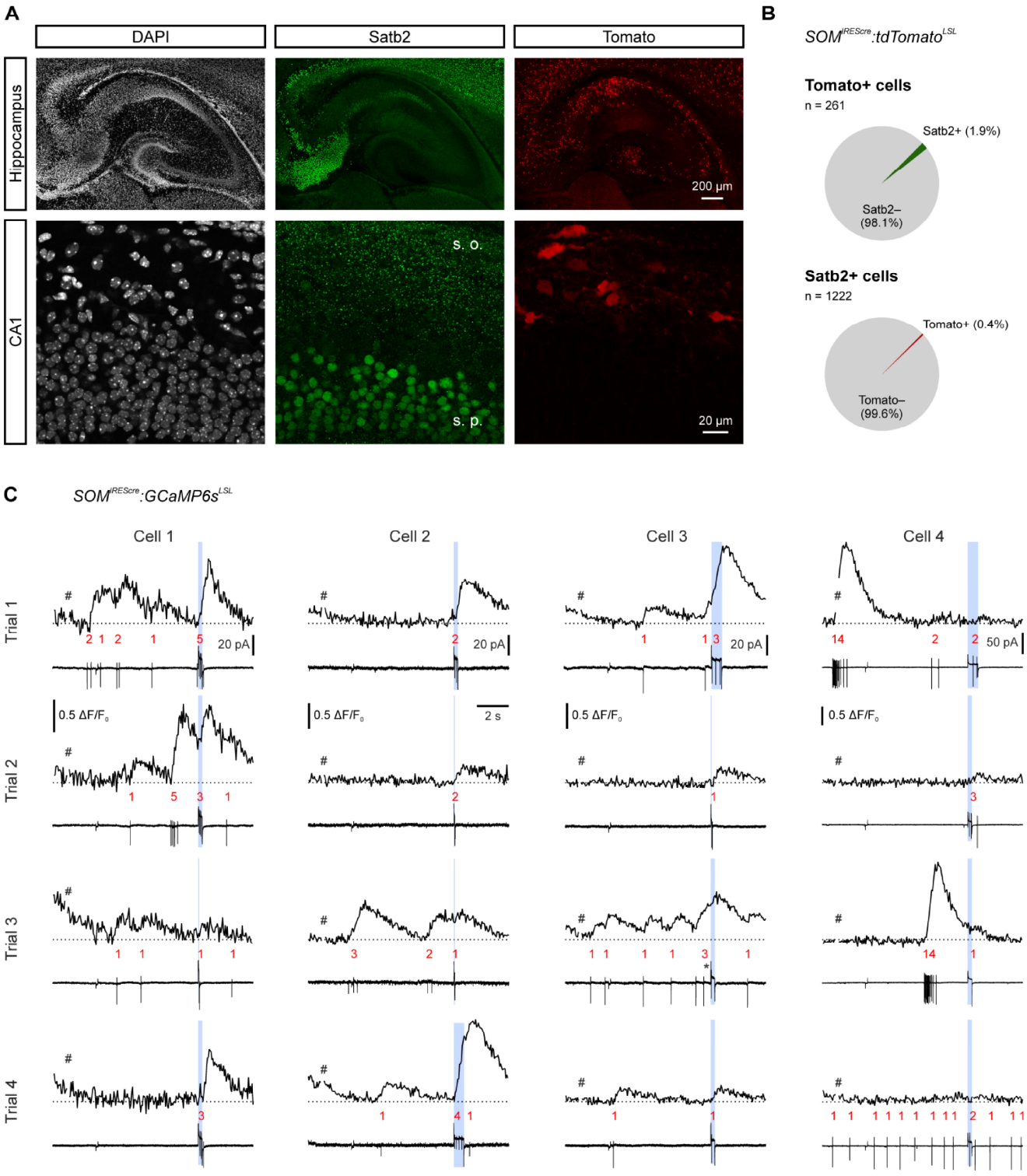

Figure S1. Related to Figure 1. Basic characterization of cells targeted in *SOM*^{IREScre} mice. (A) Sample confocal fluorescence images of a histological section from a *SOM*^{IREScre}*:tdTomato*^{LSL} mouse, in which the fluorescent protein tdTomato is conditionally expressed in SOM INs. Note the nuclear staining profile of the *bona fide* pyramidal cell marker

Satb2 in *stratum pyramidale* (s. p.) of CA1. Image tiles were manually stitched. Upper-row images were corrected for uneven excitation using a homogeneously fluorescent reference sample. (B) Quantification (data from three mice). Cells were classified as Satb2+ or Satb2– on the basis of a fluorescence index with an expected probability of false Satb2+ cells of 1% (see STAR Methods). Note that virtually all CA1 tdTomato+ are Satb2–. Also note that almost all Satb2+ cells are tdTomato–. (C) Sample Ca^{2+} traces from four representative SOM INs conditionally expressing GCaMP6s, for which simultaneous cell-attached voltage-clamp recordings were obtained. At the end of each trial, current injections of variable amplitude and duration (blue-shaded) were used to evoke action potentials. For clarity, laser-light synchronization pulses were removed (#) and capacitive transients in response to current injections were clipped. Red numbers indicate the numbers of action currents detected. Holding and test currents were varied in order to induce a range of firing frequencies. The asterisk (*) in cell 3 (trial 3) indicates clipping of an electromagnetic artefact. Note that CaTs were stereotypically accompanied by one or more action current(s). Also note that (1) single action potentials evoked discernible CaTs in several (cells 1–3), but not all (cell 4), cells, (2) within-burst action potentials could generally not be resolved as separate events, and (3) action potentials during epochs of 'tonic firing' were poorly resolved (e.g. cell 4), indicating that GCaMP6s tends to underestimate the real spiking activity in SOM INs at the age investigated.

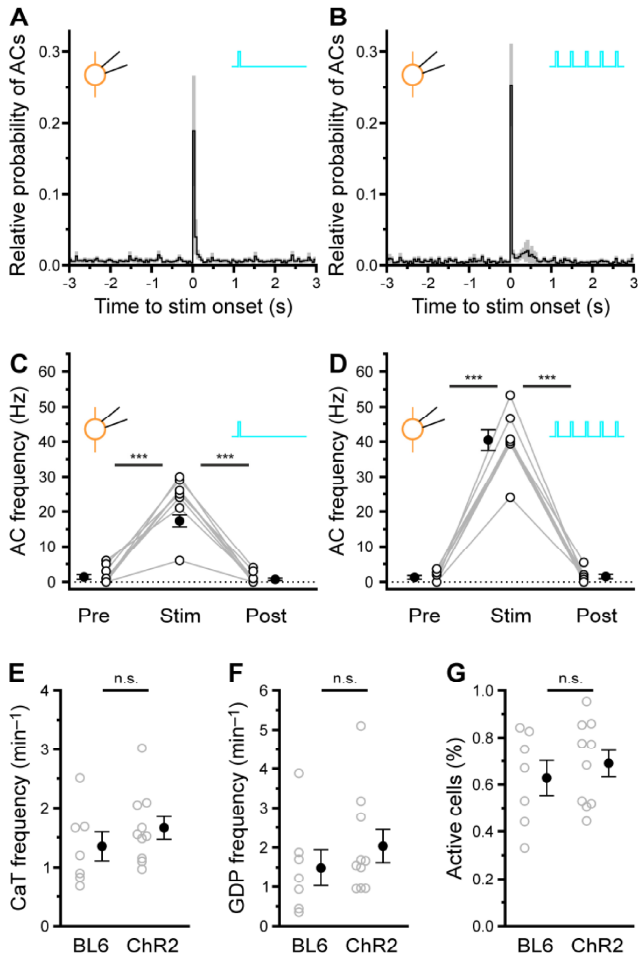

Figure S2. Related to Figures 2 and 3. Photo-stimulation of ChR2^{SOM} induces action potential firing of SOM INs in a reversible, pulse number-dependent manner. (A) and (B) Relative probability of action currents (ACs) in a 6-s period around the onset of photo-stimulation with single pulses [(A); pulse duration: 2 ms; n = 9 cells] or trains of five pulses [(B); delivered at 100 Hz; n = 8 cells]. Recordings were done in the presence of DNQX, APV and bicuculline. Data are presented as mean ± SEM. Note that the relative probability plot in (A) (shown here for comparison) is identical to that in Figure 2D. (C) and (D) Frequency of ACs quantified for 50-ms-long time intervals immediately before stimulation (Pre), after stimulation onset (Stim) and 1 s after stimulation onset (Post) – separately for single pulses (C) and trains of five pulses (D). Data are presented as mean ± SEM. Each symbol represents a single cell. *** $P < 0.001$. Note that two-way repeated-measures ANOVA yielded a significant interaction of the independent variables (pulse number × Pre-Stim-Post) suggesting that the excitatory effect of ChR2^{SOM} stimulation depends on the number of pulses. (E–G) Similar basic properties of CA1 network activity in *SOM^{IREScre}:ChR2(H134R)^{LSL}* and C57BL/6J mice revealed by spinning-disc confocal Ca^{2+} imaging. Quantification (mean ± SEM) of the average single-cell CaT frequency (E), the frequency of GDPs (F) as well as the mean fraction of active cells per GDP (G) for both C57BL/6J (BL6) and *SOM^{IREScre}:ChR2(H134R)^{LSL}* (ChR2) mice. Each gray symbol represents a single slice. n.s. – not significant. A synopsis of the applied statistical procedures can be found in Tables S2 and S4.

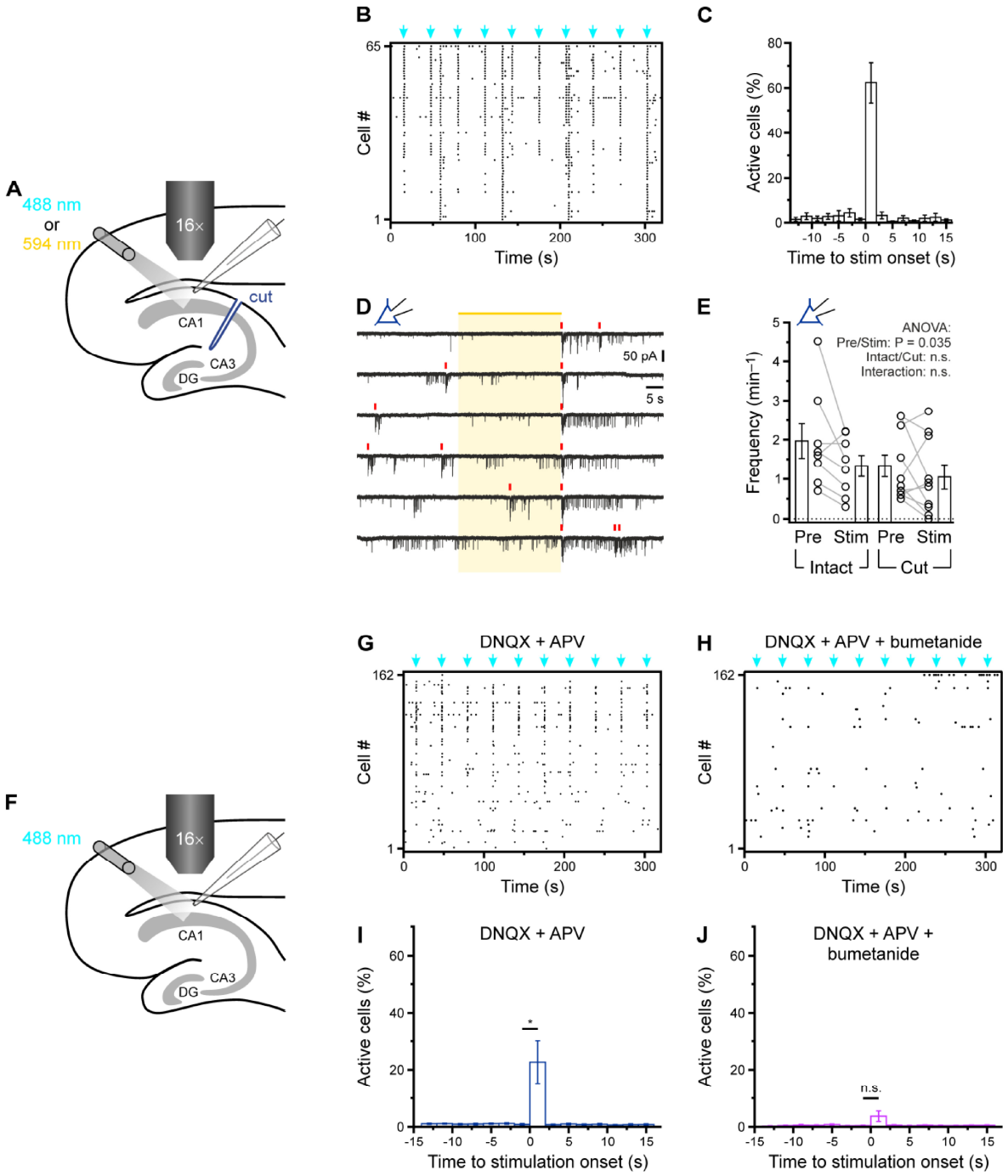

Figure S3. Related to Figures 3 and 4. The synchronizing effects of SOM INs depend on glutamatergic transmission, but not intact projections from CA3. (A) Experimental arrangement. CA1 was mechanically disconnected from CA3. (B) Raster plot indicating times of peak of CaTs from all individual cells (primarily PCs) of a single slice. Blue arrows indicate time periods of $ChR2^{SOM}$ stimulation at 488 nm (50 ms, 100 Hz). (C) Average fraction of active cells aligned to the onset of photostimulation at time = 0 s (n = 6 cells, bin size = 2 s). (D) Sample whole-cell voltage-clamp recording illustrating that photostimulation of $HR3^{SOM}$ (yellow, 30 s) inhibited the generation of PSC bursts in slices with CA3 cut. PSC bursts are indicated by red lines. (E) Absolute PSC burst frequency in intact slices (n = 8 PCs, same cells as in Figures 4I–K) and slices in which

a cut was made between CA3 and CA1 (n = 10 PCs) before (Pre) and during (Stim) photo-stimulation of $HR3^{SOM}$. (F) Experimental arrangement. (G) and (H) Raster plots indicating times of peak of CaTs from all individual cells of a single slice in the continuous presence of DNQX (10 μM) and APV (50 μM) – before (G) and after (H) wash-in of the NKCC1 inhibitor bumetanide (10 μM). Blue arrows indicate time periods of optogenetic stimulation at 488 nm (50 ms, 100 Hz). Note that bumetanide largely abolished the effect of optogenetic stimulation. (I) and (J) Average fraction of active cells aligned to the onset of photo-stimulation (time = 0 s) before [(I); n = 6 slices] and after [(J); n = 5 slices] wash-in of bumetanide. Data are presented as mean ± SEM (bin size = 2 s). * $P < 0.05$, n.s. – not significant. A synopsis of the applied statistical procedures can be found in Table S4.

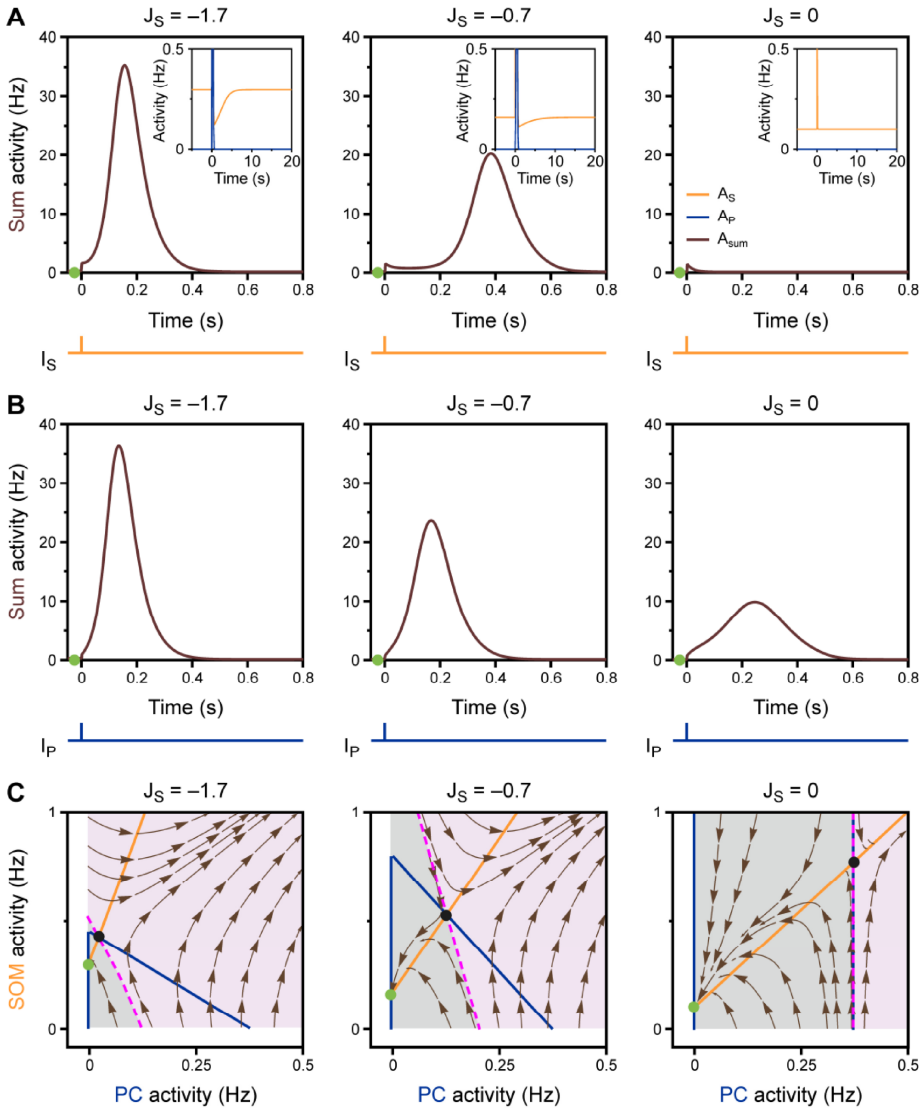

Figure S4. Related to Figure 5. In the STP-RNN model with excitatory GABA, SOM INs cooperate with PCs in governing simGDP characteristics. (A) Sum activity $A_{sum} = A_P + A_S$ of the STP-RNN in response to a perturbation of the SOM population ($I_S(t=0) = 30$ Hz) at three levels of the absolute synaptic efficacy of GABAergic transmission (J_S). J_S = 0 indicates complete block of GABAergic transmission. Green dots indicate the spontaneous stable FP (i.e. the rest state) of the STP-RNN. Insets show network activity at longer time-scales. (B) Same as (A), but the perturbation was applied to the PC population ($I_P(t=0) = 30$ Hz). Note that simGDPs can emerge even when J_S = 0. (C) A_S-A_P-plane of the STP-RNN with frozen synaptic efficacies at the corresponding rest state [see green dots in (A)]. Same format is used as in Figure 5C. Decreasing $|J_S|$ shifted the amplification threshold (magenta) upwards and to the right, and increased the area under the non-amplification (i.e. attraction) domain.

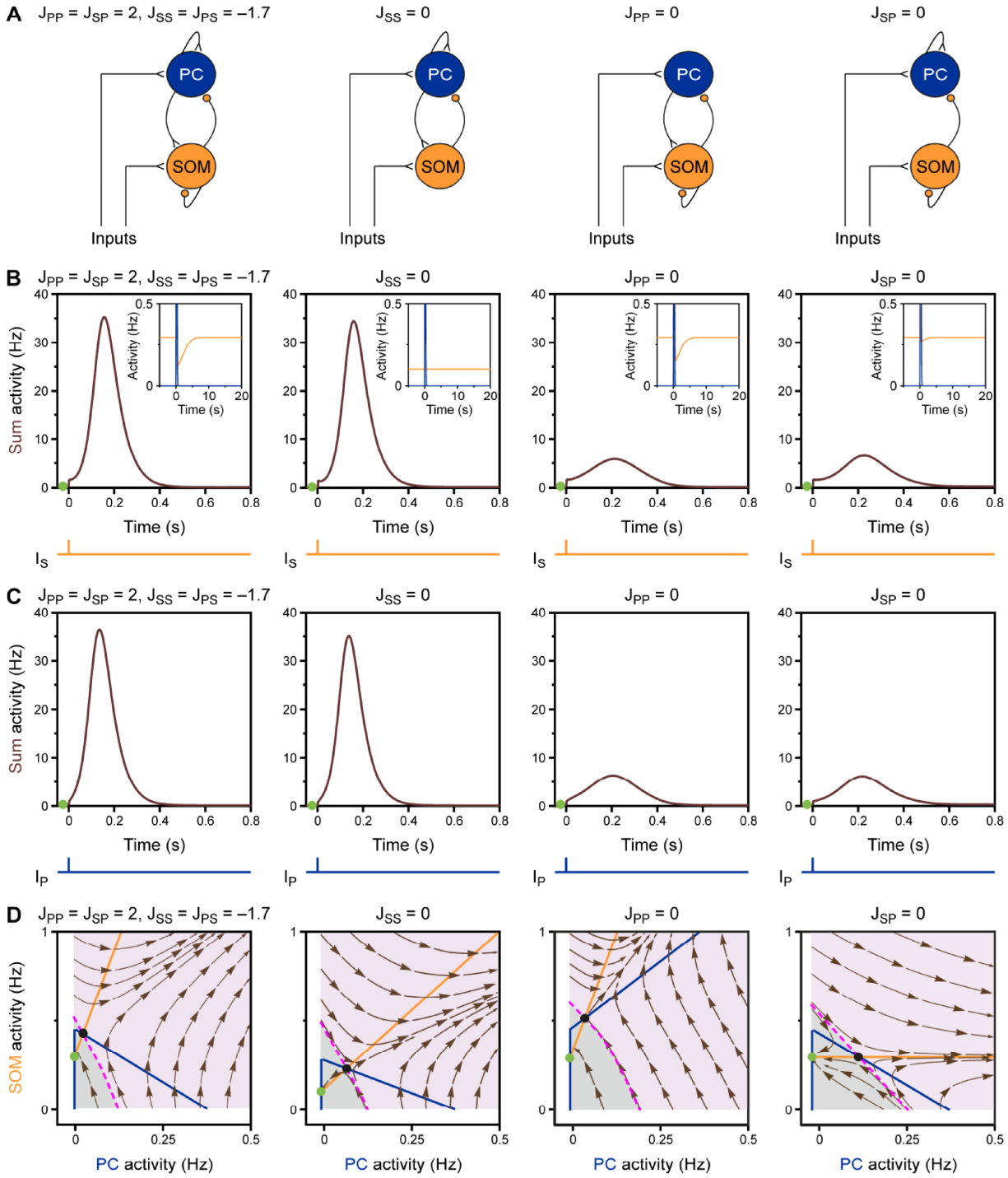

Figure S5. Related to Figure 5. In the STP-RNN model with excitatory GABA, PC–PC and PC–SOM connections contribute more to simGDP generation than SOM SOM synapses. (Λ D) The STP-RNN with parameter values as in Figure 5 (*first column*) and after selective removal of either recurrent SOM–SOM (i.e. $J_{SS} = 0$, *second column*) or recurrent PC–PC (i.e. $J_{PP} = 0$, *third column*) or PC–SOM (i.e. $J_{SP} = 0$, *fourth column*) connections. (A) Graphs representing the four network models. The rest of parameter values of the STP-RNN remain unchanged. (B) Block of PC–PC or PC–SOM synapses

profoundly reduced simGDP size, whereas block of SOM–SOM synapses had a minor effect. Note the decrease in spontaneous activity rate of the SOM population after setting $J_{SS} = 0$. (C) Same as (B), but the perturbation was applied to the PC population. Similarly to (B), simGDP size underwent a stronger reduction after setting $J_{PP} = 0$ or $J_{SP} = 0$, as compared to $J_{SS} = 0$. (D) A_S-A_P-plane of the STP-RNN with frozen synaptic efficacies at the corresponding rest state [see green dots in (B)]. Same format is used as in Figure 5C.

Table S1. Synopsis of statistical tests related to Figure 1.

Running #	Related to	Test statistics	Test(s)
1	Figure 1D	measured: 0.35 ± 0.02, shuffled: $2.1 \times 10^{-5} \pm 4.2 \times 10^{-5}$; W = 1035, P = 5.7×10^{-14}, n = 45 neuron pairs (data from 15 slices)	exact Wilcoxon signed-rank test
2	Figure 1E	measured: 81.1 ± 3.1%, shuffled: 12.0 ± 1.1%; W = 990, P = 1.1×10^{-13}, n = 44 cells (data from 18 slices)	exact Wilcoxon signed-rank test
3	Figure 1F (fGDP)	baseline: 1.1 ± 0.3 min^{-1}, bumetanide: 0.1 ± 0.1 min^{-1}; t = 4.0, df = 10, P = 2.6×10^{-3}, n = 11 slices	paired t-test
4	Figure 1F (CaT)	baseline: 3.0 ± 0.4 min^{-1}, bumetanide: 1.3 ± 0.6 min^{-1}; W = 327, P = 4.8×10^{-4}, n = 27 cells (data from 11 slices)	exact Wilcoxon signed-rank test
5	Figure 1J	measured: 0.42 ± 0.00, shuffled: 0.00 ± 0.00; W = 62479431, Z = 92, P < 1.0×10^{-16}, n = 11178 neuron pairs (data from 11 slices)	Wilcoxon signed-rank test
6	Figure 1K	measured: 92.8 ± 0.4%, shuffled: 10.6 ± 0.2%; W = 115440, Z = 19, P < 1.0×10^{-16}, n = 480 cells (data from 11 slices)	Wilcoxon signed-rank test
7	Figure 1L (fGDP)	baseline: 1.4 ± 0.2 min^{-1}, bumetanide: 0.3 ± 0.2 min^{-1}; t = 8.3, df = 8, P = 3.3×10^{-5}, n = 9 slices	paired t-test
8	Figure 1L (CaT)	baseline: 2.3 ± 0.3 min^{-1}, bumetanide: 0.6 ± 0.1 min^{-1}; W = 45, P =3.9×10^{-3}, n = 9 slices	exact Wilcoxon signed-rank test

Table S2. Synopsis of statistical tests related to Figures 2 and S2.

Running #	Related to	Test statistics	Test(s)
1	Figure 2C (SOM)	SOM: –98 ± 29 pA; t = –3.4, df = 8, P = 9.7 × 10^{-3}, n = 9 cells	one-sample t-test (null hypothesis: mean = 0)
2	Figure 2C (PC)	PC: –0.1 ± 0.1 pA; t = –0.83, df = 5, P = 0.44, n = 6 cells	one-sample t-test (null hypothesis: mean = 0)
3	Figures 2D and S2A and S2C (1 pulse)	pre: 1.4 ± 0.7 Hz, stim: 17 ± 2 Hz, post: 0.7 ± 0.3 Hz; F = 92.9, df = 1.2, P = 1.5 ×10^{-6}, n = 9 cells; P (pre vs. stim) = 3.4 ×10^{-5}, P (stim vs. post) = 2.3 ×10^{-5}, P (pre vs. post) = 0.69	one-way repeated-measures ANOVA (Huynh-Feldt correction); post hoc Bonferroni tests
4	Figures S2B and S2D (5 pulses)	pre: 1.3 ± 0.5 Hz, stim: 40 ± 8 Hz, post: 1.5 ± 0.6 Hz; F = 169, df = 1.0, P = 2.2 ×10^{-6}, n = 8 cells; P (pre vs. stim) = 8.4 ×10^{-6}, P (stim vs. post) = 1.3 ×10^{-5}, P (pre vs. post) = 1.0	one-way repeated-measures ANOVA (Huynh-Feldt correction); post hoc Bonferroni tests
5	Figures S2C and S2D [1 vs. 5 pulse(s)]	interaction (pulse number × pre-stim-post): F = 43.9, df = 1.1, P = 2.0 × 10^{-4}, n = 8 cells	two-way repeated-measures ANOVA (Huynh-Feldt correction)
6	Figure 2F	baseline: –42 ± 9 pA, block: –0.5 ± 0.5 pA; t = –4.9, df = 7, P = 1.7 × 10^{-3}, n = 8 cells	paired t-test
7	Figure 2I	pre: 0.1 ± 0.0 Hz, stim: 3.3 ± 0.8 Hz, post: 0.1 ± 0.1; F = 14.4, df = 1.0, P = 0.012, n = 6 cells; P (pre vs. stim) = 0.033, P (stim vs. post) = 0.043, P (pre vs. post) = 1.0	one-way repeated-measures ANOVA (Huynh-Feldt correction); post hoc Bonferroni tests
8	Figure S2E	BL6: 1.4 ± 0.2 min^{-1}, ChR2: 1.7 ± 0.6 min^{-1}; t = –1.0, df = 15, P = 0.33	two-sample t-test
9	Figure S2F	BL6: 1.5 ± 0.5 min^{-1}, ChR2: 2.0 ± 0.4 min^{-1}; U = 26, P = 0.42 (BL6/ChR2: n = 7/10 slices)	exact Mann-Whitney U-test
10	Figure S2G	BL6: 0.63 ± 0.07, ChR2: 0.69 ± 0.06; t = –0.67, df = 15, P = 0.51	two-sample t-test

Table S3. Synopsis of statistical tests related to Figure 3.

Running #	Related to	Test statistics	Test(s)
1	Figure 3E (baseline)	pre: 5.7 ± 2.7%, stim: 56 ± 10%; t = –4.8, df = 9, P = 1.0×10^{-3}, n = 10 slices	paired t-test
2	Figure 3E (bumetanide)	pre: 1.6 ± 0.8%, stim: 0.16 ± 0.06; t = –2.5, df = 9, P = 0.037, n = 10 slices	paired t-test
3	Figure 3E (baseline vs. bumetanide)	interaction (+/– bumetanide × pre/post stim): F = 19.5, df = 1, P = 1.7×10^{-3}, n = 10 cells	mixed-model ANOVA
4	Figure 3F (left)	A (spont): 62 ± 3%, B (evoked, base): 81 ± 3%, C (evoked, bume): 47 ± 4%; χ^2 = 31.7, df = 2, P = 1.3×10^{-7}, A: n = 128 GDPs, B: n = 67 GDPs, C: n = 25 GDPs; P (A vs. B) = 1.1×10^{-5}, P (A vs. C) = 0.17, P (B vs. C) = 2.2×10^{-7}	Kruskal-Wallis ANOVA; post hoc exact Mann-Whitney U-tests with Bonferroni correction
5	Figure 3F (middle)	A (spont): 0.240 ±0.009 $\Delta F/F_0$, B (evoked, base): 0.28 ± 0.10 $\Delta F/F_0$, C (evoked, bume): 0.22 ± 0.02 $\Delta F/F_0$; χ^2 = 14.8, df = 2, P = 6.0×10^{-4}, A: n = 110 GDPs, B: n = 66 GDPs, C: n = 25 GDPs; P (A vs. B) = 1.7×10^{-3}, P (A vs. C) = 0.72, P (B vs. C) = 0.012	Kruskal-Wallis ANOVA; post hoc exact Mann-Whitney U-tests with Bonferroni correction
6	Figure 3F (right)	A (spont): 183 ± 7 ms, B (evoked, base): 176 ± 8 ms, C (evoked, bume): 234 ± 21 ms; χ^2 = 6.27, df = 2, P = 0.043, A: n = 128 GDPs, B: n = 67 GDPs, C: n = 25 GDPs; P (A vs. B) = 1.0, P (A vs. C) = 0.079, P (B vs. C) = 0.042	Kruskal-Wallis ANOVA; post hoc exact Mann-Whitney U-tests with Bonferroni correction

Table S4. Synopsis of statistical tests related to Figures 3 and S3.

Running #	Related to	Test statistics	Test(s)
1	Figures 3E (intact) and S3C (cut)	interaction: P = 0.52, F = 0.440, df = 1; main effect stim.: P = 4.9×10^{-6}, F = 51.2, df = 1; main effect intact/cut: P = 0.89, F = 0.020 (df = 1)	mixed-model ANOVA
2	Figures S3E	interaction: P = 0.39, F = 0.774, df = 1; main effect stim.: P = 0.035, F = 5.34, df = 1; main effect intact/cut: P = 0.29, F = 1.22, df = 1	mixed-model ANOVA
3	Figure S3I	baseline: 0.008 ± 0.003, stim: 0.23 ± 0.07; t = –2.8, df = 5, P = 0.036, n = 6 slices	paired t-test
4	Figure S3J	baseline: 0.005 ± 0.001, stim: 0.04 ± 0.02; t = –1.8, df = 4, P = 0.15, n = 5 slices	paired t-test

Table S5. Synopsis of statistical tests related to Figure 4.

Running #	Related to	Test statistics	Test(s)
1	Figure 4D	baseline: 2.0 ± 0.6 Hz, stim: 0.4 ± 0.1 Hz; t = –9.4, df = 9, P = 6.0×10^{-4}, n = 10 cells	one-sample t-test on normalized data (null hypothesis: mean = 1)
2	Figures 4F and 4K (GPSCs)	baseline: 1.9 ± 0.4 Hz, stim: 1.3 ± 0.2 Hz; t = –5.9, df = 4, P = 4.2×10^{-3}, n = 5 cells	one-sample t-test on normalized data (null hypothesis: mean = 1)
3	Figure 4H	measured: 48.9 ± 9.7%, shuffled: 9.2 ± 1.6%; t = –4.3, df = 6, P = 5.2×10^{-3}, n = 7 cells	paired t-test
4	Figures 4J and 4K (PSCs)	baseline: 2.5 ± 0.6 Hz, stim: 1.7 ± 0.5 Hz; W = 1, P = 3.9×10^{-3}, n = 10 cells	exact one-sample Wilcoxon signed-rank test on normalized data (null hypothesis: median = 1)
5	Figure 4K (bursts)	baseline: 2.0 ± 0.4 min^{-1}, stim: 1.3 ± 0.3 min^{-1}; W = 2, P = 0.047, n = 8 cells	exact one-sample Wilcoxon signed-rank test on normalized data (null hypothesis: median = 1)

7. Addendum: Optimized photo-stimulation of eNpHR3.0

This chapter presents additional results that are not part of the published manuscript. The methodological development reported here served as an important prerequisite for conducting optogenetic manipulations based on eNpHR3.0, as applied in Flossmann *et al.* (2019).

7.1 Improvement of eNpHR3.0-derived photocurrents

A widely used optogenetic strategy for inhibition makes use of the light-driven Cl^- pump eNpHR3.0 (HR3). A major drawback of HR3 is its fast inactivation kinetic upon prolonged illumination rendering long-term hyperpolarization via HR3 complicated (Han and Boyden 2007, Tonnesen *et al.* 2009).

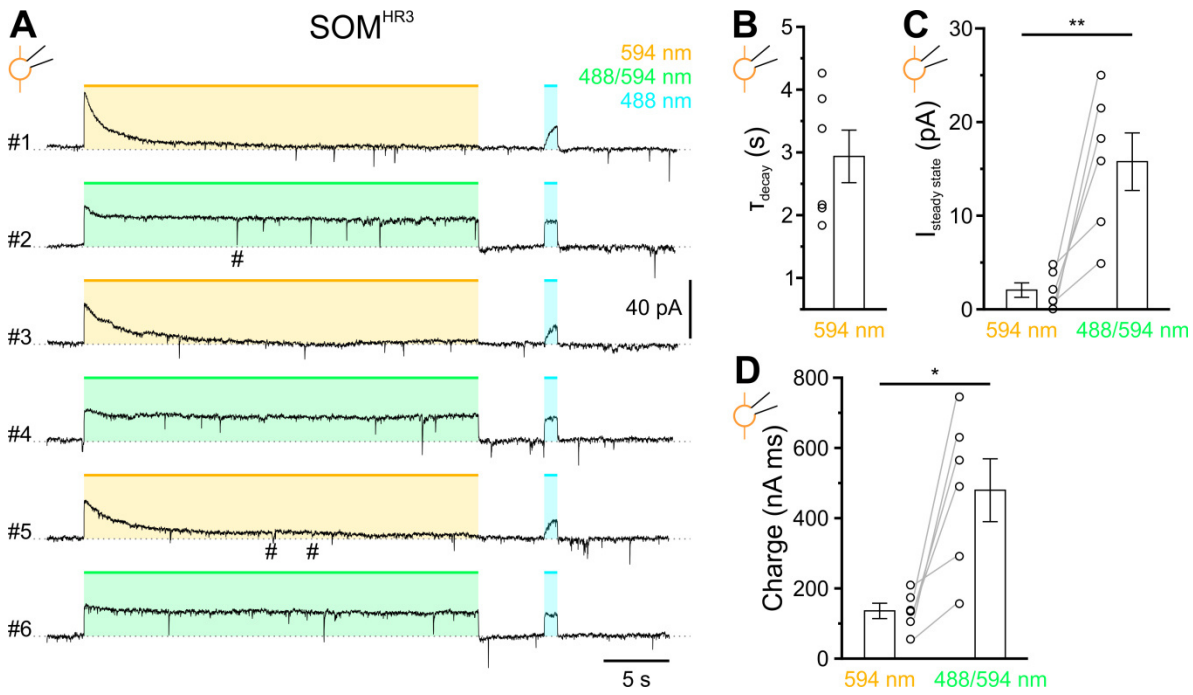

Figure 4. HR3-derived photocurrents upon 594 nm photo-stimulation show strong inactivation, which is reduced by co-illumination with light at 488 nm wavelength.

(A) Whole cell patch-clamp recordings from a SOM interneuron expressing HR3 with repetitive photo-stimulation. Stimulation was applied for 30 s with continuous 594 nm illumination or excitation with 488 nm and 594 nm wavelengths alternating at 1000 Hz. Subsequent illumination was applied at 488 nm (1 s) for acceleration of the recovery rate. Traces were down-sampled to 100 Hz. Some postsynaptic currents (PSCs) were clipped (#) for clarity. (B) and (C) Effect of stimulation regimes (594 versus 488/594) on steady state current ($I_{steady\ state}$) and charge transfer during illumination period (n = 6 cells). *p < 0.05, **p < 0.01

The measurements were obtained from the same cells as in Flossmann *et al.* (2019). According to the literature, the highest peak currents were achieved upon illumination with yellow light (Zhang *et al.* 2007). In whole-cell voltage-clamp recordings at a holding potential of –70 mV, excitation at 594 nm and ~5 mW output power at the fiber tip induced outward currents with fast on- and off-kinetics. However, during continuous stimulation, the photocurrents exhibited pronounced inactivation as they decayed with a time constant of 2.9 ± 0.4 s (n = 6 cells, Figure 4A-B).

τ_{decay} was obtained as mean value of τ from each particular cell. τ was derived from a fit of the first 10 s of the photocurrent to a mono- (1) or bi-exponential (2) function with C fixed to the baseline current at pre-illumination period. τ from the bi-exponential fit was calculated as weighted τ_w (3).

$$current = A \times e^{-\frac{\Delta t}{\tau}} + C \qquad (1)$$

$$current = A_1 \times e^{-\frac{\Delta t}{\tau_1}} + A_2 \times e^{-\frac{\Delta t}{\tau_2}} + C \qquad (2)$$

$$\tau_w = \frac{\tau_1 \times A_1 + \tau_2 \times A_2}{A_1 + A_2} \qquad (3)$$

The application of subsequent illumination at 488 nm (1 s, ~5 mW) accelerated the recovery from inactivation and showed a notable photocurrent (Figure 4A). Combining 594 nm and 488 nm illumination in an alternating manner at 1000 Hz significantly improved steady-state photocurrents upon long-term HR3 stimulation (594 nm: 2.1 pA ± 0.8 pA; 484/594 nm: 15.8 ± 3.1 pA, paired t-test, $p = 7.8 \times 10^{-3}$; Figure 4A, C). This was reflected in a significantly higher charge transfer during the stimulation period (594 nm: 136 nA ms ± 22 nA ms; 488/594 nm: 480 nA ms ± 90 nA ms, paired t-test, p = 0.010; Figure 4D). The optimized photo-stimulation regime was used to achieve long-term inhibition of spontaneous activity in SOM interneurons (Flossmann *et al.* 2019).

The here found observations led to a study to characterize photo-inactivation and wavelength-dependent recovery of HR3 in more detail and provide a significantly enhanced stimulation protocol for long-term photo-inhibition in neurons (Zhang *et al.* unpublished manuscript).

8. Discussion

The present work combined optical, electrophysiological and computational approaches to elucidate the role of SOM interneurons in structuring GDPs, the predominant correlated neuronal activity in immature murine hippocampal slice preparations.

The main findings of the present study are:

(1) During GDPs SOM interneurons and glutamatergic PCs are co-active in a highly correlated manner.

(2) At the perinatal stage SOM interneurons have excitatory $GABA_AR$-mediated synaptic projections to PCs.

(3) Excitatory GABAergic transmission from SOM interneurons depends on chloride import by NKCC1.

(4) Synchronous stimulation of GABA-release from SOM interneurons evokes correlated activity reminiscent of GDPs and dependent on NKCC1.

(5) Inhibition of spontaneous action potential-mediated GABA release from SOM interneurons attenuates GDP activity.

(6) Computational modelling suggests two mechanisms underlying GDP generation in a bi-stable network with excitatory GABA: 1) temporally patterned GABA release from SOM interneurons triggers GDPs and 2) tonic action potential firing of SOM interneurons drives the network closer to a threshold for GDP generation.

8.1 Methodological considerations

8.1.1 Animals

The questions addressed here were tackled in an *in vitro* model, using acute hippocampal brain slices from transgenic neonatal mice. Neonatal mice at the first postnatal week are a model of the last trimester of human pregnancy (Romijn *et al.* 1991, Clancy *et al.* 2001). The phenomenon of sensory-independent correlated activity during development can be found in preterm human infants as well as in neonatal mice (Iyer *et al.* 2015). Though acute brain slices consist of a reduced

neuronal network, they can be studied under controlled conditions: temperature, pH, nutrition support, application of indicators and pharmacological substances can be controlled on a precise time scale and changes can be administered in a highly reproducible manner. Further, the brain slices can be maintained vital for several hours and do generate correlated neuronal activity spontaneously, which is thought to be analogous to that found under *in vivo* conditions (Ben-Ari *et al.* 1989, Sipilä *et al.* 2006).

The transgenic driver lines Emx1^{IREScre} (Jackson, Stock No. 005628) and SOM^{IREScre} (Jackson, Stock No. 013044) were used for cell-specific cre-dependent expression (Gorski *et al.* 2002, Taniguchi *et al.* 2011). All reporter genes were expressed under control of the constitutive CAG promoter at the Gt(ROSA)26Sor locus upon cre-recombination of the loxP-flanked STOP cassette, which provides ubiquitous and homogenous transcription in the target cell populations (Zambrowicz *et al.* 1997, Madisen *et al.* 2009). The Emx1 promoter is specific for excitatory glutamatergic neurons like PCs and is also translated in glia, but not GABAergic neurons (Gorski *et al.* 2002, Kummer *et al.* 2012). The specificity of SOM^{IREScre} mice was evaluated and demonstrated to be separated from glutamatergic Satb2-positive neuron population in the neonatal CA1 (Flossmann *et. al* 2019, Figure S1A-B).

8.1.2 Optogenetic approaches

To dissect the synaptic contribution of SOM interneurons to the generation of correlated activity, optogenetic actuators were cell-specifically expressed. Optogenetic approaches are minimally invasive and powerful tools to investigate connectivity and functions of single neurons or neuron populations in a circuitry (Emiliani *et al.* 2015).

For activation of SOM interneurons, a channelrhodopsin 2 (ChR2) fused to an enhanced yellow fluorescent protein (EYFP) was expressed in transgenic mice (SOM^{ChR2}) to evoke depolarizing currents in SOM interneurons (Boyden *et al.* 2005). The expressing cell population can be identified by the EYFP tag of the construct. ChR2 is a light-gated cation channel with fast on-kinetics, a net depolarization and permeable to: $H^+ >> Na^+ > K^+ >> Ca^{2+}$ (Nagel *et al.* 2003). These properties allow a temporally precise photo-inducible depolarization at the membranes of neuronal somata, dendrites and axons where ChR2 is present with homogeneous distribution. It was verified that photo-stimulation of slices from SOM^{ChR2} mice evoked AP firing by

depolarizing photocurrents in SOM interneurons, but not PCs (Flossmann *et al.* 2019, Figure 2B-D). A general methodical constraint of combining optogenetics and Ca^{2+} imaging is a crosstalk between indicator excitation for the readout of network activity and photo-stimulation of optogenetic actuators in neurons. Excitation of Ca^{2+} indicator OGB1 and photo-stimulation of ChR2 are achieved at the same wavelength of 488 nm. This could induce unintended photocurrents during baseline conditions. This concern was addressed in unpaired comparisons of spontaneous GDPs in slices from wild type and SOM^{ChR2} mice (Flossmann *et al.* 2019, Figure S2). No major changes of GDP parameters were observed during Ca^{2+} imaging in slices from SOM^{ChR2} mice.

For optogenetic inhibition, an enhanced halorhodopsin derived from *Natronomonas pharaonis* and fused to EYFP as expression reporter, eNpHR3 (HR3), was expressed in SOM interneurons (SOM^{HR3}). As a strategy for photo-inhibition, HR3 was chosen over other optogenetic actuators, like the H^+ pump Arch, which changes the intracellular pH upon photo-stimulation or light-gated Cl^- conducting channelrhodopsins (Wietek *et al.* 2015). The mode of action of Cl^- permeable channelrhodopsins strongly depends on the local intracellular Cl^- concentration and might provide even depolarizing currents, especially in immature neurons due to the elevated intracellular chloride levels (Ben-Ari *et al.* 2007). HR3 has the advantage to pump chloride into the cells driven by photo-activation with a transport kinetic relatively independent of intracellular chloride concentrations at physiological conditions. The fast on and off kinetics of HR3-derived photocurrents enables a temporally precise hyperpolarization, which puts HR3 in favor over photo-activated G-protein coupled receptors with slower off kinetics by more than one order of magnitude (Masseck *et al.* 2014). It has to be considered that photo-stimulation of HR3 is increasing the intracellular chloride concentration and thereby shifts E_{Cl^-} towards higher values rendering GABA more depolarizing (Raimondo *et al.* 2012). Further, using hyperpolarization as strategy to inhibit neuronal firing might activate hyperpolarization-activated (I_h) currents like those of HCN-channels, which may attenuate the effect by tonic depolarizing currents (Sartiani *et al.* 2017). Due to the quite negative voltage threshold of HCN-channel activation and comparatively small photocurrents of HR3, this effect is negligible. Here, it was demonstrated that HR3-mediated inhibition is sufficient to reduce action current frequency and GABAergic postsynaptic currents (GPSCs) to stable levels during the stimulation period

(Flossmann *et al.* 2019, Figure 4C-F). However, the incomplete inhibition of action potential firing in SOM interneurons indicates an underestimation of the contribution of SOM to the GABAergic control of correlated neuronal activity. Another limitation of combining optogenetics with Ca^{2+} imaging is that the high-power optogenetic stimulation bleaches the indicator and masks dynamics of the Ca^{2+} signals. For that reason, neuronal activity was electrophysiologically recorded and GDPs were identified as bursts of postsynaptic currents (PSCs) in experiments with optogenetic inhibition of SOM interneurons (Flossmann *et al.* 2019, Figure 4G-K).

8.3 Integration of SOM interneurons in the circuitry of the neonatal CA1

Although large parts of CA1's circuitry are established during the postnatal period, it has to be considered that cell composition and connectivity at neonatal stages are different from the adult stage: First, transient neuronal populations like neurons expressing corticotropin-releasing hormone appear only during postnatal development and vanish after the second postnatal week (Chen *et al.* 2001). Second, the final number of neurons within glutamatergic and GABAergic subpopulations is not set at the first postnatal week due to subsequent activity-dependent apoptosis (Blanquie *et al.* 2017, Denaxa *et al.* 2018). Third, some GABAergic and glutamatergic populations, like thalamo-cortical SOM interneurons (Marques-Smith *et al.* 2016) or CA1 PCs form transient circuits during development (Aniksztejn *et al.* 2001). SOM interneurons are likely to receive excitatory inputs from PCs, as mature OLM interneurons in CA1 receive local and distal glutamatergic inputs from CA1 and CA3 or the entorhinal cortex (Leao *et al.* 2012). Further evidence for a high connectivity of SOM interneurons with PCs comes from a study revealing that MGE-derived interneurons, which give rise to SOM and PV interneurons, are highly interconnected with PCs at the neonatal stage (Wester and McBain 2016). As adult OLM interneurons and BiCs are equipped with synaptic projections from and to other GABAergic interneurons (Chamberland and Topolnik 2012), SOM interneurons are also likely to receive GABAergic inputs and target other interneurons at the immature state. In the present work, the mutual participation of SOM interneurons and glutamatergic PCs in GDPs of the neonatal CA1 demonstrates the synaptic integration of SOM interneurons into the CA1 neuronal network (Flossmann et al. 2019, Figure 1). Attenuating $GABA_AR$-mediated depolarization by application of

NKCC1 inhibitor bumetanide did not only reduce correlated activity in PCs, but also in SOM interneurons indicating a recurrent circuitry (Flossmann *et al.* 2019, Figure 1). Here, it has been experimentally demonstrated, that SOM interneurons have excitatory output-synapses on PCs (Flossmann *et al.* 2019, Figure 2E-I). The depolarizing action is mediated by $GABA_AR$ activation and dependent on Cl^- import by NKCC1. As no postsynaptic currents were observed in PCs under conditions of $GABA_AR$ blockers, SOM- or GABA-mediated GPCR signaling does not significantly contribute to changes in postsynaptic membrane polarization. Further, SOM interneurons account for a considerable fraction of spontaneous GABAergic inputs to PCs, as demonstrated by a reduction of GPSCs by ~30% upon photo-inhibition of SOM^{HR3} (Flossmann *et al.* 2019, Figure 4F). Taking into account that photo-inhibition of spontaneous action current firing in SOM interneurons down to ~25% is incomplete, the impact of SOM interneurons to spontaneous neuronal activity is underestimated (Flossmann *et al.* 2019, Figure 4D). Thus, neonatal SOM interneurons are integrated into the hippocampal network. They account for a considerably high proportion of excitatory GABAergic inputs to PCs, which puts them in a highly connected position within CA1's recurrent circuitry. This finding aligns with the description of super-connected hub cells in the neonatal hippocampus, which are to some extend identified as SOM positive via immuno-staining (Villette *et al.* 2016).

8.4 Towards the mechanisms of SOM interneuron-mediated GDP generation

In vitro, SOM interneurons have a baseline firing rate of 2.0 ± 0.6 Hz which is five-times higher than that of PCs (0.4 ± 0.4 Hz, Flossmann et al. 2019, Figure 4C-D). The elevated spontaneous activity is probably a result of excitatory glutamatergic and GABAergic inputs in combination with a high excitability, which is reflected in a high membrane resistance. This might be further amplified by intrinsic firing properties, as SOM expressing OLM interneurons in the adult hippocampus are fast-spiking and equipped with oscillation mediating hyperpolarization-activated currents (Griguoli *et al.* 2010, Mikulovic *et al.* 2015). Bi-directional control of electrical activity in SOM interneurons by either patterned activation or tonic inhibition scaled with GDP activity (Flossmann *et al.* 2019, Figures 3-4). Simultaneous optogenetic activation of SOM interneurons evoked GDPs in an NKCC1-dependent manner (Flossmann *et al.* 2019, Figure 3). This behavior demonstrates that SOM interneurons conduct parts of the

recurrent excitatory circuitry in CA1 by $GABA_AR$-mediated depolarization. Perturbation of excitatory feedback from SOM interneurons to PCs in the computational model mirrored the experimental observation of a reduction of simulated GDPs (simGDPs, Flossmann *et al.* 2019, Figures 1, 3 and S4). Tonic photo-inhibition of SOM interneurons reduced GPSCs, spontaneous mixed PSCs and GDPs, which goes in line with a study showing that perturbation of activity in MGE-derived interneurons attenuates correlated activity in hippocampal CA1 (Wester and McBain 2016). The idea of SOM interneuron-mediated feed-forward excitation agrees with the explanation that a recurrent excitatory circuitry of GABAergic and glutamatergic synapses is involved in GDP generation (Ben-Ari *et al.* 2007), as well as with *in vivo* evidence for a GABAergic control of synchrony during hippocampal SPWs (Bitzenhofer and Hanganu-Opatz 2014).

Some studies suggest that GABAergic interneurons are the main local source of recurrent excitation in CA1 (Garaschuk *et al.* 1998, Wester and McBain 2016). As SOM interneurons are likely to be a part of the local recurrent excitatory GABAergic network, it raises the question whether sole recurrent GABAergic excitation is able to induce GDPs. Patterned activation of SOM interneurons, under conditions when glutamatergic synaptic transmission was blocked, was strongly attenuated in its ability to synchronize the hippocampal network (Flossmann *et al.* 2019, Figure S3G-I). The same outcome was reproduced for simGDPs, when either recurrent connectivity within the PC population or from the PC to the SOM interneuron population was removed (Flossmann *et al.* 2019, Figure S5). Concurrently, perturbation of connectivity within the SOM interneuron population affected simGDPs to a much lesser degree (Flossmann *et al.* 2019, Figure S5). This behavior indicates a smaller impact of sole recurrent GABAergic than mixed recurrent GABAergic and glutamatergic transmission on network synchronization in CA1. In accordance with the computational model, high spontaneous firing rates and increased excitability of SOM interneurons provide a persistent increase of PC activity due to $GABA_AR$ dependent excitation rendering the network closer to an amplification threshold for correlated activity (Flossmann *et al.* 2019, Figure 5D-E). In addition, SOM interneurons directly contribute to network activity amplification by recurrent feedback excitation to PCs. Thus, the present work demonstrates that SOM interneurons as part of the local excitatory GABAergic network are not able to synchronize PCs

without the recurrent glutamatergic network, indicating PCs as main source of correlated activity in the immature CA1.

As GDPs are large-scale events which are initiated in different hippocampal regions and the entorhinal cortex (Garaschuk *et al.* 1998), it is of mechanistic interest whether SOM interneurons may contribute to the propagation of GDPs. Mature OLM interneurons in CA1 receive glutamatergic inputs from CA3 and might therefore amplify the excitatory input from the Schaffer collateral pathway at immature stages. Furthermore, immature long-range projecting neurons which reside in CA3 or entorhinal cortex and have output synapses in CA1 may synchronize neurons across distal hippocampal areas (Picardo *et al.* 2011, Villette *et al.* 2016). These long-range projecting interneurons express SOM and are likely to support the propagation of correlated neuronal activity from CA3 anterograde to CA1. PCs in CA3 are highly interconnected and provide a recurrent glutamatergic circuitry, which by mutual GABAergic excitation provides a strong drive of GDP generation and renders this region a major origin of GDPs in the hippocampus (Menendez de la Prida *et al.* 1998, Barger *et al.* 2015). The potential function of SOM interneuron-mediated propagation of GDPs from CA3 raises the question whether this is a main mechanism explaining the control of GDPs by bi-directional modulation of SOM interneuron activity. To address this issue, the synaptic connectivity between CA3 and CA1 was mechanically removed (Flossmann *et al.* 2019, Figure S3A-E). Although the GDP frequency tended to be reduced in CA1 under these conditions, the synchronizing capacity of SOM interneurons upon optogenetic activation and more strikingly the dependency of GDPs on spontaneous GABA release from SOM interneurons was preserved (Flossmann *et al.* 2019, Figure S3A-E). This supports the idea that SOM interneurons contribute to local GDPs by a GABAergic contribution to a local recurrent excitatory network in CA1, independent of propagating network activity from adjacent CA3. However, the mechanisms discussed here agree with studies showing that SOM expressing hub interneurons synchronize adjacent hippocampal and neocortical areas by a projection to spatially distributed PCs (Picardo *et al.* 2011, Villette *et al.* 2016).

The presented study provides new insights into a mechanistic understanding of the SOM interneuron-specific GABAergic control of correlated activity in the developing CA1.

9. Conclusions

Main conclusions drawn from the study are:

(1) SOM interneurons participate in spontaneous correlated neuronal activity in the neonatal CA1.

(2) $GABA_AR$-mediated synaptic transmission from SOM interneurons excites glutamatergic PCs in the immature CA1.

(3) Synchronous GABA release from SOM interneurons triggers the generation of correlated neuronal activity in an NKCC1-dependent manner.

(4) Spontaneous firing of SOM interneurons underlies a considerable fraction of GABAergic PSCs in neonatal CA1 PCs.

(5) Tonic or temporally patterned activity of SOM interneurons shifts the network state towards an amplification threshold for the generation of correlated neuronal activity in the developing hippocampus.

SOM interneurons integrate early into the neonatal hippocampal network and provide a considerably large fraction of spontaneous synaptic GABAergic inputs to PCs. They drive correlated neuronal activity in CA1 by an excitatory $GABA_AR$-mediated action dependent on NKCC1-driven Cl^- import. The recurrent excitatory connectivity of SOM interneurons and PCs facilitates correlated neuronal activity in CA1. Two underlying mechanisms were demonstrated: 1) tonic spontaneous activity of SOM interneurons elevates the firing rate of PCs closer to an amplification threshold for correlated activity and 2) activation of PCs by temporally patterned GABA release from SOM interneurons amplifies neuronal activity and generates synchronous activity. The mechanistic insights obtained from the present work complement existing studies in the field. Moreover, the here demonstrated early causal involvement of SOM interneurons in hippocampal synchronization expands our knowledge how the developing circuitry gives rise to correlated activity in the absence of sensory inputs. The reported findings have important implications for activity-dependent brain development.

10. References

Ackman JB, Crair MC. 2014. Role of emergent neural activity in visual map development. Current Opinion in Neurobiology, 24(1):166-175.

Ackman JB, Burbridge TJ, Crair MC. 2012. Retinal waves coordinate patterned activity throughout the developing visual system. Nature, 490(7419):219.

Aniksztejn L, Demarque M, Morozov Y, Ben-Ari Y, Represa A. 2001. Recurrent CA1 collateral axons in developing rat hippocampus. Brain Research, 913(2):195-200.

Arichi T, Whitehead K, Barone G, Pressler R, Padormo F, Edwards AD, Fabrizi L. 2017. Localization of spontaneous bursting neuronal activity in the preterm human brain with simultaneous EEG-fMRI. eLife, 6:e27814.

Babola TA, Li S, Gribizis A, Lee BJ, Issa JB, Wang HC, Crair MC, Bergles DE. 2018. Homeostatic control of spontaneous activity in the developing auditory system. Neuron, 99(3):511-524.e5.

Bandler RC, Mayer C, Fishell G. 2017. Cortical interneuron specification: the juncture of genes, time and geometry. Current Opinion in Neurobiology, 42:17-24.

Bannerman DM, Sprengel R, Sanderson DJ, McHugh SB, Rawlins JN, Monyer H, Seeburg PH. 2014. Hippocampal synaptic plasticity, spatial memory and anxiety. Nature Reviews Neuroscience, 15(3):181-192.

Barger Z, Easton CR, Neuzil KE, Moody WJ. 2015. Early network activity propagates bidirectionally between hippocampus and cortex. Developmental Neurobiology, 76(6):661-72.

Baude A, Bleasdale C, Dalezios Y, Somogyi P, Klausberger T. 2007. Immunoreactivity for the $GABA_A$ receptor alpha1 subunit, somatostatin and Connexin36 distinguishes axoaxonic, basket, and bistratified interneurons of the rat hippocampus. Cerebral Cortex, 17(9):2094-2107.

Ben-Ari Y. 2015. Is birth a critical period in the pathogenesis of autism spectrum disorders? Nature Reviews Neuroscience, 16(8):498-505.

Ben-Ari Y, Cherubini E, Corradetti R, Gaiarsa JL. 1989. Giant synaptic potentials in immature rat CA3 hippocampal neurones. The Journal of Physiology, 416:303-325.

Ben-Ari Y, Gaiarsa JL, Tyzio R, Khazipov R. 2007. GABA: a pioneer transmitter that excites immature neurons and generates primitive oscillations. Physiological Reviews, 87(4):1215-1284.

Ben-Ari Y, Khalilov I, Kahle KT, Cherubini E. 2012. The GABA excitatory/inhibitory shift in brain maturation and neurological disorders. The Neuroscientist, 18 (5):467-486.

Ben-Ari Y, Rovira C, Gaiarsa JL, Corradetti R, Robain O, Cherubini E. 1990. GABAergic mechanisms in the CA3 hippocampal region during early postnatal life. Progress in Brain Research, 83:313-321.

Bitzenhofer SH, Hanganu-Opatz IL. 2014. Oscillatory coupling within neonatal prefrontal-hippocampal networks is independent of selective removal of GABAergic neurons in the hippocampus. Neuropharmacology, 77:57-67.

Blankenship AG, Feller MB. 2010. Mechanisms underlying spontaneous patterned activity in developing neural circuits. Nature Reviews Neuroscience, 11(1):18-29.

Blankenship AG, Ford KJ, Johnson J, Seal RP, Edwards RH, Copenhagen DR, Feller MB. 2009. Synaptic and extrasynaptic factors governing glutamatergic retinal waves. Neuron, 62(2):230-241.

Blanquie O, Yang J-W, Kilb W, Sharopov S, Sinning A, Luhmann HJ. 2017. Electrical activity controls area-specific expression of neuronal apoptosis in the mouse developing cerebral cortex. eLife, 6:e27696.

Bolea S, Avignone E, Berretta N, Sanchez-Andres JV, Cherubini E. 1999. Glutamate controls the induction of GABA-mediated giant depolarizing potentials through AMPA receptors in neonatal rat hippocampal slices. Journal of Neurophysiology, 81(5):2095-2102.

Bonetti C, Surace EM. 2010. Mouse embryonic retina delivers information controlling cortical neurogenesis. PLoS One, 5(12):e15211.

Boyden ES, Zhang F, Bamberg E, Nagel G, Deisseroth K. 2005. Millisecond-timescale, genetically targeted optical control of neural activity. Nature Neuroscience, 8(9):1263-1268.

Bregestovski P, Bernard C. 2012. Excitatory GABA: how a correct observation may turn out to be an experimental artifact. Frontiers in Pharmacology, 3:65.

Buhl DL, Buzsaki G. 2005. Developmental emergence of hippocampal fast-field "ripple" oscillations in the behaving rat pups. Neuroscience, 134(4):1423-1430.

Burbridge TJ, Xu HP, Ackman JB, Ge X, Zhang Y, Ye MJ, Zhou ZJ, Xu J, Contractor A, Crair MC. 2014. Visual circuit development requires patterned activity mediated by retinal acetylcholine receptors. Neuron, 84(5):1049-1064.

Buzsaki G. 2015. Hippocampal sharp wave-ripple: A cognitive biomarker for episodic memory and planning. Hippocampus, 25(10):1073-1188.

Chamberland S, Topolnik L. 2012. Inhibitory control of hippocampal inhibitory neurons. Frontiers in Neuroscience, 6:165.

Che A, Babij R, Iannone AF, Fetcho RN, Ferrer M, Liston C, Fishell G, De Marco Garcia NV. 2018. Layer I interneurons sharpen sensory maps during neonatal development. Neuron, 99(1):98-116.e7.

Chen Y, Bender RA, Frotscher M, Baram TZ. 2001. Novel and transient populations of corticotropin-releasing hormone-expressing neurons in developing hippocampus suggest unique functional roles: a quantitative spatiotemporal analysis. The Journal of Neuroscience, 21(18):7171-7181.

Cherubini E, Gaiarsa JL, Ben-Ari Y. 1991. GABA: an excitatory transmitter in early postnatal life. Trends in Neurosciences, 14(12):515-519.

Clancy B, Darlington RB, Finlay BL. 2001. Translating developmental time across mammalian species. Neuroscience, 105(1):7-17.

Connors SL, Levitt P, Matthews SG, Slotkin TA, Johnston MV, Kinney HC, Johnson WG, Dailey RM, Zimmerman AW. 2008. Fetal mechanisms in neurodevelopmental disorders. Pediatric Neurology, 38(3):163-176.

Cossart R. 2014. Operational hub cells: a morpho-physiologically diverse class of GABAergic neurons united by a common function. Current Opinion in Neurobiology, 26:51-56.

Crepel V, Aronov D, Jorquera I, Represa A, Ben-Ari Y, Cossart R. 2007. A parturition-associated nonsynaptic coherent activity pattern in the developing hippocampus. Neuron, 54(1):105-120.

Demerens C, Stankoff B, Logak M, Anglade P, Allinquant B, Couraud F, Zalc B, Lubetzki C. 1996. Induction of myelination in the central nervous system by electrical activity. Proceedings of the National Academy of Sciences of the United States of America, 93(18):9887-9892.

Denaxa M, Neves G, Rabinowitz A, Kemlo S, Liodis P, Burrone J, Pachnis V. 2018. Modulation of apoptosis controls inhibitory interneuron number in the cortex. Cell Reports, 22(7):1710-1721.

Dupont E, Hanganu IL, Kilb W, Hirsch S, Luhmann HJ. 2006. Rapid developmental switch in the mechanisms driving early cortical columnar networks. Nature, 439(7072):79-83.

Egorov AV, Draguhn A. 2013. Development of coherent neuronal activity patterns in mammalian cortical networks: common principles and local hetereogeneity. Mechanisms of Development, 130(6-8):412-423.

Emiliani V, Cohen AE, Deisseroth K, Hausser M. 2015. All-optical interrogation of neural circuits. The Journal of Neuroscience, 35(41):13917-13926.

Favuzzi E, Deogracias R, Marques-Smith A, Maeso P, Jezequel J, Exposito-Alonso D, Balia M, Kroon T, Hinojosa AJ, E FM, Rico B. 2019. Distinct molecular programs regulate synapse specificity in cortical inhibitory circuits. Science, 363(6425):413-417.

Feller MB, Wellis DP, Stellwagen D, Werblin FS, Shatz CJ. 1996. Requirement for cholinergic synaptic transmission in the propagation of spontaneous retinal waves. Science, 272(5265):1182-1187.

Galli L, Maffei L. 1988. Spontaneous impulse activity of rat retinal ganglion cells in prenatal life. Science, 242(4875):90-91.

Garaschuk O, Hanse E, Konnerth A. 1998. Developmental profile and synaptic origin of early network oscillations in the CA1 region of rat neonatal hippocampus. The Journal of Physiology, 507(1):219-236.

Gorski JA, Talley T, Qiu M, Puelles L, Rubenstein JL, Jones KR. 2002. Cortical excitatory neurons and glia, but not GABAergic neurons, are produced in the Emx1-expressing lineage. The Journal of Neuroscience, 22(15):6309-6314.

Griguoli M, Cherubini E. 2017. Early correlated network activity in the hippocampus: its putative role in shaping neuronal circuits. Frontiers in Cellular Neuroscience, 11:255.

Griguoli M, Maul A, Nguyen C, Giorgetti A, Carloni P, Cherubini E. 2010. Nicotine blocks the hyperpolarization-activated current Ih and severely impairs the oscillatory behavior of *oriens-lacunosum moleculare* interneurons. The Journal of Neuroscience, 30(32):10773-10783.

Gu X, Olson EC, Spitzer NC. 1994. Spontaneous neuronal calcium spikes and waves during early differentiation. The Journal of Neuroscience, 14(11.1):6325-6335.

Han X, Boyden ES. 2007. Multiple-color optical activation, silencing, and desynchronization of neural activity, with single-spike temporal resolution. PLoS One, 2(3):e299.

Hannan AJ, Blakemore C, Katsnelson A, Vitalis T, Huber KM, Bear M, Roder J, Kim D, Shin HS, Kind PC. 2001. PLC-beta 1, activated via mGluRs, mediates activity-dependent differentiation in cerebral cortex. Nature Neuroscience, 4(3):282-288.

Harris KD, Hochgerner H, Skene NG, Magno L, Katona L, Bengtsson Gonzales C, Somogyi P, Kessaris N, Linnarsson S, Hjerling-Leffler J. 2018. Classes and continua of hippocampal CA1 inhibitory neurons revealed by single-cell transcriptomics. PLoS Biology, 16(6):e2006387.

Heck N, Kilb W, Reiprich P, Kubota H, Furukawa T, Fukuda A, Luhmann HJ. 2007. GABA-A receptors regulate neocortical neuronal migration *in vitro* and *in vivo*. Cerebral Cortex, 17(1):138-148.

Hennou S, Khalilov I, Diabira D, Ben-Ari Y, Gozlan H. 2002. Early sequential formation of functional $GABA_A$ and glutamatergic synapses on CA1 interneurons of the rat foetal hippocampus. European Journal of Neuroscience, 16(2):197-208.

Hensch TK. 2005. Critical period plasticity in local cortical circuits. Nature Review Neuroscience, 6(11):877-888.

Hubel DH. 1982. Effects of visual deprivation in cats and monkeys. Acta Ophthalmologica, 60(3):484-485.

Ikonomidou C, Bosch F, Miksa M, Bittigau P, Vockler J, Dikranian K, Tenkova TI, Stefovska V, Turski L, Olney JW. 1999. Blockade of NMDA receptors and apoptotic neurodegeneration in the developing brain. Science, 283(5398):70-74.

Iyer KK, Roberts JA, Hellstrom-Westas L, Wikstrom S, Hansen Pupp I, Ley D, Vanhatalo S, Breakspear M. 2015. Cortical burst dynamics predict clinical outcome early in extremely preterm infants. Brain, 138(8):2206-2218.

Kaila K, Pasternack M, Saarikoski J, Voipio J. 1989. Influence of GABA-gated bicarbonate conductance on potential, current and intracellular chloride in crayfish muscle fibres. The Journal of Physiology, 416:161-181.

Kasyanov AM, Safiulina VF, Voronin LL, Cherubini E. 2004. GABA-mediated giant depolarizing potentials as coincidence detectors for enhancing synaptic efficacy in the developing hippocampus. Proceedings of the National Academy of Sciences of the United States of America, 101(11):3967-3972.

Katz LC, Shatz CJ. 1996. Synaptic activity and the construction of cortical circuits. Science, 274(5290):1133-1138.

Khazipov R, Milh M. 2018. Early patterns of activity in the developing cortex: Focus on the sensorimotor system. Seminars in Cell and Developmental Biology, 76:120-129.

Khazipov R, Sirota A, Leinekugel X, Holmes GL, Ben-Ari Y, Buzsaki G. 2004. Early motor activity drives spindle bursts in the developing somatosensory cortex. Nature, 432(7018):758-761.

Kilb W, Kirischuk S, Luhmann HJ. 2011. Electrical activity patterns and the functional maturation of the neocortex. European Journal of Neuroscience, 34(10):1677-1686.

Kirmse K, Kummer M, Kovalchuk Y, Witte OW, Garaschuk O, Holthoff K. 2015. GABA depolarizes immature neurons and inhibits network activity in the neonatal neocortex *in vivo*. Nature Communications, 6:7750.

Klausberger T. 2009. GABAergic interneurons targeting dendrites of pyramidal cells in the CA1 area of the hippocampus. European Journal of Neuroscience, 30(6):947-957.

Knierim JJ. 2015. The hippocampus. Current Biology, 25 (23):R1116-R1121.

Komuro H, Rakic P. 1996. Intracellular Ca^{2+} fluctuations modulate the rate of neuronal migration. Neuron, 17(2):275-285.

Kummer M, Kirmse K, Witte OW, Holthoff K. 2012. Reliable *in vivo* identification of both GABAergic and glutamatergic neurons using Emx1-Cre driven fluorescent reporter expression. Cell Calcium, 52(2):182-189.

Kummer M, Kirmse K, Zhang CQ, Haueisen J, Witte OW, Holthoff K. 2016. Column-like Ca^{2+} clusters in the mouse neonatal neocortex revealed by three-dimensional two-photon Ca^{2+} imaging *in vivo*. NeuroImage, 138:64-75.

Kwon H-B, Sabatini BL. 2011. Glutamate induces *de novo* growth of functional spines in developing cortex. Nature, 474(7349):100-4.

Leao RN, Mikulovic S, Leao KE, Munguba H, Gezelius H, Enjin A, Patra K, Eriksson A, Loew LM, Tort AB, Kullander K. 2012. OLM interneurons differentially modulate CA3 and entorhinal inputs to hippocampal CA1 neurons. Nature Neuroscience, 15(11):1524-1530.

Leinekugel X, Medina I, Khalilov I, Ben-Ari Y, Khazipov R. 1997. Ca^{2+} oscillations mediated by the synergistic excitatory actions of $GABA_A$ and NMDA receptors in the neonatal hippocampus. Neuron, 18 (2):243-255.

Leinekugel X, Khazipov R, Cannon R, Hirase H, Ben-Ari Y, Buzsaki G. 2002. Correlated bursts of activity in the neonatal hippocampus *in vivo*. Science, 296 (5575):2049-2052.

Liguz-Lecznar M, Urban-Ciecko J, Kossut M. 2016. Somatostatin and somatostatin-containing neurons in shaping neuronal activity and plasticity. Frontiers in Neural Circuits, 10:48.

Lim L, Pakan JMP, Selten MM, Marques-Smith A, Llorca A, Bae SE, Rochefort NL, Marín O. 2018. Optimization of interneuron function by direct coupling of cell migration and axonal targeting. Nature Neuroscience.

Liu M, Wang L, Cang J. 2014. Different roles of axon guidance cues and patterned spontaneous activity in establishing receptive fields in the mouse superior colliculus. Frontiers in Neural Circuits, 8:23.

Luhmann HJ, Sinning A, Yang JW, Reyes-Puerta V, Stuttgen MC, Kirischuk S, Kilb W. 2016. Spontaneous neuronal activity in developing neocortical networks: from single cells to large-scale interactions. Frontiers in Neural Circuits, 10:40.

Madisen L, Zwingman TA, Sunkin SM, Oh SW, Zariwala HA, Gu H, Ng LL, Palmiter RD, Hawrylycz MJ, Jones AR, Lein ES, Zeng H. 2009. A robust and high-

throughput Cre reporting and characterization system for the whole mouse brain. Nature Neuroscience, 13:133.

Marchionni I, Omrani A, Cherubini E. 2007. In the developing rat hippocampus a tonic GABAA-mediated conductance selectively enhances the glutamatergic drive of principal cells. The Journal of Physiology, 581(2):515-528.

Marguet SL, Le-Schulte VT, Merseburg A, Neu A, Eichler R, Jakovcevski I, Ivanov A, Hanganu-Opatz IL, Bernard C, Morellini F, Isbrandt D. 2015. Treatment during a vulnerable developmental period rescues a genetic epilepsy. Nature Medicine, 21(12):1436-44.

Marques-Smith A, Lyngholm D, Kaufmann AK, Stacey JA, Hoerder-Suabedissen A, Becker EB, Wilson MC, Molnar Z, Butt SJ. 2016. A transient translaminar GABAergic interneuron circuit connects thalamocortical recipient layers in neonatal somatosensory cortex. Neuron, 89(3):536-549.

Masseck OA, Spoida K, Dalkara D, Maejima T, Rubelowski JM, Wallhorn L, Deneris ES, Herlitze S. 2014. Vertebrate cone opsins enable sustained and highly sensitive rapid control of $G_{i/o}$ signaling in anxiety circuitry. Neuron, 81(6):1263-1273.

McLaughlin T, Torborg CL, Feller MB, O'Leary DD. 2003. Retinotopic map refinement requires spontaneous retinal waves during a brief critical period of development. Neuron, 40(6):1147-1160.

Meister M, Wong RO, Baylor DA, Shatz CJ. 1991. Synchronous bursts of action potentials in ganglion cells of the developing mammalian retina. Science, 252(5008):939-943.

Menendez de la Prida L, Bolea S, Sanchez-Andres JV. 1998. Origin of the synchronized network activity in the rabbit developing hippocampus. European Journal of Neuroscience, 10(3):899-906.

Meredith RM. 2015. Sensitive and critical periods during neurotypical and aberrant neurodevelopment: a framework for neurodevelopmental disorders. Neuroscience and Biobehavioral Reviews, 50:180-188.

Mikulovic S, Restrepo CE, Hilscher MM, Kullander K, Leao RN. 2015. Novel markers for OLM interneurons in the hippocampus. Frontiers in Cellular Neuroscience, 9:201.

Mikulovic S, Restrepo CE, Siwani S, Bauer P, Pupe S, Tort ABL, Kullander K, Leao RN. 2018. Ventral hippocampal OLM cells control type 2 theta oscillations and response to predator odor. Nature Communications, 9(1):3638.

Modabbernia A, Velthorst E, Reichenberg A. 2017. Environmental risk factors for autism: an evidence-based review of systematic reviews and meta-analyses. Molecular Autism, 8:13.

Modol L, Sousa VH, Malvache A, Tressard T, Baude A, Cossart R. 2017. Spatial embryonic origin delineates GABAergic hub neurons driving network dynamics in the developing entorhinal cortex. Cerebral Cortex, 27(9):4649-4661.

Nagel G, Szellas T, Huhn W, Kateriya S, Adeishvili N, Berthold P, Ollig D, Hegemann P, Bamberg E. 2003. Channelrhodopsin-2, a directly light-gated cation-selective membrane channel. Proceedings of the National Academy of Sciences of the United States of America, 100(24):13940-13945.

O'Leary DDM, Sahara S. 2008. Genetic regulation of arealization of the neocortex. Current Opinion in Neurobiology, 18(1):90-100.

Oh WC, Lutzu S, Castillo PE, Kwon HB. 2016. *De novo* synaptogenesis induced by GABA in the developing mouse cortex. Science, 353(6303):1037-1040.

Pelkey KA, Chittajallu R, Craig MT, Tricoire L, Wester JC, McBain CJ. 2017. Hippocampal GABAergic inhibitory interneurons. Physiological Reviews, 97(4):1619-1747.

Philippidou P, Dasen JS. 2013. Hox genes: choreographers in neural development, architects of circuit organization. Neuron, 80(1):12-34.

Picardo MA, Guigue P, Bonifazi P, Batista-Brito R, Allene C, Ribas A, Fishell G, Baude A, Cossart R. 2011. Pioneer GABA cells comprise a subpopulation of hub neurons in the developing hippocampus. Neuron, 71(4):695-709.

Pleasure SJ, Anderson S, Hevner R, Bagri A, Marin O, Lowenstein DH, Rubenstein JLR. 2000. Cell migration from the ganglionic eminences is required for the development of hippocampal GABAergic interneurons. Neuron, 28(3):727-740.

Priya R, Paredes MF, Karayannis T, Yusuf N, Liu X, Jaglin X, Graef I, Alvarez-Buylla A, Fishell G. 2018. Activity regulates cell death within cortical interneurons through a calcineurin-dependent mechanism. Cell Reports, 22(7):1695-1709.

Raimondo JV, Kay L, Ellender TJ, Akerman CJ. 2012. Optogenetic silencing strategies differ in their effects on inhibitory synaptic transmission. Nature Neuroscien ce, 15(8):1102-1104.

Rivera C, Voipio J, Payne JA, Ruusuvuori E, Lahtinen H, Lamsa K, Pirvola U, Saarma M, Kaila K. 1999. The K^+/Cl^- co-transporter KCC2 renders GABA hyperpolarizing during neuronal maturation. Nature, 397 (6716):251-255.

Romijn HJ, Hofman MA, Gramsbergen A. 1991. At what age is the developing cerebral cortex of the rat comparable to that of the full-term newborn human baby? Early Human Development, 26(1):61-67.

Roux L, Hu B, Eichler R, Stark E, Buzsaki G. 2017. Sharp wave ripples during learning stabilize the hippocampal spatial map. Nature Neuroscience, 20(6):845.

Salgueiro-Pereira AR, Duprat F, Pousinha P, Loucif A, Douchamps V, Regondi C, Ayrault M, Eugie M, Stunault MI, Escayg A, Goutagny R, Gnatkovsky V, Frassoni C, Marie H, Bethus I, Mantegazza M. 2019. A two-hit story: Seizures and genetic mutation interaction sets phenotype severity in SCN1A epilepsies. Neurobiology of Disease, 125:31-44.

Sartiani L, Mannaioni G, Masi A, Novella Romanelli M, Cerbai E. 2017. The hyperpolarization-activated cyclic nucleotide–gated channels: from biophysics to pharmacology of a anique family of ion channels. Pharmacological Reviews, 69(4):354-395.

Sato SS, Artoni P, Landi S, Cozzolino O, Parra R, Pracucci E, Trovato F, Szczurkowska J, Luin S, Arosio D, Beltram F, Cancedda L, Kaila K, Ratto GM. 2017. Simultaneous two-photon imaging of intracellular chloride concentration and pH in mouse pyramidal neurons *in vivo*. Proceedings of the National Academy of Sciences of the United States of America, 114(41):E8770-E8779.

Schmidt MJ, Mirnics K. 2015. Neurodevelopment, GABA system dysfunction, and schizophrenia. Neuropsychopharmacology, 40(1):190-206.

Schwartz TH, Rabinowitz D, Unni V, Kumar VS, Smetters DK, Tsiola A, Yuste R. 1998. Networks of coactive neurons in developing layer 1. Neuron, 20(3):541-552.

Shi Y, Ikrar T, Olivas ND, Xu X. 2014. Bidirectional global spontaneous network activity precedes the canonical unidirectional circuit organization in the developing hippocampus. Journal of Comparative Neurology, 522(9):2191-2208.

Sipilä ST, Huttu K, Soltesz I, Voipio J, Kaila K. 2005. Depolarizing GABA acts on intrinsically bursting pyramidal neurons to drive giant depolarizing potentials in the immature hippocampus. The Journal of Neuroscience, 25(22):5280-5289.

Sipilä ST, Schuchmann S, Voipio J, Yamada J, Kaila K. 2006. The cation-chloride cotransporter NKCC1 promotes sharp waves in the neonatal rat hippocampus. The Journal of physiology, 573(3):765-773.

Siwani S, Franca ASC, Mikulovic S, Reis A, Hilscher MM, Edwards SJ, Leao RN, Tort ABL, Kullander K. 2018. OLMalpha2 Cells Bidirectionally Modulate Learning. Neuron, 99(2):404-412.

Somogyi P, Klausberger T. 2005. Defined types of cortical interneurone structure space and spike timing in the hippocampus. The Journal of Physiology, 562(1):9-26.

Soto F, Ma X, Cecil JL, Vo BQ, Culican SM, Kerschensteiner D. 2012. Spontaneous activity promotes synapse formation in a cell-type-dependent manner in the developing retina. The Journal of Neuroscience, 32(16):5426-5439.

Spitzer NC. 1994. Spontaneous Ca^{2+} spikes and waves in embryonic neurons: signaling systems for differentiation. Trends in Neurosciences, 17(3):115-118.

Spitzer NC. 2006. Electrical activity in early neuronal development. Nature, 444(7120):707-712.

Spitzer NC. 2017. Neurotransmitter switching in the developing and adult brain. Annual Review of Neuroscience, 40:1-19.

Spoljaric I, Spoljaric A, Mavrovic M, Seja P, Puskarjov M, Kaila K. 2019. KCC2-mediated Cl^- extrusion modulates spontaneous hippocampal network events in perinatal rats and mice. Cell Reports, 26(5):1073-1081 e1073.

Stark E, Roux L, Eichler R, Senzai Y, Royer S, Buzsaki G. 2014. Pyramidal cell-interneuron interactions underlie hippocampal ripple oscillations. Neuron, 83(2):467-480.

Taniguchi H, He M, Wu P, Kim S, Paik R, Sugino K, Kvitsiani D, Fu Y, Lu J, Lin Y, Miyoshi G, Shima Y, Fishell G, Nelson SB, Huang ZJ. 2011. A resource of Cre driver lines for genetic targeting of GABAergic neurons in cerebral cortex. Neuron, 71(6):995-1013.

Tonnesen J, Sorensen AT, Deisseroth K, Lundberg C, Kokaia M. 2009. Optogenetic control of epileptiform activity. Proceedings of the National Academy of Sciences of the United States of America, 106(29):12162-12167.

Tricoire L, Pelkey KA, Erkkila BE, Jeffries BW, Yuan X, McBain CJ. 2011. A blueprint for the spatiotemporal origins of mouse hippocampal interneuron diversity. The Journal of Neuroscience, 31(30):10948-10970.

Tukker JJ, Fuentealba P, Hartwich K, Somogyi P, Klausberger T. 2007. Cell type-specific tuning of hippocampal interneuron firing during gamma oscillations *in vivo*. Journal of Neuroscience, 27(31):8184-8189.

Tyzio R, Represa A, Jorquera I, Ben-Ari Y, Gozlan H, Aniksztejn L. 1999. The establishment of GABAergic and glutamatergic synapses on CA1 pyramidal neurons is sequential and correlates with the development of the apical dendrite. The Journal of Neuroscience, 19(23):10372-10382.

Valeeva G, Valiullina F, Khazipov R. 2013. Excitatory actions of GABA in the intact neonatal rodent hippocampus *in vitro*. Frontiers in Cellular Neuroscience, 7:20.

van Rheede JJ, Richards BA, Akerman CJ. 2015. Sensory-evoked spiking behavior emerges via an experience-dependent plasticity mechanism. Neuron, 87(5):1050-1062.

Villette V, Guigue P, Picardo MA, Sousa VH, Leprince E, Lachamp P, Malvache A, Tressard T, Cossart R, Baude A. 2016. Development of early born GABA hub neurons in mouse hippocampus from embryogenesis to adulthood. Journal of Comparative Neurology, 524(12):2440-61.

Washbourne P. 2015. Synapse assembly and neurodevelopmental disorders. Neuropsychopharmacology, 40(1):4-15.

West AE, Greenberg ME. 2011. Neuronal activity-regulated gene transcription in synapse development and cognitive function. Cold Spring Harbor Perspectives in Biology, 3(6).

Wester JC, McBain CJ. 2016. Interneurons differentially contribute to spontaneous network activity in the developing hippocampus dependent on their embryonic lineage. The Journal of Neuroscience, 36(9):2646-2662.

Wiesel TN. 1982. Postnatal development of the visual cortex and the influence of environment. Nature, 299(5884):583-591.

Wietek J, Beltramo R, Scanziani M, Hegemann P, Oertner TG, Wiegert JS. 2015. An improved chloride-conducting channelrhodopsin for light-induced inhibition of neuronal activity *in vivo*. Scientific Reports, 5:14807.

Wong FK, Bercsenyi K, Sreenivasan V, Portalés A, Fernández-Otero M, Marín O. 2018. Pyramidal cell regulation of interneuron survival sculpts cortical networks. Nature, 557(7707):668-673.

Yamada J, Okabe A, Toyoda H, Kilb W, Luhmann HJ, Fukuda A. 2004. Cl^- uptake promoting depolarizing GABA actions in immature rat neocortical neurones is mediated by NKCC1. The Journal of Physiology, 557(3):829-841.

Yap EL, Greenberg ME. 2018. Activity-regulated transcription: bridging the gap between neural activity and behavior. Neuron, 100(2):330-348.

Zambrowicz BP, Imamoto A, Fiering S, Herzenberg LA, Kerr WG, Soriano P. 1997. Disruption of overlapping transcripts in the ROSA beta geo 26 gene trap strain leads to widespread expression of beta-galactosidase in mouse embryos and

hematopoietic cells. Proceedings of the National Academy of Sciences of the United States of America, 94(8):3789-3794.

Zhang F, Wang LP, Brauner M, Liewald JF, Kay K, Watzke N, Wood PG, Bamberg E, Nagel G, Gottschalk A, Deisseroth K. 2007. Multimodal fast optical interrogation of neural circuitry. Nature, 446(7136):633-639.

Zheng JJ, Lee S, Zhou ZJ. 2004. A developmental switch in the excitability and function of the starburst network in the mammalian retina. Neuron, 44(5):851-864.

Zhu JJ, Esteban JA, Hayashi Y, Malinow R. 2000. Postnatal synaptic potentiation: delivery of GluR4-containing AMPA receptors by spontaneous activity. Nature Neuroscience, 3(11):1098-1106.

11. Appendix

11.1. Ehrenwörtliche Erklärung

Hiermit erkläre ich, dass mir die Promotionsordnung der Medizinischen Fakultät der Friedrich-Schiller-Universität bekannt ist,

ich die Dissertation selbst angefertigt habe und alle von mir benutzten Hilfsmittel, persönlichen Mitteilungen und Quellen in meiner Arbeit angegeben sind,

mich folgende Personen bei der Auswahl und Auswertung des Materials sowie bei der Herstellung des Manuskripts unterstützt haben:

Dr. Knut Kirmse, Prof. Dr. Knut Holthoff,

die Hilfe eines Promotionsberaters nicht in Anspruch genommen wurde und dass Dritte weder unmittelbar noch mittelbar geldwerte Leistungen von mir für Arbeiten erhalten haben, die im Zusammenhang mit dem Inhalt der vorgelegten Dissertation stehen,

dass ich die Dissertation noch nicht als Prüfungsarbeit für eine staatliche oder andere wissenschaftliche Prüfung eingereicht habe und

dass ich die gleiche, eine in wesentlichen Teilen ähnliche oder eine andere Abhandlung nicht bei einer anderen Hochschule als Dissertation eingereicht habe.

Jena, den 20. Dezember 2019 Unterschrift des Verfassers

11.2. Danksagung

Hiermit bedanke ich mich herzlich bei meinem Doktorvater Prof. Knut Holthoff, sowie bei Dr. Knut Kirmse für die hervorragende Betreuung während meiner Doktorarbeit und die durchstrukturierte Konzeption des Forschungsprojekts. Außerdem möchte ich an dieser Stelle meine Dankbarkeit darüber ausdrücken, dass mir bei projektbezogenen Anliegen, wie auch bei Fragen im Hinblick auf persönliche Perspektiven in der akademischen Laufbahn immer Tür und Ohr offenstanden, und ich dabei stets mit hilfreichen Ratschlägen unterstützt wurde. Besonderen Dank möchte ich in diesem Zusammenhang an Knut Kirmse richten, der mich in Praxis und Theorie unter anderem der Kalziumbildgebung und Elektrophysiologie eingeführt hat.

Großer Dank gilt auch meinen Kollegen in der Arbeitsgruppe: Jürgen Graf, Chuanqiang Zhang, Michael Kummer, Thomas Kaas und Alexander Joerk mit denen die Zusammenarbeit im Labor immer angenehm und der Umgang untereinander freundschaftlich war. Dankbar bin ich außerdem den technischen Assistentinnen der Abteilung: Ina Ingrisch, Svetlana Würl, Claudia Sommer und Madlen Günther. Im Zusammenhang mit der vorliegenden Arbeit und Publikation danke ich im Besonderen Ina Ingrisch für die technische Hilfe zur Genotypisierung und bei Immunfärbungen.

Ein besonderes Dankeschön möchte ich auch an Vahid Rahmati und Prof. Stefan Kiebel richten, deren Kooperation maßgeblich zur erfolgreichen Veröffentlichung der Publikation beigetragen hat.

Für die finanzielle Unterstützung sowie das wissenschaftliche Programm außerhalb meiner Doktorarbeit danke ich den Organisatoren des interdisziplinären Zentrums für klinische Forschung und des SFB Transregio 166 „Receptor Light“.

Insbesondere danke ich meiner Familie für ihre mentale Unterstützung und Hilfe in kniffeligen Zeiten, sowie dafür dass sie mich auf dem Weg meiner Ausbildung immer mit Rat und Tat begleitet und mir diesen damit überhaupt ermöglicht hat.

Vor allem möchte ich Ann-Kristin Kaune danken für ihre Unterstützung, Geduld und die innige Verbundenheit auf deren Grundlage wir unseren Weg gemeinsam beschreiten.